Author(s): Nörtershäuser, W.; Moore, I. D.

Title: Nuclear Charge Radii

Year: 2023

Version: Accepted version (Final draft)

Please cite the original version:

Nörtershäuser, W., & Moore, I. D. (2023). Nuclear Charge Radii. In I. Tanihata, H. Toki, & T. Kajino (Eds.), Handbook of Nuclear Physics (pp. 243-312). Springer. https://doi.org/10.1007/978-981-19-6345-2_41

Nuclear Charge Radii

W. Nörtershäuser and I.D. Moore

Abstract Nuclei are experimentally observed to have charge radii that show remarkably different trends to those that may be naively expected from liquid drop or droplet behaviour. Instead, its variation with proton and neutron numbers exhibits diverse patterns that offer a unique insight into the structure of atomic nuclei and fundamental symmetries. The techniques developed to measure nuclear charge radii during the last 50 – 70 years have become increasingly sensitive and are nowadays applied to determine differential changes throughout the nuclear landscape from the lightest to the heaviest elements. While elastic electron scattering and muonic-atom spectroscopy has been applied almost exclusively to stable isotopes, optical and particularly laser spectroscopy has become a unique tool to gain insight into the behavior of nuclear charge radii along isotopic chains of short-lived isotopes. Collinear laser spectroscopy and resonance ionization spectroscopy are the workhorses for these studies and have already been applied to a significant fraction of the nuclear chart. This chapter will provide an overview on the techniques that are used to determine nuclear charge radii and a selection of results from different regions of the nuclear chart to highlight some of the unique phenomena exhibited by this fundamental property.

Introduction

The first indications about the existence of a compact nucleus inside the atom being roughly 10,000 times smaller than the atom itself were obtained in the ex-

---

W. Nörtershäuser
Institut fur Kernphysik, Technische Universität Darmstadt, 64289 Darmstadt, Germany. e-mail: `wnoertershaeuser@ikp.tu-darmstadt.de`

I.D. Moore
Department of Physics, University of Jyväskylä, PB 35 (YFL), 40014, Jyväskylä, Finland. e-mail: `iain.d.moore@jyu.fi`

periments of Rutherford and co-workers (Geiger and Marsden, 1908, 1909, 1910). Alpha particles impinging on thin sheets of gold were found to be scattered at very large angles. The distribution of the scattered particles could be very well described by the existence of a minute massive centre carrying a positive charge (Rutherford, 1911). An upper limit of the nuclear size of a few 10 fm was obtained from these early experiments. Departures from Coulomb scattering caused by nuclear reactions were found for light elements and interpreted as a result of penetration of the α-particle trajectory into the nuclear region. From these experiments nuclear radii of a few femtometer were extracted (Pollard, 1935).

Since those days a much more accurate and diverse picture of nuclear radii has been established by a variety of experiments addressing nuclei across the nuclear chart. In Rutherford's approach the nuclear size was detected by the action of the strong nuclear force at the nuclear surface, which to lowest order does not differentiate between protons and neutrons. Alpha scattering as well as other experiments based on nuclear reactions are therefore usually sensitive to the matter radius of a nucleus. The majority of modern experiments applies the electromagnetic force as a probe to obtain nuclear radius information, which is sensitive to the charge distribution inside the nucleus. To lowest order, this is described by the root-mean-square (rms) charge radius $\sqrt{\langle r_c^2 \rangle}$, with

$$\left\langle r_{\mathrm{c}}^2 \right\rangle = \frac{1}{Z} \int \mathrm{d}^3 r \, r^2 \rho_{\mathrm{c}}(\vec{r}). \tag{1}$$

The preferred probes are electrons and muons, since they are point-like particles that are not subject to the strong force and their interactions can therefore be accurately described using quantum electrodynamics (QED). These can either be used as free particles in scattering experiments or bound to the nucleus inside atoms, subsequently probed by photons to obtain information about their binding energies. It should nevertheless be noted that leptons also interact by the weak force and can therefore be used to measure the neutron radius of a nucleus. Moreover, nuclear charge-changing reactions have lately been used to extract nuclear charge radii however are to a much larger extent model dependent.

Nuclear charge radii globally scale with the nuclear mass as $\sqrt[3]{A}$ but complex interactions between protons and neutrons lead to appreciable isotopic variations which are related to phenomena including halo structures, nuclear shell closures, shape changes, shape coexistence, or pairing correlations. The difference between charge radii, neutron and matter radii, can be used to determine sizes of nuclear halos or neutron skins. The latter can be related to the equation of state of nuclear matter and, thus, provides useful information for the structure of neutron stars. Moreover, nuclear charge radii are relevant for processes in weak interaction studies. These are a few reasons for the long-standing interest in nuclear charge radii and its impact in multidisciplinary topics.

The structure of this chapter is as follows. We will start with a summary of the techniques having dominantly contributed to our knowledge on nuclear charge radii, including a few that are currently under development. In the second part, selected results will be presented to highlight some of the principle features of charge radii that regularly occur within isotopic chains.

Experimental Techniques

The main techniques that have been used for the determination of nuclear charge radii are electron scattering, X-ray spectroscopy of muonic atoms and isotope shift measurements in optical electronic transitions. All are based on the electroweak interaction between a structureless lepton (e^-, μ^-) and an extended hadronic system composed of quarks and gluons interacting via the strong force. The electromagnetic interaction is mediated via the exchange of virtual photons and this process can be treated rigorously in QED. The extended particle is represented by its form factors, on which the definition of a charge radius can be based on an equal footing for all three cases as will be discussed below.

Electron Scattering

Electron scattering allows one in principle to determine the radial charge distribution $\rho_c(r)$, while all other techniques discussed in this chapter provide only integral quantities of $\rho_c(r)$, particularly the mean-square (ms) charge radius $\langle r_c^2 \rangle$ and higher even moments such as $\langle r_c^4 \rangle$. Hence, it also offers the means to connect characteristic radial moments, based on the ratio of the different radial moments that can be calculated using $\rho_c(r)$.

In electron scattering, the differential cross section $d\sigma(E,\theta)/d\Omega$ for an electron that impinges with energy E on a target and is scattered at an angle θ into the solid angle $d\Omega$ is measured. The energy of the scattered electron is usually determined with a magnetic spectrometer. Care has to be taken that only the contribution from elastically scattered electrons is measured, while inelastically scattered electrons from M1, E2 and higher multipolarities are excluded. Other critical factors include scattering from target impurities or the target holder. Moreover, the incoming beam energy and beam current has to be measured and controlled precisely.

In non-relativistic scattering theory, the incoming electron beam of energy E along the z-axis is represented as a plane wave $\psi_{\text{in}} \sim e^{ik_{\text{in}}z}$ with wave vector $k_{\text{in}} = \sqrt{2m_e E/\hbar}$. According to Huygens principle, outgoing spherical waves are created at all points of the scattering potential, which is here the nuclear charge distribution $\rho_c(\vec{r})$. The scattered wave is written as

$$\psi_{\text{scat}} \sim f(\theta,\varphi)\,\frac{e^{ik_{\text{scat}}r}}{r}, \tag{2}$$

where the second factor represents the spherical wave originating at the scattering centre and the scattering amplitude $f(\theta,\varphi)$ represents the modification of the spherical wave caused by the interference of the waves scattered at different points of the potential $\hat{V}(\vec{r})$. The connection between the observed differential cross section and the scattering amplitude is given by

$$\left(\frac{\mathrm{d}\sigma}{\mathrm{d}\Omega}\right) = |f(\vec{k}_{\mathrm{scat}},\vec{k}_{\mathrm{in}})|^2 = |f(\theta,\varphi)|^2. \tag{3}$$

Energy conservation in elastic scattering on a fixed target (recoil neglected) requires $k_{\mathrm{in}} = k_{\mathrm{scat}}$: the k-vector will only change direction, which is indicated by the pure dependence of f on the polar and azimuth angles θ and φ with respect to k_{in}. Evaluation of the scattering amplitude in first order (the so-called plane-wave Born approximation, PWBA) with appropriate normalization factors results in

$$f(\vec{k}_{\mathrm{scat}},\vec{k}_{\mathrm{in}}) = \frac{m}{2\pi\hbar^2}\left\langle \psi_{\mathrm{scat}}|\hat{V}|\psi_{\mathrm{in}}\right\rangle. \tag{4}$$

Introducing the momentum transfer to the scattered particle $\vec{q} = \hbar\Delta\vec{k} = \hbar(\vec{k}_{\mathrm{scat}} - \vec{k}_{\mathrm{in}})$, $|\Delta\vec{k}| = 2k\sin(\theta/2)$, the matrix element in Eq. (4) can be written as (neglecting normalization factors)

$$\left\langle \psi_{\mathrm{scat}}|\hat{V}|\psi_{\mathrm{in}}\right\rangle \sim \int \mathrm{e}^{i\left(\vec{k}_{\mathrm{scat}}\cdot\vec{r}\right)} V(\vec{r})\mathrm{e}^{-i\left(\vec{k}_{\mathrm{in}}\cdot\vec{r}\right)}\mathrm{d}^3r = \int \mathrm{e}^{i(\Delta\vec{k}\cdot\vec{r})}V(\vec{r})\mathrm{d}^3r, \tag{5}$$

which is the three-dimensional Fourier transform of the potential.

For scattering of an electron on a point-like charge $V(r) = Ze\delta(r)$, the classical Rutherford formula

$$\left(\frac{\mathrm{d}\sigma}{\mathrm{d}\Omega}\right)_{\mathrm{Rutherford}} = |f(\theta)|^2 = \left(\frac{2mZe^2}{4\pi\varepsilon_0}\right)^2\frac{1}{q^4} \equiv \left(\frac{1}{4\pi\varepsilon_0}\frac{Ze^2}{4E_{\mathrm{kin}}}\right)^2\frac{1}{\sin^4(\theta/2)}, \tag{6}$$

is obtained. The introduction of a spatially distributed (normalized) charge density $\rho(r)$ will modify the cross section by the square of the so-called form factor usually denoted $F(q^2)$

$$\frac{\mathrm{d}\sigma}{\mathrm{d}\Omega} = \left(\frac{\mathrm{d}\sigma}{\mathrm{d}\Omega}\right)_{\mathrm{Rutherford}}\cdot\left|F\left(q^2\right)\right|^2. \tag{7}$$

According to Eq. (4), $F(q^2)$ is the three-dimensional Fourier transform of the charge distribution. For $\rho_{\mathrm{c}}(\vec{r}) \equiv \rho_{\mathrm{c}}(r)$ being spherically symmetric, the angular integration can be carried out and the relation

$$F(q^2) = \frac{4\pi\hbar}{q}\int_0^\infty \mathrm{d}r\,\rho_{\mathrm{c}}(r)\,\sin(qr/\hbar) \tag{8}$$

is obtained. Using Eq. (1), it can be shown that the form factor can be written as an expansion

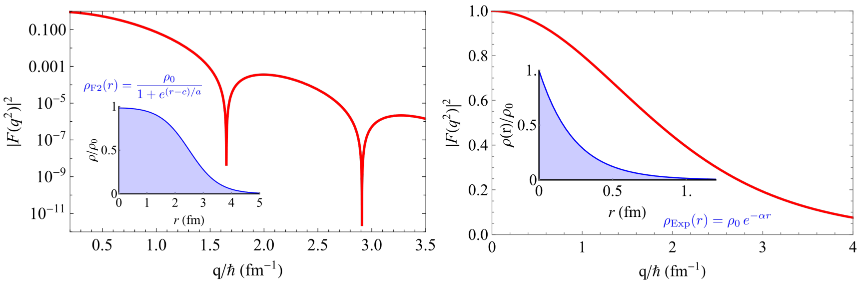

Fig. 1 Illustration of charge density distributions (blue) and the corresponding form factors (red). *Left panel*: Two-parameter Fermi distribution (Woods-Saxon) where ρ_{o} is the central nuclear density, c is the size at 50% density and a is related to the skin thickness t. The latter is usually defined as the radial extension of the region in which the density drops from 90% to 10% of the central density, which refers to $t = 4a\ln 3$. The parameters chosen in the plot ($c = 2.5\,\mathrm{fm}$, $a = 0.52\,\mathrm{fm}$) are a reasonable approximation for the ^{12}C nucleus. *Right panel*: Exponentially decreasing charge density as is approximately observed for the proton ($\alpha = 4.2\,\mathrm{fm}^{-1}$). While the form factor of the Fermi distribution has pronounced minima, the form factor of the exponential distribution is dipole-like and distinct structures are absent.

$$F(q^2) = 1 - \frac{1}{6\hbar^2}\left\langle r_{\mathrm{c}}^2\right\rangle q^2 + \cdots , \tag{9}$$

which directly relates the ms charge radius to the slope of the form factor at very small momentum transfer

$$\left\langle r_{\mathrm{c}}^2\right\rangle = -\, 6\hbar^2 \frac{\mathrm{d}F(q^2)}{\mathrm{d}q^2}\bigg|_{q^2=0} . \tag{10}$$

In the plane-wave Born approximation, the charge distribution of a spin zero ($I = 0$) nucleus with a spherically symmetric charge distribution can, thus, in principle be determined from the measured form factor by the Fourier transformation

$$\rho_{\mathrm{c}}(r) = \frac{1}{2\pi\hbar^2}\int_0^\infty \mathrm{d}q\, q^2 F\left(q^2\right) \frac{\sin(qr/\hbar)}{qr} . \tag{11}$$

The left panel in Fig. 1 shows a two-parameter Fermi distribution (inset) and the corresponding form factor. The distinct minima in $|F(q^2)|^2$ provide information on the nuclear size as can be easily obtained for a homogeneously charged sphere. Evaluating this model as is done in many textbooks results in the relation $qR \approx 4.5\,\hbar$ for the first minimum, from which the (model-dependent) radius can be inferred.

In principle, the complete charge distribution $\rho_{\mathrm{c}}(r)$ can be obtained from the form factor but since the measurement of $F(q^2)$ is restricted to a range between q_{min} and q_{max}, the Fourier coefficients can only be determined in the wavelength range from ${}^{2\pi}/_{q_{\mathrm{max}}}$ to ${}^{2\pi}/_{q_{\mathrm{min}}}$. In the early days, data was generally analysed using model distributions for the charge density $\rho_{\mathrm{c}}(r)$, commonly a two- or three-parameter Fermi model. This led to a model-dependence of the extracted nuclear densities and the corresponding moments. To overcome this drawback, model-independent analyses were proposed based on charge densities represented by a Fourier-Bessel series expansion with a cutoff radius R ($\rho_\mathrm{c}(r) = 0$ for $r > R_\mathrm{cut}$) (Dreher et al., 1974) and a sum of Gaussians (Sick, 1974) of the charge density. The former allows a separate treatment of the uncertainty caused by the experimental uncertainties of the measured data points and the uncertainty resulting from the lack of knowledge of the form factor for $q > q_\mathrm{max}$. However, it suffers from the fact that densities at widely separated radii are still coupled due to the radial behavior of the Bessel functions and due to the somewhat unphysical constraint to limit the number of Bessel coefficients to $N = R_\mathrm{cut} q_\mathrm{max}/\pi$. In the sum-of-Gaussian approach, interference between different components is only possible within the width of a Gaussian since it rapidly falls off. At large radii, the density is expected to behave like a Whittaker function governed by the proton separation energy. Further details regarding both procedures can be found in the original literature and the compilations of DeVries et al. (1987) and Fricke et al. (1995). The latter provide tables with sum-of-Gaussian parameters as well as Bessel-Fourier coefficients obtained from elastic electron scattering data for most of the stable isotopes. We note that the electron scattering measurements were rarely performed for momentum transfers larger than $2.5\,\mathrm{fm}^{-1}$, which limits the knowledge on $\rho_\mathrm{c}(r)$ but does not impose a severe limitation for the extraction of $\langle r_\mathrm{c}^2 \rangle$. While charge radii from elastic electron scattering have not been reported for heavier nuclei during the last years, light nuclei have been in the focus of such measurements, in particular for the extraction of the form factors and sizes of the proton and the neutron.

Non-relativistic scattering theory as discussed so far, does not take into account the electron spin. The differential cross section for scattering an unpolarized electron beam on a spinless point-like nucleus with charge Ze is the Mott cross section, having an additional correction term of $1 - \beta^2 \sin^2(\theta/2)$ compared to Rutherford scattering. The Mott cross section at relativistic electron energies ($\beta = v/c \approx 1$) and still neglecting the nuclear recoil can be expressed as

$$\left(\frac{\mathrm{d}\sigma}{\mathrm{d}\Omega}\right)_{\mathrm{Mott},\infty} = \left(\frac{1}{4\pi\varepsilon_0}\frac{Ze^2}{4E}\right)^2 \frac{\cos^2(\theta/2)}{\sin^4(\theta/2)} = \cos^2(\theta/2) \cdot \left(\frac{\mathrm{d}\sigma}{\mathrm{d}\Omega}\right)_{\mathrm{Rutherford}}. \tag{12}$$

The suppression of back-scattering ($\cos(\theta/2) = 0$ for $\theta = \pi$) is related to helicity conservation for $\beta \to 1$.

For light nuclei, the recoil term has to be included and leads to

$$\left(\frac{\mathrm{d}\sigma}{\mathrm{d}\Omega}\right)_{\mathrm{Mott}} = \left(\frac{\mathrm{d}\sigma}{\mathrm{d}\Omega}\right)_{\mathrm{Mott},\infty} \cdot \frac{1}{1 + \frac{2E}{Mc^2}\sin^2(\theta/2)} = \left(\frac{\mathrm{d}\sigma}{\mathrm{d}\Omega}\right)_{\mathrm{Mott},\infty} \cdot \frac{1}{(1+\tau)}. \tag{13}$$

The form factor that encodes the density information of the extended nucleus is now defined as the ratio of the measured cross section and the Mott cross section

$$\left|F(Q^2)\right|^2 = \frac{\left(\frac{\mathrm{d}\sigma}{\mathrm{d}\Omega}\right)_{\mathrm{exp}}}{\left(\frac{\mathrm{d}\sigma}{\mathrm{d}\Omega}\right)_{\mathrm{Mott}}}. \tag{14}$$

The relativistic scattering process is interpreted as an exchange of a virtual photon with three-momentum $|\vec{q}| = ({}^{2E}/_{c}) \cdot \sin({}^{\theta}/_{2}) = \hbar \Delta k$ between the electron and the nucleus. It corresponds to the momentum change of the electron. Usually the negative four-momentum of the space-like photon is used $Q^2 = -q^\nu q_\nu$ as the dynamical variable, indicated by $F(Q^2)$.

All nuclei with spin have a more complex form factor and with increasing spin the number of moments that contribute increases. Here, we will discuss only the proton, *i.e.*, scattering on a spin-$^1/_2$ particle. Due to the spin-orbit interaction, the form factor contains an electric and a magnetic contribution, which are taken into account in the Dirac and the Pauli form factor, F_1 and F_2, respectively. The Dirac form factor F_1 relates to the case when the proton spin does not flip during the interaction, whereas the Pauli form factor F_2 corresponds to processes including a spin flip of the proton. Formally, they are obtained from the scattering process of an electron with a spin-$^1/_2$ extended particle, which is given in QED at lowest order by the exchange of a single photon. This leads to a factor

$$\Gamma^\mu = \gamma^\mu F_1(Q^2) + \frac{i\sigma^{\mu\nu} q_\nu}{2Mc}\, \kappa F_2(Q^2)\,, \tag{15}$$

at the vertex between the virtual photon and the nucleus. Here, q_ν is the four-momentum of the virtual photon, γ^μ are the Dirac matrices, $\sigma^{\mu\nu} = (i/2)[\gamma^\mu, \gamma^\nu]$, M is the mass of the nucleus, and κ its anomalous magnetic moment. Experimentally, it is often more convenient to use a linear combination of these form factors which are called the electric and magnetic (Sachs) form factors

$$G_E(Q^2) = F_1 - \frac{Q^2}{4M^2c^2} F_2, \quad \text{and} \quad G_M(Q^2) = F_1 + F_2, \tag{16}$$

respectively. For $Q^2 \to 0$, they reduce to the overall charge and the magnetic moment, respectively. Using G_E and G_M, the electron scattering cross section is given by

$$\frac{\mathrm{d}\sigma}{\mathrm{d}\Omega} = \left(\frac{\mathrm{d}\sigma}{\mathrm{d}\Omega}\right)_{\text{Mott}} \left(G_E^2 + \frac{\tau}{\varepsilon} G_M^2\right) \tag{17}$$

with the polarization of the virtual photon $\varepsilon = (1 + 2(\tau + 1)\tan^2({}^{\vartheta}/_{2}))^{-1}$. This is the basis of the so-called Rosenbluth separation that takes advantage of the ε dependence of the structure term to extract G_E^2 and G_M^2 from cross-section measurements at different ε and constant Q^2 by varying the electron beam energy and the scattering angle. According to Eq. 17, one can then plot the measured reduced cross section $G_M^2 + {}^{\varepsilon}/_{\tau} G_E^2$ as a function of ε, *i.e.* the scattering angle θ. The form factors are then determined from the slope and the intercept of the fit.

The usual connection between the Sachs form factor and the rms charge radius is constructed by a Taylor expansion of the form factor in terms of Q^2,

$$\frac{G_E(Q^2)}{G_E(0)} = 1 - \frac{1}{6\hbar^2} \left\langle r_\mathrm{c}^2 \right\rangle Q^2 + \frac{1}{120\hbar^4} \left\langle r_\mathrm{c}^4 \right\rangle Q^4 - \ldots \tag{18}$$

The charge radius can therefore be obtained from the slope of the form factors at very low momentum transfer $Q^2 \to 0$

$$\left\langle r_{\mathrm{c}}^2 \right\rangle = -6\hbar^2 \left. \frac{G_E'(Q^2)}{G_E(0)} \right|_{Q^2=0} \equiv -6\hbar^2 G_E'(0), \tag{19}$$

similar to the non-relativistic case in Eq. (10). While in non-relativistic scattering theory, the form factor is the Fourier transform of the charge distribution (see above), this correspondence is lost in the relativistic case. Here, G_E and G_M can be interpreted as the Fourier transform of the electric and the magnetic distribution only in the so-called Breit frame, which corresponds to the frame in which only momentum and no energy is exchanged between the electron and the nucleus. The definition in Eq. (19) can instead be used to define the ms charge radius of an extended object.

Spectroscopic Determination of Nuclear Charge Radii in Hydrogen-Like Systems

The direct extraction of the nuclear charge radius R_c from level and transition energies requires a theoretical description of bound systems with an accuracy better than the contribution of the nuclear-size effect. As of today (2022) this has been established only for hydrogen-like systems. Of these, hydrogen, muonic hydrogen and muonic He$^+$ have been investigated by laser spectroscopy. Passive X-ray emission spectroscopy of muonic atoms is a long-established tool to extract nuclear charge radii and was used for almost every element with stable isotopes.

Laser Spectroscopy of Hydrogen

The binding and transition energies of electrons bound in atoms or ions are also affected by the size of the nuclear charge distribution. The level shift caused by the finite nuclear size can in lowest order be separated into a product of an electronic and a nuclear factor as shown in many textbooks, *e.g.*, (Bransden and Joachain, 2003),

$$\Delta E_{\mathrm{FS}} = E_{\mathrm{exp}} - E_{\mathrm{point}} = F \left\langle r_{\mathrm{c}}^2 \right\rangle = \frac{Ze^2}{6\varepsilon_0} \left|\psi(0)\right|^2 \left\langle r_{\mathrm{c}}^2 \right\rangle, \tag{20}$$

where F is the field-shift factor, which is dependent on the nuclear charge Z and the electron probability density at the nucleus $|\psi(0)|^2$, and $\left\langle r_{\mathrm{c}}^2 \right\rangle$is defined as the second moment of a three-dimensional charge distribution. Alternatively, one can start from the photon-nucleus vertex function, introduce the nuclear form factor and arrive at a level-energy shift of (Miller, 2019),

$$\Delta E_{\mathrm{FS}} = -4\pi(Z\alpha\hbar c)\hbar^2 G_{\mathrm{E}}'(0) \left|\psi(0)\right|^2 \delta_{\ell 0}, \tag{21}$$

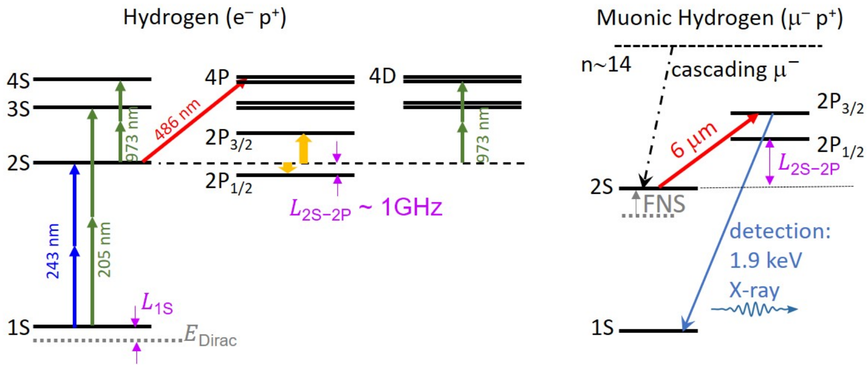

Fig. 2 Illustration of levels and transitions used in laser spectroscopy of hydrogen and muonic hydrogen. Level distances are not to scale. The proton radius is extracted from a measurement of either the 1S or the 2S–2P Lamb shift L, which includes the finite nuclear-size effect (FNS). The blue arrows denote the narrow (1.3 Hz) 1S–2S two photon transition while other two-photon transitions with natural linewidth of $\sim 1\,\text{MHz}$ are indicated by green arrows. Red arrows represent electric dipole transitions starting from the metastable 2S state. Wide arrows in orange are radiofrequency transitions. The dash-dotted line in the level scheme of muonic hydrogen symbolizes muons cascading from the $n \approx 14$ levels down to the metastable 2S state, the dominant cascade to the ground state (99%) is not shown.

which - by introducing Eq. (19) - also leads to Eq. (20). For hydrogen-like or muonic atoms, theory is sufficiently advanced to enable the direct determination of the mean-square nuclear charge radius $\langle r_c^2 \rangle$ using Eq. (20). Based on the Dirac equation and QED calculations, there are only two input parameters required in the QED calculation, the Rydberg constant R_∞ and the nuclear mean-square charge radius. In a simplified picture, s-level energies of hydrogen are given by

$$E(ns) = -\frac{R_\infty}{n^2} + \frac{L_{1S}}{n^3}\,\delta_{\ell,0} = -\frac{R_\infty}{n^2} + \frac{8172\,\text{MHz} + C_{1S} R_p^2(p)}{n^3}\,\delta_{\ell,0} \qquad (22)$$

where n is the principal quantum number, L_{1S} is the Lamb-shift of the 1S ground-state, which includes the finite nuclear size effect $C_{1S} R_p^2$ of the 1S state with $C_{1S} = 1.56\,\text{MHz}\,\text{fm}^{-2}$ and the rms proton radius R_p. The value of 8172 MHz is the QED prediction for the 1S Lamb shift assuming a point-like proton. Hence, the proton charge radius induces a fractional shift of a few 10^{-10} in optical transition frequencies. Precise measurements of two transitions in hydrogen can be used to extract R_∞ and L_{1S}. The determined 1S Lamb shift can then either be used to test QED by taking a proton radius from a different source or to extract the proton size assuming QED to be correct. The second case is of interest here.

Traditionally, the frequency of the narrow 1S–2S transition (Parthey et al., 2011) (linewidth 1.3 Hz) is combined with another transition starting from the metastable 2S level to extract L_{1S} and R_∞. The level scheme of hydrogen up to $n = 4$ and some of the used transitions are shown in Fig. 2. Starting from the metastable level, two photon transitions, like the indicated 2S–4S or 2S-4D have been used as well as dipole transitions to the P manifold, *e.g.*, 2S–4P. Using laser light at 205 nm, even the 1S–3S transition was induced with a cw laser in (Fleurbaey et al., 2018) and by direct frequency-comb spectroscopy with a colliding-pulse technique (Grinin et al., 2020). Alternatively, the charge radius can be extracted from the classical $2S_{1/2}$–$2P_{1/2}$ Lamb shift (Bezginov et al., 2019), which is actually the difference between the Lamb shifts of the two states. In this case, the Lamb shift and the nuclear-size contribution are about $8\times$ smaller ($\propto n^{-3}$), but since the Lamb-shift is directly addressed by a radiofrequency transition, the contribution of the nuclear size is about 0.014% of the transition frequency. Additionally, the extraction of the proton size does not require knowledge of the Rydberg constant since n does not change.

Laser Spectroscopy of Muonic Atoms

The higher mass of the muon, $m_\mu \approx 207\,m_e$, leads to a correspondingly larger splitting between levels of different n. The probability density at the nucleus increases by m^3, enhancing the nuclear size contribution by a factor of almost 10^7. This shifts the transition frequency into the laser-accessible region, $L_{2\mathrm{s}-2\mathrm{p}} \approx 49.818\,71\,\mathrm{THz}$ for a point-like nucleus, and provides a high sensitivity for the charge radius of $C_{2\mathrm{s}-2\mathrm{p}} \approx 1.2640\,\mathrm{THz\,fm}^{-2}$. The finite size effect contributes about 2% of the transition frequency and allows a very precise measurement of the proton radius even with moderate fractional accuracy of the transition frequency.

The prerequisite for these experiments are intense muon beams. The most intense beams are available at the πE5 muon beamline at the Paul Scherrer Institute (PSI) in Villingen, Switzerland. The experimental setup is schematically shown in Fig. 3.

Negative pions are produced in proton-nucleus collisions, transported to a cyclotron trap where they decay into high-energy muons (MeV), which are decelerated in a thin foil located in the center of the trap. The keV μ^- leave the trap and are transported along a torroidal magnetic field, which acts as a momentum filter into a 5 T solenoid. Here, they are stopped in a gas cell, filled with H_2, D_2 or He gas and captured by the atoms into Rydberg states of principal quantum number $n \approx \sqrt{m_\mu/m_e} \approx 14$. From there, the muons cascade down to low-lying states within $\approx 100\,\mathrm{ns}$, dominantly into the 1S ground state, but a small fraction, $\approx 1\%$, ends up in the metastable 2S state (lifetime $\sim 2\,\mu\mathrm{s}$), which is the starting point for laser spectroscopy. We note that the 2S lifetime decreases rapidly with pressure whereas the stopping power increases, requiring a delicate balancing to reach the optimal performance and efficiency. The laser system described in Pohl et al. (2010) is able to fire intense laser pulses within less than 1 µs after being triggered by the arrival of a muon at the gas cell. The titanium:sapphire laser creates a wavelength around 700 nm that is subsequently shifted into the 5.5–6 µm range by Raman scattering in a hydrogen cell. Muonic atoms in the 2S state are excited by a laser pulse into the $2p_{1/2,3/2}$ levels from which they relax into the ground state emitting X-rays, detected using avalanche photodiodes (see Fig. 2). A resonant laser pulse is therefore followed by an increased number of X-ray photons, which serve as the smoking gun for laser excitation.

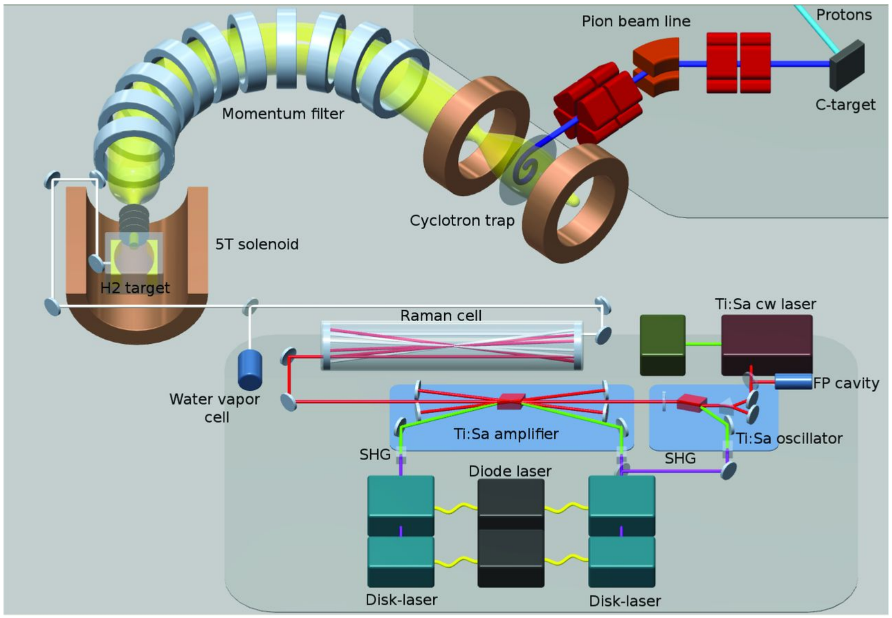

Fig. 3 Experimental setup for laser spectroscopy of muonic hydrogen and deuterium. The setup for muonic helium is similar, but a different laser system is used. For details see text. Figure reprinted with permission from Antognini et al. (2013), Copyright Science 2013.

Muonic-atom laser spectroscopy provides the most accurate and nuclear-model independent charge radii, about an order of magnitude more accurate than the best values from elastic electron scattering or hydrogen spectroscopy. This technique has been applied so far to hydrogen (Pohl et al., 2010), deuterium (Pohl et al., 2016) and helium (Krauth et al., 2021).

X-Ray Spectroscopy of Muonic Atoms

X-ray emission spectroscopy of muonic atoms is a technique that has been applied for a long time and has delivered charge radii for the majority of stable isotopes with 10^{-3} – 10^{-4} accuracy (Fricke et al., 1995). Muonic atoms are formed when negative muons (μ^-) are stopped in a target and captured by a target atom. Similar to the previous section, the muon cascades within a few ns into low-lying states that have a large probability density to be located at the nuclear site and are therefore strongly shifted in energy by the finite-nuclear-size effect. The most reliable information on nuclear charge radii from muonic atom X-ray spectra is obtained from $2p_{1/2,3/2} \rightarrow 1s_{1/2}$ (K_α-) transitions. It is, however, not the second moment of the charge radius that is extracted from these spectra, since the muons' wavefunction cannot be expected to be constant across the whole nuclear volume already in moderately heavy nuclei.

In order to extract information from the measured X-rays that can be related to rms charge radii, the following procedure is used. The Dirac equation of the muon in the nuclear field is numerically solved for the upper and the lower state of the X-ray transition assuming an analytical charge distribution, usually the two-parameter Fermi distribution (see inset Fig. 1, left)

In first-order perturbation theory the energy shift of a muonic transition between the initial level i and the final level f due to a variation $\Delta\rho_{\mathrm{c}}(r)$ of the spherical nuclear charge distribution can be written as

$$\Delta E_{\mathrm{if}} = 4\pi \int \Delta\rho_{\mathrm{c}}(r) \left[V_{\mu}^{(\mathrm{i})}(r) - V_{\mu}^{(\mathrm{f})}(r) \right] r^2 \, \mathrm{d}r, \tag{23}$$

with the potentials $V_{\mu}^{(\mathrm{i,f})}$ generated by the bound muon in the states i and f, respectively. The calculated energy difference between the two muonic states corresponds to the X-ray energy and the nuclear charge distribution is now modified in order to obtain agreement with the experimental spectrum, *i.e.*, the transition energies of the observed X-ray series. The rms radius of the nucleus under investigation can be evaluated directly from the parameterized distribution. However, it turns out that the value for $\sqrt{\langle r^2 \rangle}$ is strongly model-dependent since it changes considerably as the skin thickness t is varied or alternative distributions are used. It has been shown that the numerically obtained potential difference $\Delta V_{\mathrm{if}} = V_{\mu}^{(\mathrm{i})}(r) - V_{\mu}^{(\mathrm{f})}(r)$ between the two muonic states connected by the K_{α} transition can be well approximated by the analytical expression $Br^k e^{-\alpha r}$ (Barrett, 1970). The constants B, k and α are fitted to get the best estimation to ΔV_{if} within the range in which the change in ρ_{c} is largest. The corresponding expectation value

$$\left\langle r^k e^{-\alpha r} \right\rangle = \frac{4\pi}{Ze} \int \rho_{\mathrm{c}}(r) r^k e^{-\alpha r} r^2 \, \mathrm{d}r, \tag{24}$$

is called the Barrett moment and has been shown to be largely insensitive to the details of the assumed nuclear density distribution, *e.g.* the skin thickness, and is therefore considered *model-independent*. An *equivalent* Barrett radius $R_{k\alpha}$ is introduced, by the implicit relation

$$\left\langle r^k e^{-\alpha r} \right\rangle = \frac{3}{R_{k\alpha}^3} \int_0^{R_{k\alpha}} r^k e^{-\alpha r} r^2 \, \mathrm{d}r. \tag{25}$$

$R_{k\alpha}$ is the radius of a sphere of constant charge density that has the same Barrett moment as the nucleus under investigation. Usually the limited knowledge of the nuclear polarization correction is reported as the dominant systematic error of the result.

The traditional experimental approach, last applied over 30 years ago, was limited to stable isotopes with sufficient amounts of target material to stop negative muons with a momentum of typically 30 MeV/c. The muX experiment now aims to expand this method to long-lived isotopes of which only microgram samples are available Wauters and Knecht (2021). In this experiment, muons are stopped in a compact 100-bar H_2 target with a small admixture of D_2. Through a series of transfer reactions,

$$\mu^- \to \mu^- p \to \mu^- d \to \mu^- Z, \tag{26}$$

muonic deuterium is formed (second step), slowed down by elastic collisions with the H_2 molecules until it reaches an energy of the order of 10 eV. In this energy region, hydrogen becomes quasi-transparent for μd atoms (Ramsauer-Townsend effect) and the muons are quickly transported to the walls and the target region where they are finally transferred to the high-Z atoms (last step). X-rays are then detected by an array of high-purity Ge detectors. The technique was first applied to measure the quadrupole moments of ^{185,187}Re Antognini et al. (2020) and will be applied for charge radii measurements, *e.g.*, of ^{226}Ra.

A similar approach, but in thin films of frozen hydrogen and deuterium, was proposed by Strasser et al. (2002) to perform muonic atom X-ray spectroscopy on very short-lived nuclei at on-line facilities. A thick layer of frozen $H_2 + 10^{-3}\,D_2$ is used to stop muons. The first transfer processes in Eq. (26) produce muonic deuterium. The μd atoms diffuse to a frozen pure D_2 layer (5 μm) on top of the H_2/D_2 layer in which short-lived isotopes can be implanted at typical beam energies of a few 10 keV. The muons are transferred to these impurity atoms and X-rays can be observed.

Combination of muonic and electronic data

While the muonic data provide Barrett-equivalent radii with high precision, most applications require information on rms nuclear radii. Data from elastic electron scattering can be used to determine the ratio V_n^{e} between the Barret-equivalent radius and the charateristic radial moment $\langle r^n \rangle^{1/n}$

$$V_n^{\mathrm{e}} = \frac{R_{k\alpha}^{\mathrm{e}}}{\langle r^n \rangle^{1/n}}. \tag{27}$$

For light elements $k \approx 2$, $\alpha \approx 0$ and, thus, the Barrett moment in Eq. 24 is very close to the second radial moment. It is therefore not surprising that the Barrett equivalent radius has almost the same value as the rms equivalent radius $\sqrt{5/3 \langle r^2 \rangle}$ (Fricke et al., 1995). Even for lead ($\alpha \approx 0.15$, $k \approx 2.33$), the deviation between the radii is only of the order of 1%. From electron scattering, V_n^{e} can be calculated to about an order of magnitude more precise than the radial moments $\langle r^n \rangle^{1/n}$ themselves and it is therefore an ideal tool to transform the muonic Barrett radius into an rms radius

$$\langle r^n \rangle_{\mu\mathrm{e}}^{1/n} = \frac{R_{k\alpha}^{\mu}}{V_n^{\mathrm{e}}}. \tag{28}$$

A comprehensive summary of results obtained from X-ray spectroscopy of muonic atoms and elastic electron scattering is provided in Fricke et al. (1995) and Fricke

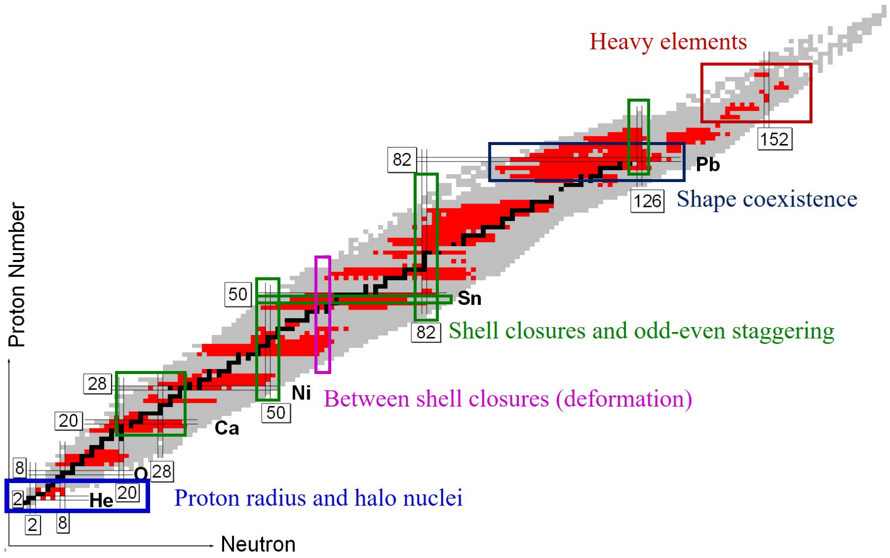

Fig. 4 Laser spectroscopy of radioactive isotopes indicating all known data published until March 2022. Black are stable and very long-lived isotopes, while radioactive isotopes that were investigated by laser spectroscopy at various on-line facilities worldwide are marked in red. Included in this figure are off-line measurements of elements for which stable isotopes do not exist. Colored rectangles indicate regions that are discussed in this chapter highlighting the requisite subjects given in the same color.

and Heilig (2004). These compilations contain the necessary information, *i.e.* $R^{\mu}_{k\alpha}$ and V^{e}_{n}, to calculate $\langle r^{n}\rangle^{1/n}$ for $n = 2,4,6$, as well as a detailed description of the procedure.

Optical Isotope Shift

Thus far we have discussed methods to extract the full nuclear size information, *i.e.* the rms radius $\sqrt{\langle r_{\mathrm{c}}^{2}\rangle}$. However, neither electron scattering nor X-ray spectroscopy of muonic atoms has yet been applied to short-lived isotopes since they require relatively large amounts of target material. For radioactive species another approach is used. Optical excitation of bound electrons and measurements of the small frequency differences along an isotopic chain provide changes between mean-square charge radii that are then combined with charge radius information of stable isotopes to extract absolute nuclear charge radii. Figure 4 shows the current status of all isotopes that have been investigated to date.

The isotopes of each element experience specific shifts and splittings in their resonance lines. A shift of the line center between two isotopes with mass numbers A and A' (the isotope shift, $\delta\nu_{\mathrm{IS}}^{AA'}$), depicted for some nickel isotopes in the middle panel in Fig. 5, arises from the difference in their nuclear masses M_A and $M_{A'}$, respectively, (mass shift, MS) and from the difference in nuclear volume (volume shift or field shift, FS)

$$\delta\nu_{\mathrm{IS}}^{AA'} = \nu^{A'} - \nu^{A} = K_{\mathrm{MS}} \cdot \frac{M_{A'} - M_A}{(M_A + m_e)(M_{A'} + m_e)} + F\,\delta\left\langle r_{\mathrm{c}}^2 \right\rangle^{AA'} . \tag{29}$$

The mass shift constant K_{MS} in a one-electron system is given to lowest order by $m_e\nu$ with the shift decreasing quickly as a function of increasing mass ($\propto 1/M^2$). A similar analytical expression for the mass shift constant is not available for systems with more than one electron due to the influence of electron-electron correlations, which are often termed specific mass shift (SMS) in contrast to the "normal" mass shift (NMS) in one-electron systems. The total mass shift is somewhat artificially divided into the two contributions, i.e., $K_{\mathrm{MS}} = K_{\mathrm{NMS}} + K_{\mathrm{SMS}}$, with $K_{\mathrm{NMS}} = m_e\nu$, which allows for the estimation of the contribution of electron-electron correlations from the measured mass shift constants. Empirically, it is found that the NMS dominates in typical $s \rightarrow p$ transitions, whereas significant SMS contributions are found if electronic states of higher angular momenta (d,f) are involved.

We note that it is also possible to extract the difference between the ms charge radius of a nuclear ground state and an excited isomeric state, provided that this state has a sufficiently long lifetime, at least in the millisecond range. The *isomer shift* is practically free from a mass-shift contribution since the mass difference between the two states is purely given by the nuclear excitation energy and is therefore negligible. Hence, even very small differences in radii can be determined with relatively high accuracy. A particularly illustrative example of high-resolution isomer shifts along a long chain of isotopes and isomers has been reported by Yordanov et al. (2016).

The field shift can be written as a product of the field-shift constant F and the difference in the mean-square charge radii of the two isotopes

$$\delta\left\langle r_{\mathrm{c}}^2 \right\rangle^{A,A'} = \left\langle r_{\mathrm{c}}^2 \right\rangle^{A'} - \left\langle r_{\mathrm{c}}^2 \right\rangle^{A} . \tag{30}$$

F is largely determined by the change in the electron probability density at the nucleus in the transition from the initial level i to the final level f, $\Delta\,|\psi(0)|^2 = |\psi(0)|_{\mathrm{f}}^2 - |\psi(0)|_{\mathrm{i}}^2$. The field shift approximately increases as $Z^2/\sqrt[3]{A}$. The relative contributions of the mass and the field shift to the isotope shift as a function of the atomic number is depicted in the left panel in Fig. 5. The field shift in light isotopes is only a 10^{-6} fraction of the mass shift, whereas in heavy isotopes the mass shift becomes negligible. Hence, it is obvious that for very light isotopes, the isotope shift *and* the mass shift must be determined with high precision in order to reliably extract the nuclear size contribution as will be discussed below.

We note that the pure dependence of the field shift on the second radial moment of the nucleus denoted in Eqs. (20) and (29) is a simplification, fully warranted only for light isotopes. In such cases, the electronic probability density $|\Psi(r)|^2 = |\Psi(0)|^2$ can be considered constant across the nuclear volume. For heavier isotopes,

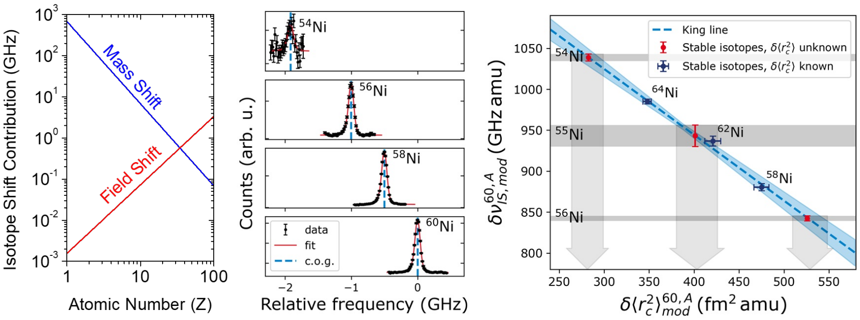

Fig. 5 *Left panel*: Approximate contributions of the mass shift and the field shift to the overall isotope shift. In light elements, the mass shift is the dominant contribution whereas beyond $Z \approx 35$ the field shift dominates. *Middle panel*: Resonances of four Ni isotopes. The shift in transition frequency between the isotopes is clearly visible. *Right panel*: King plot of Ni isotopes. The mass-modified isotope shift is plotted as a function of the mass-modified differential ms charge radii obtained from muonic atoms and elastic electron scattering. Blue data points are results for the stable isotopes with known radii, the blue line is the respective regression line. The red data points are the unstable isotopes and the arrows represent the projection onto the mass-modified nuclear charge radius. For details see text.

$\delta\left\langle r_{\mathrm{c}}^2\right\rangle^{AA'}$ must be replaced by the so-called nuclear parameter $\Lambda^{AA'}$ in which higher radial moments are also included

$$\Lambda^{AA'} = \delta\left\langle r_{\mathrm{c}}^2\right\rangle^{AA'} + \frac{C_2}{C_1}\delta\left\langle r_{\mathrm{c}}^4\right\rangle^{AA'} + \frac{C_3}{C_1}\delta\left\langle r_{\mathrm{c}}^6\right\rangle^{AA'} + \cdots \quad . \tag{31}$$

The so-called Seltzer coefficients C_2/C_1, etc. are tabulated in Seltzer (1969). The parameterization of the expectation values of higher even-order moments in terms proportional to $\delta\left\langle r_{\mathrm{c}}^2\right\rangle^{AA'}$ acts to recover a simple proportionality to changes in the ms charge radius. Additional relativistic corrections and screening effects have to be considered for the electron wavefunctions in heavier atoms, further increasing the nuclear-size contribution in these systems.

Determining the atomic constants K_{MS} and F of Eq. (29) is one of the critical steps in the extraction of $\delta\left\langle r_{\mathrm{c}}^2\right\rangle$. In the early days, semi-empirical estimates of the size of the specific mass shifts were used and the electron density at the nucleus was either inferred from the Goudsmit-Fermi-Segré rule based on fine-structure splittings of levels at high n or from the hyperfine structure, as discussed, *e.g.*, in Kopferman (1958). Nowadays, high-precision non-relativistic bound-state QED calculations with sufficient accuracy to treat the mass shift on a 10^{-6} level of accuracy are available up to five-electron systems, as demonstrated in Maaß et al. (2019). More complicated systems are treated with *ab-initio* approaches, *e.g.*, with multi-configuration Dirac-Fock calculations, many-body perturbation theory or coupled-cluster calculations Cheal et al. (2012). Typical uncertainties for the mass-shift and field-shift factors are of the order of 10%.

If nuclear charge radii information is available for three or more stable isotopes from X-ray spectroscopy of muonic atoms, elastic electron scattering or optimally even combined $\left\langle r_c^2 \right\rangle_{\mu e}$, the atomic factors can be extracted from respective isotope shift measurements by applying a so-called King-plot procedure King (1984). This is based on a modification of Eq. 29,

$$\frac{(M_A + m_e)(M_{A'} + m_e)}{M_{A'} - M_A} \delta \nu_{\mathrm{IS}}^{AA'} = K_{\mathrm{MS}} + F \, \frac{(M_A + m_e)(M_{A'} + m_e)}{M_{A'} - M_A} \, \delta \left\langle r_c^2 \right\rangle^{AA'} \quad (32)$$

$$\delta \nu_{\mathrm{IS,mod}}^{AA'} = K_{\mathrm{MS}} + F \, \delta \left\langle r_c^2 \right\rangle_{\mathrm{mod}}^{AA'}, \quad (33)$$

where the index “mod” (= modified) indicates expressions that have been multiplied with the inverse of the mass-dependence of the mass shift. The linear expression obtained in this way, allows the extraction of the mass and field shift factors from a linear fit to the known experimental data as is exemplified in the right panel in Fig. 5 for Ni isotopes. The blue points represent the modified isotope shifts as a function of the modified difference in ms charge radii obtained from the combination of muonic X-ray data and electron scattering information for the stable isotopes. The blue line is a linear regression line taking into account the uncertainties in x- and y-direction and the blue shaded region represents the 1σ-confidence interval. The slope of the line provides the field shift. Radii of short-lived nuclei can now be extracted as it is visually represented in the figure by the red points in a simplified way: the measured isotope shift provides the position along the line and the projection onto the x-axis indicated by the gray arrows provides the mass-modified ms charge radius difference. Its uncertainty does not only depend on the isotope shift uncertainty but also on the position of the isotope on the King-plot line.

If isotope shifts are measured in several lines (in the same or different ionization states) they can all be combined in a single multi-dimensional King fit, in order to get the best constraints for the nuclear charge radii of the short-lived as well as of the stable isotopes.

King plots are also regularly used to verify the consistency of the isotope shift data whereby mass-modified transition frequencies of two or even more transitions obtained using the same isotopes are plotted against each other. The points must then also form a straight line with high accuracy. The slope of these lines is determined by the ratio of the field-shift coefficients of the respective transitions. Recently, it has been suggested by Berengut et al. (2018) that deviations from the linear behavior may be an indication for the existence of beyond-standard-model (BSM) bosons that mediate forces between the electrons and the neutrons.

Finally, we note that the extracted value of $\delta \left\langle r_c^2 \right\rangle$ is nuclear-model independent. This separates it from the majority of the aforementioned non-optical measures of the nuclear charge distribution.

In the following sections, we discuss the main experimental techniques that aim to measure the optical isotope shift in order to determine the mean-square charge radius. As will be illustrated, the detection of an atomic resonance may be realized using a variety of spectroscopic methods that have been developed over the years, often tailored according to a specific chemical species or to the nature of the production facility. The studies leading to the current overview of the nuclear landscape (Fig. 4) have involved detection of resonance fluorescence, laser-induced nuclear orientation, optical pumping and resonance ionization. The choice of technique is often informed by the requirements of experimental sensitivity, efficiency as well as spectroscopic resolution (precision). As indicated in the left panel of Fig.5, it becomes clear that the required resolution to resolve the finite size effect of the nucleus varies dramatically depending on the element of interest, decreasing with increasing atomic number Z. For heavier elements, some loss of resolution can be tolerated in order to increase the efficiency, while this is not possible in the light- and medium-mass region. Notwithstanding the requirements in sensitivity and resolution, the spectroscopic techniques are additionally weighed against rapidly decreasing production rates as well as limitations set by the inherent lifetimes of the species of interest as one moves ever further from stability. The lifetime of the radioactive nuclei may be viewed as the critical limitation in the field in the longer term. The majority of facilities and spectroscopies now report, in favorable species, $\sim$ 1–10 ms as the minimum lifetime.

Resonance Ionization Spectroscopy

Laser resonance ionization takes advantage of the unique atomic level fingerprint as well as the resonant laser–atom interaction. By optically exciting the atom (or, in some cases, the ion) from either the atomic ground state or a low-lying thermally populated metastable state, ionization can be achieved via a stepwise process that raises the electron towards the continuum. With a typical ionization potential of about 6 eV for the majority of elements, an excitation ladder may contain two (or more) resonant excitation steps that can be rather easily saturated. Generally, the cross section for a strong transition between low-lying states is given by $\sigma_{\text{res}} = \lambda^2/2\pi \sim 10^{-10}\,\text{cm}^2$. As the excitation probability is given by $\mathrm{d}W(t) = \sigma \cdot J(t) \cdot \mathrm{d}t$, a laser beam with an intensity of $\sim 10^{18}$ photons/cm^2/s, or $100\,\text{mW/cm}^2$, can saturate a resonant transition for an excited state lifetime of 10^{-8} s. The final step that ionizes the atom is traditionally the “bottleneck” of the multi-step process. Direct non-resonant ionization into the continuum is unfavorable due to a cross section several orders of magnitude lower, $\sigma_{\text{i}} \sim 10^{-17}\,\text{cm}^2$. The requirement on the laser intensity is only within reach of pulsed laser systems, and several online facilities use commercially available pump lasers (solid state, copper vapour or excimer lasers) if a non-resonant ionization step is required. This low cross section can be enhanced by 2–3 orders of magnitude when ionization proceeds via excitation into high-lying Rydberg states (followed by electric field ionization, infra-red irradiation or collisional ionization) or via the excitation of an autoionizing state, which decays rapidly into an ion and a free electron. We note that laser spectroscopy can also be used to probe the convergence of a Rydberg series to make a precise measurement of the ionization potential as performed recently for the actinide element nobelium by (Chhetri et al., 2018). We refer the interested reader to the extensive texts of Letokhov (1987) and Hurst and Payne (1988) for a thorough theoretical treatment of the multi-step process as well as a range of applications.

The resonant laser–atom interaction inherently leads to one of the most attractive features of laser resonance ionization, the high degree of selectivity in the process. The difference in the atomic structure, isotope shifts and hyperfine structures, provide the elemental selectivity. If narrow-band lasers are used, it is also possible to discriminate between nuclear ground and isomeric states due to differences in nuclear spins and electromagnetic moments. We define the selectivity of a single optical excitation as the probability of exciting the selected isotope over the probability of exciting a neighboring isotope. By assuming a simple model of two Lorentzian peaks, a quantitative estimate of the selectivity can be given,

$$s \sim 4 \cdot (\mathit{\Delta}/\mathit{\Gamma})^2 \text{ when } \Delta \gg \Gamma, \tag{34}$$

where $\mathit{\Delta}$ is the frequency difference between neighbouring elements, isotopes or isomers, and $\mathit{\Gamma}$ is the interaction linewidth. As an example, in the resonant $4d^9 5s\,^3\mathrm{D}_3 \to 4d^9 5p\,^3\mathrm{P}_2$ transition in palladium, the isotope shift $\delta\nu^{105,106}$ is $\sim$345 MHz and the natural linewidth $\mathit{\Gamma}$ is $\sim$20 MHz. Under the assumption of negligible line broadening, the isotopic selectivity s is $\sim$1200. The elemental selectivity on the other hand can theoretically reach $\sim 10^{17}$ due to the frequency difference with a neighboring element, $\mathit{\Delta} \sim 10^{15}$ Hz. In a multi-step excitation process, a simplified estimate of the total selectivity S can be made as the product of the selectivity of each step. Moreover, with the coupling to mass spectrometry, the isotopic selectivity can be further enhanced.

The sensitive detection of ions (or nuclear decays) as a function of laser frequency compared with the detection of resonantly scattered photons (to be discussed in connection with collinear laser spectroscopy), has led to resonance ionization spectroscopy (RIS) becoming a powerful spectroscopic tool for the determination of charge radii and electromagnetic moments of nuclei. Indeed, the method of RIS was first demonstrated in 1971 for rubidium atoms by Ambartsumyan et al. (1971). Throughout the following years, multi-step laser resonance ionization was refined and used in many laboratories for applications ranging from the separation of uranium isotopes to the ultra-sensitive detection of single atoms and rare isotopes. It was in 1983 that these sensitive methods finally entered the field of contemporary nuclear physics, aiding in the exploration of fundamental properties of short-lived isotopes produced at radioactive beam facilities. These facilities employ particle accelerators to induce nuclear reactions in order to provide short-lived nuclei for immediate study using a variety of spectroscopic techniques. At the isotope separator on-line (ISOL) facility, IRIS, Gatchina in Russia, isotope shifts and hyperfine structures of long-lived samples of rare-earth isotopes $^{145-149}$Eu were investigated by Alkhazov et al. (1983). This initial work was performed “off line”, with samples accumulated on foils and transferred into an atomic beam oven. Spectroscopy was performed in a perpendicular geometry to reduce the effects of Doppler broadening, with one of the lasers scanned over the isotope shifts and hyperfine structure. This mode of operation was not however suitable for shorter-lived isotopes, and therefore an “on-line” technique was soon implemented by Fedoseyev et al. (1984). The mass-separated beam was stopped in a tantalum tube from which isotopes could be evaporated, collimated and ionized.

Numerous developments were made throughout the 1980s, often by different groups in parallel. The laser technology was refined, in particular with improvements in the spectral resolution, and more efficient ion source techniques emerged. For example, at ISOLDE, pulsed-laser induced desorption (PLID) methods improved the efficiency of RIS performed with low duty-cycle lasers (10 Hz) by matching the repetition rate laser system with pulsed thermal atomic beams Krönert et al. (1987). In parallel with ISOLDE, the same approach was employed by groups at McGill University, Montréal, Canada, and the Institut de Physique Nucléaire d’Orsay (IPN, Orsay, France), used in the study of isotopic chains of gold and platinum isotopes at the ISOCELE separator at Orsay Lee et al. (1987, 1988); Duong et al. (1989). Later, a programme of measurements was initiated at ISOLDE using the COMPLIS (COllaboration for spectroscopy Measurements using a Pulsed Laser Ion Source) setup Sauvage et al. (2000). In that work, neutron-deficient isotopes of gold and the refractory elements platinum and iridium were uniquely accessed at ISOLDE as daughter atoms of parent mercury ions. The latter are readily produced and implanted into a graphite catcher. Following a suitable decay time, the daughter atoms are desorbed using a pulsed laser, resonantly ionized and detected.

A more detailed overview of these developments can be found in the review of Fedosseev et al. (2012) in which a summary of the ionization schemes applied throughout the periodic table for both radioactive beam production and RIS is provided. In the following, we discuss the most common methods of “in-source” spectroscopy that are used for the exploration of nuclear charge radii at radioactive beam facilities today and present the most recent variants that are still under development.

- **Hot cavity in-source resonance ionization spectroscopy:** In the early 1990s, a particularly efficient method of laser spectroscopy was demonstrated on-line by using the laser ion source of a mass separator by Alkhazov et al. (1992), a technique which nowadays is referred to as “in-source” spectroscopy. A hot cavity, connected to the production target, provides a confinement of atoms which are interrogated with multiple laser frequencies spatially overlapped into the tube. High-repetition rate lasers (of order 10 kHz) are required to ensure a suitable temporal overlap with the diffusion time of an atom through the cavity. The mass-separated ion yield is measured as a function of the wavelength of one of the pulsed lasers used in the resonant excitation process. With a typical operating temperature of 2000 K, the atomic spectral lines have a broad thermal velocity distribution according to $\Delta\nu_\mathrm{D} = 7.16 \times 10^{-7}\ \nu_0\sqrt{T/M}$, where T is the cavity temperature in K, M the atomic mass number and ν_0 the atomic transition frequency. Such high temperatures prohibit the study of light elements whose atomic structure perturbations are fully masked. However, using a narrow-band pulsed laser with a linewidth approaching 1 GHz, the resolution is sufficient for the study of heavy elements whose isotopes exhibit large isotopic shifts (dominated by the field shift) and large hyperfine structures (HFS). For example, a precision of better than 100 MHz in HFS measurements of stable thallium isotopes

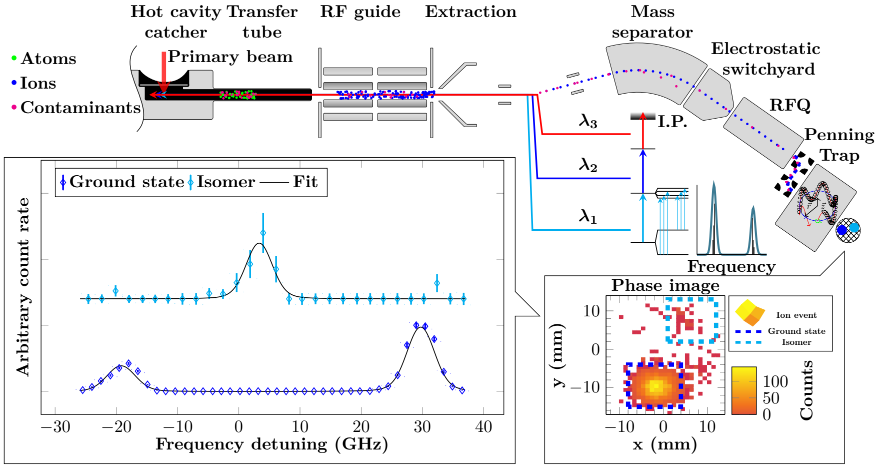

Fig. 6 Principle of in-source RIS. Radioactive isotopes are created in nuclear reactions of a high-energy primary beam with a thick target, or a thin target following which reaction products recoil into a catcher. Atoms diffuse out of the catcher/target material and effuse into a transfer tube where they are selectively ionized via a multi-step laser ionization process. After acceleration and mass separation, the ions are then delivered to a detection system. In this novel variant, the ions are cooled, bunched and delivered to a Penning trap for high-resolution mass separation enabling almost background free identification of ground and isomeric states. Tagging of the detected states as a function of laser frequency allows for isotope/isomer shift as well as hyperfine structure measurements.

by in-source spectroscopy was realized at ISOLDE RILIS, an accuracy sufficient for the study of mean-square charge radii variations along isotopic chains (Fedosseev et al., 2003). The high selectivity and efficiency of the RIS process is impressively highlighted in a measurement of ^{182}Pb ($\tau_{1/2}$=55 ms), 26 neutrons from stability, with a detection rate of 1 ion per second (De Witte et al., 2007).

In recent years, in-source RIS experiments have been complemented by sensitive ion detection techniques, for example, multi-reflection time-of-flight (MR-TOF) devices for isobaric purification offer a means of achieving high counting sensitivity as demonstrated for mercury isotopes by Marsh et al. (2018). At the IGISOL facility, RIS was combined with the high mass resolving power of the phase-imaging ion-cyclotron resonance (PI-ICR) method, traditionally implemented for Penning trap mass spectrometry (Eliseev et al., 2013), to study the nuclear charge radii of silver isotopes, crossing the N=50 magic neutron number below ^{100}Sn (Reponen et al., 2021). As illustrated in Fig. 6, a three-step resonant laser ionization scheme selectively ionizes the effusing atoms following diffusion out of a hot graphite catcher. After electrostatic acceleration, the ions are mass-separated and bunched in a gas-filled radiofrequency quadrupole cooler and buncher. The bunched ions are injected into the JYFLTRAP Penning trap and manipulated according to their mass-dependent cyclotron motion. Following release from the trap, the ions are finally detected on a position-sensitive detector.

The ground or isomeric state can be selected for analysis by applying software gates, and a hyperfine spectrum can be constructed by correlating the ions to the tagged laser frequency. This method has demonstrated a detection sensitivity of one ^{96}Ag resonant ion every five minutes. Such low event rates are only possible if the background rate is similarly low, a condition satisfied with the PI-ICR detection method.

- **In-gas-cell resonance ionization spectroscopy:** The fast and universal thermalization of nuclear reaction products in an online gas cell was originally pioneered at Jyväskylä by Ärje et al. (1985), addressing the inability of the traditional ISOL method to produce refractory species. Evacuation times are much shorter in comparison to the hot cavity ion source, as low as $\sim$1 ms for small volume gas cells. The combination with the resonant ionization process was demonstrated several years later at the LISOL facility by Van Duppen et al. (1992). In this variant, high-purity ($<$1 ppb) argon rather than helium gas is favored for the enhancement of the neutralization process. Complexities associated with losses of the photo-ions during evacuation from the gas cell due to recombination in the presence of buffer gas electrons created by the primary beam, led to a dual-chamber design in which the stopping and laser ionization volumes are physically separated, presented by Kudryavtsev et al. (2009). Gas flow transports atoms from the stopping volume to a chamber which can be illuminated by laser light either longitudinally along the extraction axis, or transversely close to the gas-cell exit hole. The latter geometry is often employed in combination with upstream ion collector electrodes to collect any residual non-neutral fraction prior to laser ionization, thus assisting in an improved selectivity. The evacuation time of the laser-irradiated volume is longer than the time between two successive laser pulses, guaranteeing that all atoms are irradiated by the laser light.

  Similar to the drawback of using the hot cavity ion-source for RIS, environmental effects in the gas cell are detrimental to the spectral linewidth of an atomic transition. Operational pressures between 200–500 mbar result in experimentally observed pressure broadening and shift due to collisions with buffer gas atoms, limiting the spectral resolution to a few GHz. At the LISOL facility, in-gas-cell RIS has been used to explore neutron-deficient isotopes of copper and silver, as well as neutron-deficient $^{212-215}$Ac (Granados et al., 2017) located near the N=126 shell closure. At the KEK Isotope Separation System (KISS), RIKEN, a doughnut-shaped gas cell was developed by Hirayama et al. (2017) for extracting target-like fragments produced in multi-nucleon transfer (MNT) reactions. KISS initially focused on nuclear spectroscopy studies of neutron-rich isotopes in the region of N=126. Recently, the in-gas-cell RIS method has been applied to the study of HFS and isotope shifts of $^{196-198}$Ir by Mukai et al. (2020), as a first step to probe the evolution of nuclear deformation in this transitional region of the nuclear chart.

  Resonance ionization spectroscopy in an argon buffer gas cell has also been coupled with radioactive decay detection in the so-called RADRIS (RAdiation Detected Resonance Ionisation Spectroscopy) method, the development of which has been pursued at the University of Mainz and GSI. In this technique, the nuclides of interest are neutralized on a filament wire and are evaporated for subsequent in-gas-cell RIS by the application of a short heating pulse. Electrical fields guide the photo-ions towards a suitable particle detector that is sensitive to the resulting decay radiation. The sensitivity and efficiency of RADRIS was highlighted in successful measurements of isotope shifts for superdeformed americium fission isomers Backe et al. (1998, 2000). This method has proven to be the optimal tool for studying short-lived isotopes produced via heavy-ion fusion-evaporation reactions with low production rates. RADRIS has been applied to the study of transuranium nuclides, with separated fusion-evaporation products stopped in a gas cell at pressures of about 100 mbar. By detecting the radioactive decay of photo-ions, spectroscopy may be performed on target production rates as low as $10\,\mathrm{s}^{-1}$ and nuclei with half-lives approaching 1 ms. The culmination of this technique was realized online at GSI, with resonance ionization spectroscopy performed on the transfermium element nobelium (Z=102), in single atom-at-a-time quantities by Laatiaoui et al. (2016). An overview of the past achievements and prospects of laser spectroscopy in buffer gas cells for the study of superheavy elements can be found in the reviews of Backe et al. (2015) and Block et al. (2021).

- **Perpendicularly illuminated laser ion source and trap (PI-LIST):** A newly developed variation of the in-source RIS method has been realized in combination with the so-called Laser Ion Source and Trap (LIST) device. LIST was originally proposed by Blaum et al. (2003) to improve the quality of the beam extracted from a hot cavity ion source, by decoupling the laser ionization volume from the production and evaporation regions. In this manner, the problem of surface ionization leading to isobaric contamination can be alleviated. As indicated in the left panel of Fig. 7, neutral atoms are allowed to diffuse from the hot cavity (atomizer) into a radio-frequency quadrupole (RFQ) ion guide, with surface ions and electrons suppressed using repelling voltages. Background-free laser ionization takes place within the RFQ and an impressive suppression of surface ions by up to four orders of magnitude has been realized. This mode of operation is however accompanied by a loss factor of 20 in ionization efficiency compared to the traditional in-source mode as the suppression of resonant ions produced within the hot cavity is unavoidable. Experiments on in-source laser spectroscopy of $^{216-218}$Po have been performed with the LIST as well as a nuclear decay study of ^{219}Po (Fink et al., 2015). Importantly, no systematic effects were seen in comparison to the in-source RIS method. This development, when coupled with efficient methods of ion counting, offers enhanced selectivity that will enable the continuation of studies in the region north-east of ^{208}Pb that have been notoriously difficult to access due to intense isobaric contamination.

  A refinement of the LIST device, indicated in the right panel of Fig. 7, has been proposed in order to reduce the effect of the overlap of the effusing atomic beam and counter-propagating laser beams that limits the spectral resolution of RIS to about 1–2 GHz. The spectroscopy laser is introduced perpendicular to the atomic beam (perpendicularly illuminated LIST, PI-LIST), resonantly ionizing a localized volume within the RFQ structure. To fully exploit the Doppler reduction, the

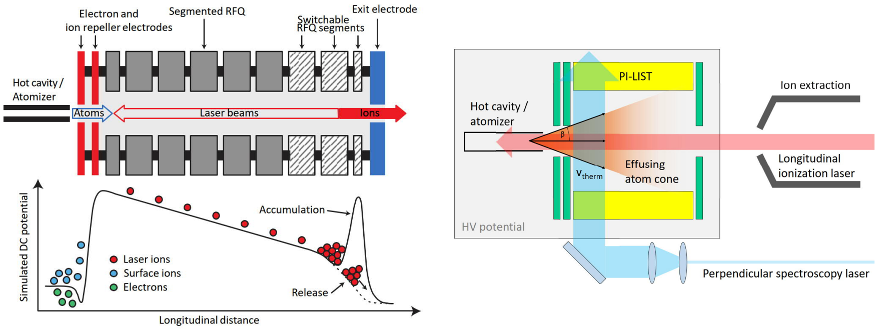

Fig. 7 *Left panel*: Schematic overview of the original Laser Ion Source and Trap, LIST. Ions and electrons from a hot cavity ion source are prevented from entering an RFQ device using repelling fields. Resonant laser ionization of the atomic plume proceeds along the central axis of the structure, with the possibility to extract ions in bunches using controllable DC voltages on the segmented rods. *Right panel*: Principle of the perpendicularly illuminated LIST, PI-LIST, variation. The number of velocity classes is significantly reduced by introducing the spectroscopy laser in a perpendicular geometry between the segments of the RFQ. Figure courtesy of R. Heinke.

linewidth of the scanning laser must be appropriately reduced. This can be done using a laser system in which a pulsed Ti:sapphire laser cavity is seeded with cw radiation from a commercial, narrowband laser. An overall efficiency loss factor of 100 to 300 has been observed between standard in-source and perpendicular broad-band laser operation, with a further loss factor when operating in a narrowband mode as reported by Heinke et al. (2016). Nevertheless, the method has been successfully applied at the offline RISIKO mass separator at the University of Mainz for high-resolution spectroscopy of long-lived isotopes $^{97-99}$Tc by Kron et al. (2020). Hyperfine structures and isotope shifts were investigated from spectra with linewidths below 100 MHz. The PI-LIST is currently being implemented at ISOLDE with first experiments planned to explore the charge radii of neutron-rich actinium isotopes in a region known for octupole correlations.

- **In-gas-jet resonance ionization spectroscopy:** In a similar manner to the motivation of the PI-LIST for improving the spectral linewidth of in-source RIS, spectroscopy in the gas jet environment has been proposed in recent years to improve the resolution of in-gas-cell RIS. In this approach, highlighted in Fig. 8, neutral reaction products are ionized upon exit from a gas cell and are captured by the radio-frequency field of a quadrupole or sextupole ion guide. In order to meet the requirements of a good geometrical overlap between the gas jet and laser beams, as well as achieving minimal disturbance to the spectral line, the gas flow characteristics must be well understood. To ensure an efficient ionization, a high-repetition-rate laser system is a mandatory requirement in order to have a good temporal overlap between the laser pulses and the atom velocity in the gas jet. For example, for a repetition rate of 10 kHz and a supersonic Ar gas jet with velocity 550 m s^{-1}, a laser–atom overlap of 5.5 cm is required. De-Laval nozzles produce suitable supersonic flow of approximately constant temperature and density, resulting in a considerable reduction in spectral linewidth in comparison with in-gas-cell RIS. A proof-of-principal study was carried out at the Leuven ISOL separator, with in-gas-jet spectroscopy performed by Ferrer et al. (2017) on ^{214,215}Ac with a spectral resolution of 300 MHz, a selectivity of $\sim$200 and an efficiency of $\sim$0.5%. If one is able to minimize the jet divergence then a spectral resolution below 200 MHz is feasible. Resonance ionization spectroscopy has recently been used to support the refinement of the gas-jet technique by mapping the local flow properties (Ferrer et al., 2021). Future experiments at online facilities will use the method to study the atomic and nuclear structure of the actinide and transactinide elements.

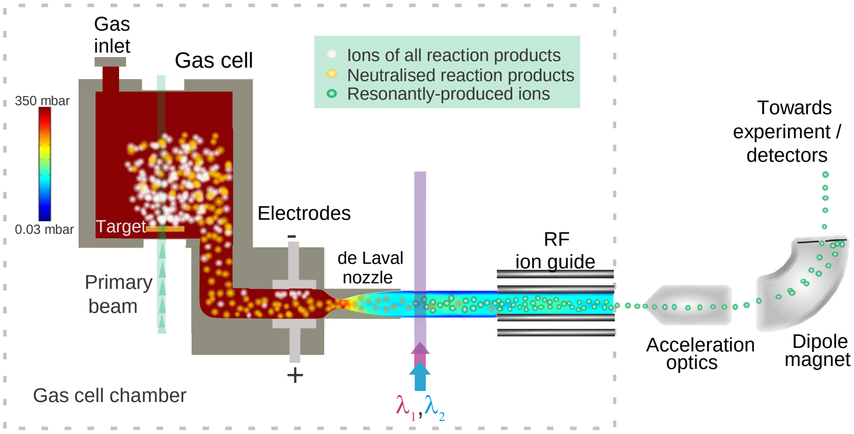

Fig. 8 Principle of in-gas-jet RIS. Fusion-evaporation recoils are thermalized and neutralized in purified argon, and are transported from the stopping chamber towards the exit of the gas cell. Atoms are evacuated from the cell through a de Laval nozzle, forming a supersonic gas jet. A pair of electrodes before the nozzle collect any non-neutralized ions, increasing the selectivity of the method. The resulting collimated jet provides a suitable environment for medium-resolution spectroscopy, with RIS performed in a localized geometry formed by the intersection of the laser beams with the gas jet. Photo-ions are then accelerated, mass-separated and delivered to experimental stations either for detection as a function of laser frequency, or for further ion manipulation. Figure courtesy of R. Ferrer.

Collinear Laser Spectroscopy

Collinear laser spectroscopy (CLS), also called collinear fast-beam laser spectroscopy, was proposed by Kaufman (1976) and first realized for the spectroscopy of molecular HD$^+$ by Wing et al. (1976). The application of the method at an on-line facility was demonstrated at the University of Mainz by Anton et al. (1978), where

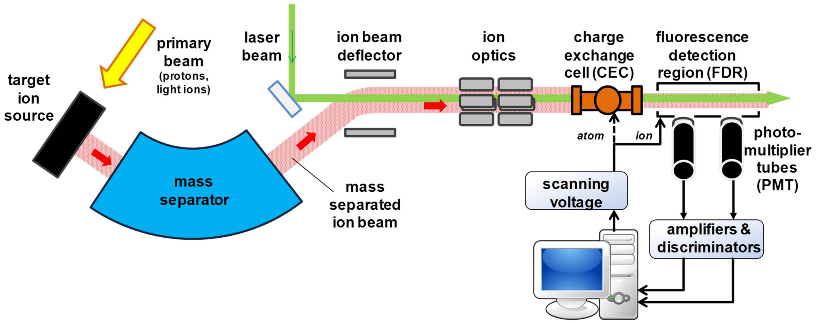

Fig. 9 Principle of classical collinear laser spectroscopy (CLS). Radioactive isotopes are produced by bombardment of a target with a high-energy primary beam either in a target container (*e.g.* at CERN-ISOLDE) or within a gas cell (*e.g.* at the JYFL-IGISOL). After extraction and mass separation the ion beam is superimposed with a collimated laser beam using electrostatic deflector plates. Additional ion-optical systems match the ion beam profile for maximum overlap with the laser beam. The ions are either neutralized in a charge exchange cell (CEC) or directly studied in the fluorescence detection region (FDR). When the scanning voltage applied to the CEC or the FDR results in a beam velocity that fulfills the resonance condition of an atomic transition with the Doppler-shifted light, the laser induced fluorescence in the FDR is detected by photomultiplier tubes (PMTs) and recorded after signal processing in the data acquisition system.

short-lived cesium isotopes produced at the TRIGA research reactor were the first species to be studied Schinzler et al. (1978). Soon thereafter, the COLLAPS experiment was installed at ISOLDE by Mueller et al. (1983) and became the prototype for several collinear setups worldwide.

The technique requires ion beams with low emittance and of typically 30–60 keV beam energy, readily available at ISOL facilities, and are thus often called ISOL-type beams in contrast to the high-energy (at least several MeV/u, up to GeV/u)), large emittance beams at in-flight facilities. A typical experimental setup at an ISOL or IGISOL facility is depicted in Fig. 9. It consists of an ion source, where the short-lived isotopes are produced and ionized by various processes. Surface ion sources, plasma ion sources as well as resonance laser ionization are usually applied. The ion source is at a high positive potential (typical 30–60 kV), such that the ions extracted are accelerated towards ground potential. The ions are then mass-separated in a magnetic sector field and transported to the collinear laser spectroscopy beamline, where an electrostatic deflector is used in order to superimpose the ion beam with a laser beam that either copropagates with the ion beam (“collinear geometry”) or counterpropagates (“anticollinear geometry”).

The electrostatic acceleration has two consequences for laser spectroscopy: First it leads to a large Doppler shift of the transition frequency ν_0. The laser in the laboratory frame must therefore provide the frequency

$$\nu_L = \frac{\nu_0}{\gamma(1-\beta\cos\theta)} = \nu_0\frac{\sqrt{1-\beta^2}}{1-\beta\cos\theta} \tag{35}$$

with the ion velocity in terms of the speed of light $\beta = \upsilon/c$, the relativistic time-dilation factor $\gamma = 1/\sqrt{1-\beta^2}$ and the angle between the ion beam and the laser beam direction θ. For exact collinear (+, $\theta = 0$) or anticollinear (–, $\theta = \pi$) geometry, this simplifies to

$$\nu_\pm = \nu_0\,\gamma(1\pm\beta) = \nu_0\sqrt{\frac{1\pm\beta}{1\mp\beta}}. \tag{36}$$

According to Eq. (35), there are two ways to change the frequency in the reference frame of the ion. Either the laser frequency is tuned or the ion-beam velocity is changed by applying an accelerating or decelerating voltage (Doppler tuning).

The second effect of the static acceleration, and the foundation of the achievable high resolution in CLS, is a longitudinal kinematic compression of the velocity distribution. The width ΔE_s of the ions' energy distribution stays constant during the acceleration since all ions experience the same potential difference. The width of the corresponding velocity spread of the ion beam $\Delta\upsilon_\mathrm{b}$ in the beam direction is accordingly reduced compared to the velocity spread $\Delta\upsilon_\mathrm{s}$ in the ion source as (Kaufman, 1976)

$$\Delta\upsilon_\mathrm{b} = \frac{1}{2}\sqrt{\frac{\Delta E_\mathrm{s}}{eU}}\cdot\Delta\upsilon_\mathrm{s}. \tag{37}$$

In practice, residual Doppler widths on the order of 50–100 MHz are usually obtained in CLS and the line profile can be described sufficiently well by a Gaussian or a Voigt profile.

Since isotopes of different masses are accelerated with the same voltage, they obtain different velocities and this artificial isotope shift has to be considered in the analysis. Therefore, the ion beam energy has to be known with sufficient accuracy. This includes the high-voltage potential at the ion source as well as the voltage at the acceleration stage for Doppler tuning. This can be achieved by using precision high-voltage dividers (Krieger et al., 2011) or calibrating the high-voltage by measuring precisely known isotope shifts as demonstrated, *e.g.*, in Gorges et al. (2015).

A variety of techniques for the observation of the resonant interaction between the atomic species and the laser has been developed in the last decades in order to extend laser spectroscopy into increasingly exotic regions of the nuclear chart. They differ in sensitivity and applicability. First, techniques based on fluorescence detection will be discussed.

- **Fluorescence detection of ions:** The conceptually easiest approach is a direct measurement of transitions in the ion starting from the ionic ground state, which is usually the only significantly populated level. In this case, Doppler tuning is performed by applying a variable voltage at the detection region. The sensitivity depends on the light-collection and detection efficiency of the optical system but also strongly on the spectroscopic properties of the ion. The dominant background stems from scattered laser light and limits the sensitivity reached with continuous ion beams to typically about 10^3–10^4 ions/s for strong transitions on closed two-level systems. Sensitivity can be considerably worse in cases where the ion has a multitude of low-lying fine-structure or hyperfine states, and the population of the state addressed with the laser is rapidly depopulated. Scattered laser light can be effectively suppressed with optical filters when the relaxation of the excited level proceeds preferably along another decay branch with a sufficiently different wavelength.

- **Fluorescence detection of atoms:** Transitions from the ground state of ions are often in the UV and sometimes even in the VUV region and are thus not accessible by the available laser systems. This is of particular concern for alkaline metal ions, ions of the rare gases and practically all non-metal ions, but also many metals. In these cases it is necessary to neutralize the beam and perform laser spectroscopy on the atoms. Neutralization is achieved in a charge-exchange cell filled with a low pressure of alkaline metal vapor. Two types are in operation, either the ion beam traverses the alkaline cell directly as described by Mueller et al. (1983) or an alkaline gas jet intersects the ion beam perpendicularly. A comparison of these types is provided in Klose et al. (2012). The neutralization is usually quite efficient (typically 50%) but the process leads to a large number of populated atomic states and only the atoms in the level of interest will contribute to the signal. Large populations of specific atomic states can often be achieved in cases of (nearly) resonant charge transfer, *i.e.*, if the binding energy of the targeted atomic level coincides with the ionization potential of the alkaline atom. The article by Vernon et al. (2019) provides extensive tables of calculated level populations obtained after charge exchange. The population of metastable atomic states is particularly useful if the atomic ground state does not provide laser-accessible transitions, as is the case, *e.g.* for all noble gases. Doppler-tuning with neutral beams is performed by applying the reacceleration voltage to the charge exchange cell. Since the interaction with the laser sets in as soon as the ions are neutralized, the distance to the fluorescence detection region should be short to avoid depopulation of the atomic level before the detection region is reached. For bunched beams (see below), this can be suppressed by switching the laser beam accordingly, *e.g.*, with an electro-optical modulator as demonstrated by Voss et al. (2013).
- **Photon-Ion Coincidence Detection:** The dominating background in conventional CLS with fluorescence detection is scattered laser light. This can be reduced if photons registered by the photomultipliers are only accepted while an ion traverses the detection region. This is realized by placing a particle detector downstream from the detection region and feeding the signal together with the suitably delayed PMT-pulse into a coincidence unit Eastham et al. (1986). The technique is applicable with low-intensity ion beams having little isobaric contamination.
- **Bunched-Beam Fluorescence Detection (Fig. 10a):** A more effective coincidence detection is possible if the arrival of the ions at the fluorescence detection region is deterministic. This is now state of the art and implemented at most on-line facilities using gas-filled radio-frequency quadrupole (RFQ) cooler and bunchers (Nieminen et al., 2002). These devices are linear Paul traps and consist of four segmented rods to which an RF-signal and a DC signal is applied. The RF signal is shifted by 180 degrees between the pairs of opposing rods, such that

radially an effective potential minimum is created at the axis, while DC potentials at the rod segments are used to create an additional axial trapping potential. The device is filled with helium at low pressure ($\sim 10^{-1}$ mbar) and is mounted on a high-voltage platform at approximately 100 eV below the potential of the ion source. The axial potential at the RFQ entrance just allows the ions to enter. Within the RFQ, the ions undergo elastic collisions with the helium atoms, gradually losing energy and being cooled into the minimum of the axial potential well. A potential set at the exit electrode ensures the ions are held within the cooler. After a typical accumulation time $T_{\mathrm{acc}} \sim 50\,\mathrm{ms}$, depending on the ion beam intensity and the half-life of the isotope, the exit electrode potential is pulsed down and an ion bunch of typically $T_{\mathrm{bunch}} \sim 5\,\mu\mathrm{s}$ temporal length is released, reaccelerated to ground potential and transported to the collinear beamline.

With the known time-of-flight of the ions from the cooler and buncher to the detection region, only photons detected in coincidence with a gate defining the laser and ion bunch interaction time are counted. This reduces the background from scattered laser light by a typical factor of $R = T_{\mathrm{bunch}}/T_{\mathrm{acc}} \sim 10^{-4}$, increasing the detection limit by about two orders of magnitude. For ions with a corresponding nuclear ground state spin I=0 and a fast transition on a closed two-level system that allows the generation of multiple photons from a single ion, bunched-beam spectroscopy of species with production rates as low as 50 ions/s has been demonstrated by Miller et al. (2019). The sensitivity of bunched-beam fluorescence spectroscopy can be limited by beam-induced background if the beams are isobarically contaminated. Background photons are generated either in inelastic collisions with residual gas or the "afterglow" behind the charge-exchange cell, caused by the spontaneous emission from higher lying states populated in the neutralization process.

While the ions are accumulated inside the RFQ, they can also be addressed with (pulsed) laser light to obtain an efficient redistribution of population following the excitation of ground states into a selected metastable state. This can be advantageous if the electronic transitions from the ionic ground state are unsuitable for efficient spectroscopy. Unlike the high-resolution continuous-wave lasers used for collinear laser spectroscopy, pulsed lasers, that readily access higher harmonics and a broader wavelength range, are used for pumping. The enhanced metastable population survives the transport to the downstream Doppler tuning region, and spectroscopy can be performed using transitions from the metastable state in preference to the ground state as demonstrated for Mn ions by Cheal et al. (2009).

While fluoresence detection is widely applicable, it does not often provide the highest sensitivity since the collection efficiency of photons, emitted in a solid angle of 4π is usually far below 1%. Contrary, charged particle detection can have efficiencies close to 100% since the particles can be collected by electric and magnetic fields and guided to highly efficient low-background detectors. Additionally, particle-selective identification steps can be included to further reduce background, which is – apart from the application of optical filters – not possible in fluorescence detection.

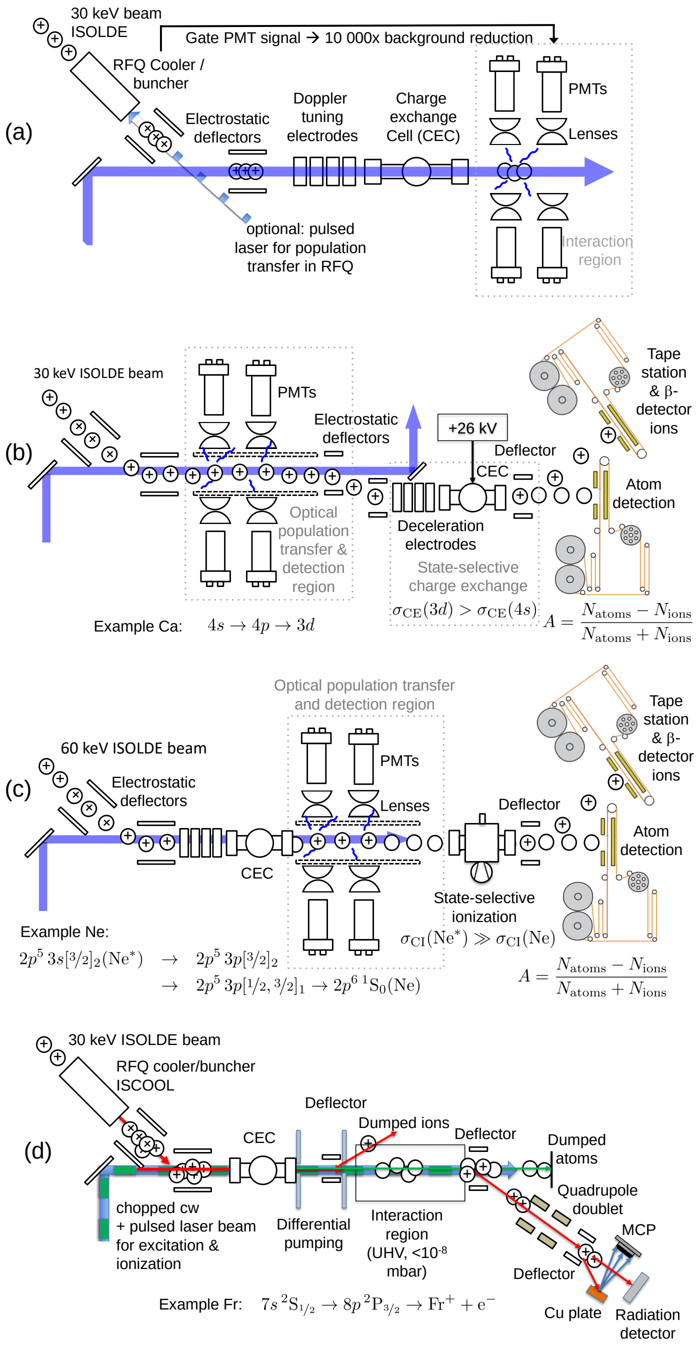

Fig. 10 High-sensitivity variants of collinear laser spectroscopy (CLS). (a) Bunched-beam fluorescence spectroscopy, (b) state-selective charge exchange, (c) state-selective collisional ionization, and (d) collinear resonance ionization (CRIS). For details see text.

- **State-selective charge exchange (Fig. 10b):** The interaction of multi-level ions or atoms with laser light will inevitably lead to a population transfer between specific states. If these states exhibit significantly different properties in collisions, this can be used for the detection of the laser resonance. The first application of this concept was state-selective charge exchange as demonstrated by Silverans et al. (1987). It has been used for spectroscopy on alkaline-earth ions, which exhibit a favorable level scheme for this technique. For calcium (in other cases only the principal quantum number n has to be adjusted), excitation of the $4s_{1/2} \rightarrow 4p_{1/2,3/2}$ resonance transition is followed by a decay branch into the metastable $3d_{3/2,5/2}$ levels. Even though the branching ratio is only about 5%, a few excitation cycles are sufficient to transfer a significant fraction of ions into the metastable state. Detection exploits the difference in cross section for charge exchange of ground-state ions compared to ions in the metastable state. The cross sections depend on the beam energy and differ by about a factor of three at about 4 keV. Hence, the CLS setup for this type of spectroscopy includes a long optical pumping region at the full beam energy, before the beam is decelerated to 4 keV and enters into a charge exchange cell. Separation of the charge states after the cell is accomplished by electrostatically deflecting the remaining ions and counting the atoms and ions using particle-sensitive detectors. As long as the laser is not in resonance, the charge exchange process is inefficient and the rate detected by the atom detector stays low. Resonant interaction of the laser light with the $4s \rightarrow 4p$ transition will transfer ions into the $3d$ state and the charge-exchange rate increases, leading to an increased signal at the atom detector while the rate at the ion detector will decrease. Counting both species and taking the asymmetry signal $A = (N_{\text{atom}} - N_{\text{ion}})/(N_{\text{atom}} + N_{\text{ion}})$ allows for signal normalization in case of fluctuating production rates of the radioactive isotope. Isobaric beam contamination can deteriorate the otherwise low-background of this technique since it will increase the rate either on the atom or the ion detector. For short-lived species, this can be handled by replacing the particle detectors by nuclear radiation detectors in combination with a tape transport system (Silverans et al., 1985; Garcia Ruiz et al., 2017).
- **State-selective ionization (Fig. 10c):** This method has first been used for the measurement of noble gases by Neugart et al. (1986) and Borchers et al. (1987) and is based on the different collisional ionization cross sections of excited states and the ground state. Charge exchange of noble gas ions on the closest alkaline atom leads to a substantial population of the $np^5(n+1)s\,[3/2]_2$ states that are metastable against decay to the $np^6\,{}^1\mathrm{S}_0$ ground-state. These states have ionization energies of only $\sim 4\,\mathrm{eV}$ and are prone to collisional ionization. Laser excitation into an $np^5(n+1)p$ state will be followed by spontaneous decay into the $np^5(n+1)s\,[1/2, 3/2]_1$ levels, which inevitably return to the atomic ground state, with typically 10 eV higher binding energy and very small ionization cross section. Collisional ionization is realized at the full beam energy in a gas-filled chamber after the optical interaction region. Ion-atom separation and detection can be performed analogously to the state-selective charge exchange technique.

- **Optical pumping and β-asymmetry detection:** This method is based on the parity violation in β-decay. The β-particle has a preferred emission direction with respect to the nuclear spin. Optical pumping with circularly polarized light in the electron shell on a suitable transition will lead to a nuclear polarization through the hyperfine interaction. Implanting the polarized ensemble into a crystal located in a strong magnetic field and measuring the asymmetry of the emitted β-particles along and opposite to the magnetic field, a resonance spectrum of the atomic transition can be obtained since asymmetries will only be produced if the laser is in resonance with the transition. This technique is limited to isotopes with nuclear spin and therefore not applicable for isotopes with even numbers of protons and neutrons. Its advantage is that the polarized ensemble implanted into the crystal can subsequently be used to study nuclear moments with very high precision by β-detected nuclear magnetic resonance (β-NMR). For charge radii studies it has been used for ^{29,31}Mg by Yordanov et al. (2012).
- **Collinear Resonance Ionization (Fig. 10d):** A combination of the methods of collinear laser spectroscopy and multi-step photoionization was proposed 40 years ago for ultra-low abundance detection of rare radioactive isotopes by Kudriavtsev and Letokhov (1982). The technique promised significant advantages for beams with high isobaric contamination which require efficient background suppression. The first online demonstration was performed on fast atomic beams of radioactive ytterbium isotopes by Schulz et al. (1991), almost ten years after the initial proposal, with resonance ionization proceeding from a metastable atomic level populated following neutralization of the fast ion beam in a charge exchange cell. The limiting factor in this initial experiment was primarily associated with the duty-cycle losses due to the laser–atom interaction. Combined with a low population of the metastable state and the inefficiency of the ionization process, experiments on radioactive beams would require production rates of order 10^6 atoms/s.

  The implementation of gas-filled radio-frequency quadrupole cooler and buncher devices provided the opportunity to address the duty-cycle losses. The release time for the ion bunches is synchronized with the duty cycle of the pulsed laser system, enabling a 100% temporal overlap. In the collinear resonance ionization spectroscopy (CRIS) method, any remaining non-neutral fraction after the charge exchange cell is deflected in a differential pumping region before the laser–atom interaction region. Differential pumping addresses the main source of background in collinear resonance ionization experiments, namely collisional re-ionization with rest-gas molecules. Vacuum conditions are nominally maintained below 5×10^{-9} mbar. Resonantly-produced ions are deflected towards a charged-particle detector after leaving the interaction region. At ISOLDE, the CRIS experiment features a detection setup that also includes a decay spectroscopy station, with a rotating wheel housing thin carbon implantation foils and silicon detectors. Gamma rays emitted from decay products may be detected by up to three high-purity germanium detectors placed around the implantation point. This has allowed for successful decay-assisted laser spectroscopy, for example α-decay measurements as a function of laser frequency to uniquely identify the atomic hyperfine structure components associated with low-lying nuclear states in neutron-deficient Fr isotopes as reported by Lynch et al. (2014). In recent years, ongoing developments in both resolution and sensitivity have resulted in laser spectroscopy of exotic species with production rates as low as 20 ions/s, such as ^{78}Cu with a resonant ion detection rate of $0.05\,\mathrm{s}^{-1}$ (de Groote et al., 2017) and with half-lives as low as 5 ms for ^{214}Fr, scanned and identified using the decay spectroscopy station (Farooq-Smith et al., 2016).

A short summary indicating the approximate experimental spectroscopic linewidths achievable with the techniques we have introduced in this section, along with the type of laser used in the method, is provided in Table 1.

Table 1 Resolution of the optical techniques typically applied for measuring isotope shifts of short-lived isotopes.

Method	Linewidth	Resolution limit	Lasers
In-source RIS	∼GHz	Doppler broadening	Pulsed
In gas-cell RIS	∼GHz	Pressure broadening	Pulsed
In gas-jet RIS	∼200 MHz	Residual Doppler	Pulsed, cw-seeded
Collinear RIS (CRIS)	∼50 MHz	Natural linewidth	Pulsed + cw / cw-seeded
Collinear spectroscopy	∼50 MHz	Natural linewidth	cw

Charge Exchange Cross Sections

In recent years, an alternative methodology was suggested to derive the radii of proton distributions in neutron-rich nuclei using nuclear reactions on separated relativistic ion beams. This is particularly useful if very exotic and rarely produced isotopes are to be investigated. In peripheral collisions of heavy ions at intermediate energies (*e.g.* 300–900 MeV/u), the projectile might lose one or more protons. The corresponding charge-changing cross section σ_{cc} reflects a collision probability of the valence proton(s) from the projectile with the target nucleus and is therefore sensitive to the projectiles' proton distribution. The underlying principle of σ_{cc} measurements is the transmission method. The number of particles N_0 of the isotope of interest impinging on a target is counted and compared to the number of projectiles that leave the target without a change in proton number $N_{Z=Z'}$ based on event-by-event information. The ratio $R = N_{Z=Z'}/N_0$ is measured with and without target and the charge-changing cross section is defined as $\sigma_{\mathrm{cc}} = -1/t \ln\left(R_{\mathrm{out}}/R_{\mathrm{in}}\right)$ with t being the target thickness. Measurements without target (R_{out}) are performed to eliminate reactions that happen in the detectors and might therefore be falsely attributed to proton loss in the target. Appropriate corrections for proton-pickup reactions of the projectile ($Z_{\mathrm{final}} > Z_0$) have to be included in cases for which the corresponding cross-section is not negligible. The relation between σ_{cc} and the point-proton distributions is provided by finite-range or zero-range optical-limit Glauber-type calculations Glauber (1970) using a phenomenological correction factor $F(E)$

$$\sigma_{\mathrm{cc}} = 2\pi \int b\,[1 - T^p(b)]\,F(E)\,\mathrm{d}b, \tag{38}$$

$$T^p(b) = \exp\left[-\left(\sigma_{pp} \int \rho_p^{\mathrm{targ}} \rho_p^{\mathrm{proj}} + \sigma_{np} \int \rho_n^{\mathrm{targ}} \rho_p^{\mathrm{proj}}\right)\right]. \tag{39}$$

Here, b denotes the impact parameter and $\sigma_{pp}\,(\sigma_{np})$ the proton(neutron)-proton cross sections. $T^p(b)$ is a part of the transmission function, where ρ_p and ρ_n are the z-integrated density distributions of protons and neutrons, respectively, in the target and projectile nucleus as indicated. The method has been applied to Li, Be, B, and C isotopes, but only for carbon isotopes point-proton radii and charge radii were extracted by Kanungo et al. (2016). It should be noted that the technique cannot be applied to isotopes close to the proton drip-line since proton evaporation after neutron removal or inelastic excitation into states above the proton emission threshold cannot be excluded for nuclei with relatively low proton separation energies.

Dielectronic recombination

Another rather recent atomic physics technique to obtain high-precision isotope shifts involves electron recombination in highly-charged ions. This process utilizes a resonant channel of photo-recombination, namely *dielectronic recombination*. In brief, electron–ion recombination into a particular final recombined state may be represented as follows,

$$\mathrm{e}^- + A_i^{q+} \to A_f^{(q-1)+} + \hbar\omega, \tag{40}$$

and

$$\mathrm{e}^- + A_i^{q+} \to \left[A_j^{(q-1)+}\right]^{**} \to A_f^{(q-1)+} + \hbar\omega, \tag{41}$$

where q is the charge state of the ion with mass A and ω the frequency of the emitted photon. The first (direct) process is radiative recombination (RR), and is possible at all free electron energies. The second, dielectronic recombination (DR), involves a resonant channel whereby the free electrons have an incoming energy that matches the resonant excitation of a bound electron attended by the capture of the free electron into a highly excited (Rydberg) state of the highly-charged ion. The formed doubly-excited electronic state can decay either by an Auger process (the reverse of dielectronic capture) or by photon emission. The latter leads to an ion with a charge state reduced by one. Thus, the successful DR process can be considered the inverse of photoionization through an autoionizing state, whereas the RR process of Eq. (40) is the inverse of non-resonant photoionization. By studying the electron recombination rate as a function of the free-electron energy one obtains spectra

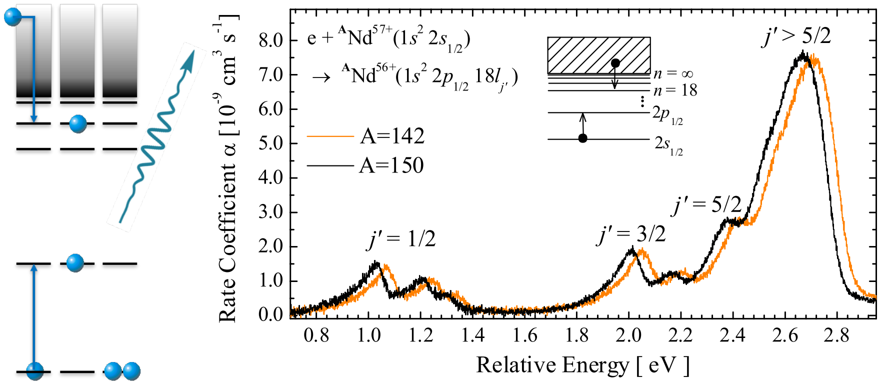

Fig. 11 *Left panel*: The three steps of the DR process according to Eq. (41): capture, doubly-excited state and stabilization by photon emission. *Right panel*: Dielectronic recombination of the Li-like neodymium isotopes ^{142}Nd^{57+} (orange line) and ^{150}Nd^{57+} (black line) in the energy range of the $1s^2 2p_{1/2} 18\ell_{j'}$ resonance groups. The labels indicate the individual fine structure components j' of the $n = 18$ Rydberg electron. (Reprinted with permission from Phys. Rev. Lett. 100 073201 Copyright 2008 American Physical Society).

associated with the DR resonances, whose positions give the atomic transition energies, isotope shifts and hyperfine structure. This is somewhat akin to precision X-ray spectroscopy – measuring at meV-precision atomic lines in highly-charged ions.

In general, dielectronic recombination has received a lot of theoretical attention due, in part, to its importance in the modeling of high-temperature plasmas. It is therefore of immediate interest for solar and other dense astrophysical plasma environments where it is the predominant electron recombination reaction. DR experiments involve highly-charged ions, either in a storage ring, *e.g.* the Experimental Storage Ring (ESR) at the GSI in Darmstadt, Germany, or in an electron beam ion trap (EBIT). In a storage ring experiment, the free electrons for DR are provided by the electron cooler used to cool the ions. At very low ion–electron collision energies, such experiments have enabled precision determination of the Lamb shifts in several highly-charged ions (Brandau et al., 2003). In order to determine precise isotope shifts, DR of a free electron with a very small kinetic energy, preferably below 10 eV, is required. This has been demonstrated by Brandau et al. (2008) for two neodymium isotopes, ^{142}Nd and ^{150}Nd, using the transitions $e^- + \mathrm{Nd}^{57+}(1s^2 2s_{1/2}) \rightarrow \mathrm{Nd}^{56}(1s^2 2pn\ell j)^{**}$, with ** denoting the doubly excited state created in the dielectronic capture. The interpretation of the resulting shifts of the resonance positions, clearly seen in Fig. 11, in terms of changes in ms charge radii in this simple three-electron system is very reliable, taking into account the nuclear size correction, relativistic and QED contributions. In contrast with optical isotope-shift studies, isoelectronic studies of different elements can be done to disentangle atomic and nuclear contributions. Such applications can be expected at the upcoming Facility for Antiproton and Ion Research (FAIR). Here, CRYRING@ESR is expected to provide two orders of magnitude higher resolution due to its advanced electron cooler including magnetic expansion, providing considerably lower longitudinal and transversal electron temperatures as detailed in Lestinsky et al. (2016).

Significance of Nuclear Charge Radii

While the spherical droplet model by Myers and Swiatecki (1969) suggests a smooth increase of the ms charge radius along an isotopic chain, the study of isotope shifts to elucidate $\delta\langle r_\mathrm{c}^2\rangle$ portrays a rather different picture. Emergent fine structure features caused by quantum effects in the structure of atomic nuclei are in clear evidence. Trends in the charge radii of light isotopes are often dominated by clustering effects, while in medium mass and heavy atoms a staggering of sizes between nuclei with odd and even neutron number is an omnipresent but still not fully understood feature. Prominent changes in the slope of the charge radii are observed at almost all shell closures, while away from shell closures rather dramatic changes arise from sudden onsets of deformation at a specific neutron number. Perhaps the most celebrated example of this is seen in the large shape staggering first observed in neutron-deficient isotopes of mercury. In this section, experimental and theoretical results on nuclear sizes across the nuclear chart will be discussed, starting with the proton radius up to charge radii of the heaviest elements.

The proton radius

The proton is the only stable baryon and one of the building blocks of matter. Understanding its structure based on quantum chromodynamics (QCD) is an enormous challenge due to the non-perturbative behavior of QCD calculations in the low-energy regime. Experimentally, the charge radius has been determined by electron scattering, laser and radio-frequency spectroscopy of ordinary hydrogen and on muonic hydrogen. While there have been inconsistent values from elastic electron scattering experiments spanning more than four decades, *e.g.* $R_p = 0.805(11)\,\mathrm{fm}$ reported in Hand et al. (1963) and $R_p = 0.862(12)\,\mathrm{fm}$ by Simon et al. (1980), more recent precision measurements of elastic electron scattering by Bernauer et al. (2010) as well as Lamb-shift measurements in hydrogen by Bourzeix et al. (1996), Schwob et al. (1999), and Udem et al. (1997) in combination with QED calculations seemed to have settled the inconsistency in favor of the larger proton radius around the millennium as shown in Fig. 12. Measurements on muonic hydrogen by Pohl et al. (2010) then indicated a considerably smaller proton radius. This discrepancy was termed the "proton radius puzzle" and led to a plethora of publications (for an overview, see the review by Pohl et al. (2013) for example) and speculations on whether muons might interact differently with protons than electrons, violating lepton universality. Since then, several new measurements were performed to resolve the proton radius puzzle. The 2S–4P transition was investigated in Beyer

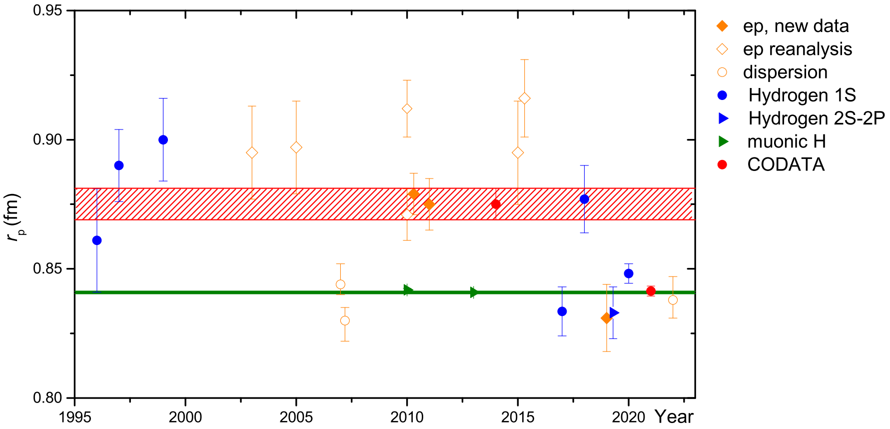

Fig. 12 Proton radius determinations since 2000. Data and references are taken from the Particle Data Group (Zyla et al., 2020). Additionally, early hydrogen results from Bourzeix et al. (1996), Udem et al. (1997), and Schwob et al. (1999), as well as the latest dispersion analysis data by Lin et al. (2021) are added. Open symbols represent results from reanalysis of published data whereas filled symbols are new measurements. Colors encode the applied technique: electron scattering (orange), hydrogen spectroscopy (blue) and muonic hydrogen spectroscopy (green). Red are the CODATA values from 2014 (uncertainty range indicated by the red lines) and from NIST (2022) The latter is mainly determined by the muonic hydrogen result from Antognini et al. (2013), with uncertainties represented by the green lines.

et al. (2017), starting from a well-controlled cryogenic source of 5.8-K 2S atoms prepared by two-photon excitation into a single hyperfine state. Contrary to the previous measurements performed on 2S atoms created by electron bombardment and, therefore, high thermal velocities and partially unresolved hyperfine structure, the new measurement resulted in a smaller charge radius in agreement with the muonic hydrogen experiment as depicted in Fig. 12. More recently, a direct measurement of the 1S–3S transition at 205 nm using room temperature hydrogen gas in Fleurbaey et al. (2018) supported again the larger CODATA value from 2014 published in Mohr et al. (2016). The same transition was remeasured using direct frequency-comb spectroscopy on cold hydrogen atoms and the second-order Doppler shift was determined at several low temperatures and extrapolated to 0 K. In combination with the 1S–2S two-photon transition, the Rydberg constant and the proton charge radius were extracted by Grinin et al. (2020). As shown in Fig. 12, the radius is closer to the muonic radius but disagrees by 2.9 standard deviations from the old CODATA value. The muonic hydrogen value is further supported by a new measurement of the classical 2S–2P Lamb shift in atomic hydrogen by Bezginov et al. (2019) as well as a result from elastic electron-proton scattering at very low momentum transfer (PRad experiment) performed at Jefferson Laboratory by Xiong et al. (2019). The latter does not use a magnetic spectrometer and has therefore different systematics than the older electron scattering experiments. Instead, an electromagnetic calorimeter is used, which allows the simultaneous measurement of the elastic *e*-*p* scattering and the Møller *e*-*e* scattering, an exactly calculable QED process used for luminosity normalization. A windowless target, realized by a cryo-cooled hydrogen gas jet was another improvement. Furthermore, the PRad experiment measured at very low momentum transfer Q^2, dominated by the electric form factor G_E, and the data is therefore useful to constrain the extrapolation towards the slope at $Q^2 = 0$. While the PRad result is the first modern electron scattering experiment in agreement with the muonic hydrogen data, its accuracy is not sufficient to statistically reject the Mainz Microtron (MAMI) result from 2010. In fact, the behavior in the region of larger Q^2 obtained at MAMI is not at all compatible with the fit parameters obtained in the low-Q^2 from the PRad experiment. For a compact review of the proton charge radius including an outlook to upcoming experiments see, *e.g.*, the article by Karr et al. (2020) and citations therein.

It should also be noted that the analysis of the scattering results using dispersion relations, which relate the real and imaginary parts of the electromagnetic nucleon form factors, has delivered a small radius for the proton already in Belushkin et al. (2007) and still does so in the latest analysis based on all space-like and time-like data from elastic scattering and proton-antiproton annihilations presented by Lin et al. (2021). In summary, evidence for a smaller charge radius of the proton is growing and an adopted value for the proton radius of $r_p = 0.8414(19)\,\mathrm{fm}$, including the results from μp and μd measurements, has been made available online at NIST (2022) by the CODATA group.

The proton charge radius is also particularly important for comparisons of experimental nuclear charge radii of heavier elements with theoretical results. Many theoretical approaches, especially *ab-initio* calculations, are based on the treatment of the protons as point-like charges. The so-called point-proton radii $\langle r_{\mathrm{pp}}^2 \rangle$ obtained in theory must then be converted into the observable charge radii using the relation given by Friar et al. (1997)

$$\left\langle r_{\mathrm{c}}^2 \right\rangle = \langle r_{\mathrm{pp}}^2 \rangle + \left(\langle r_{\mathrm{p}}^2 \rangle + \frac{3\hbar^2}{4m_{\mathrm{p}}^2 c^2} \right) + \frac{N}{Z} \langle r_{\mathrm{n}}^2 \rangle + \langle r^2 \rangle_{\mathrm{so}} + \langle r^2 \rangle_{\mathrm{mec}} \,, \tag{42}$$

where $\langle r_{\mathrm{n}}^2 \rangle = -0.1161(22)\,\mathrm{fm}^2$ (Zyla et al., 2020) is the mean-square charge radius of the neutron, $\langle r^2 \rangle_{\mathrm{so}}$ denotes a spin-orbit contribution to the charge density and $\langle r^2 \rangle_{\mathrm{mec}}$ a similar contribution caused by meson-exchange currents. The second term in parenthesis is the relativistic Darwin-Foldy term and accounts for the "Zitterbewegung" of the proton due to virtual particle-antiparticle pairs that surround the 'bare' proton. Even a hypothetical point proton would thus acquire a mean-square charge radius of $3\hbar^2/\left(2m_{\mathrm{p}}c\right)^2 = 0.033\,\mathrm{fm}^2$ (m_{p} is the proton mass).

With the results from muonic atoms and laser spectroscopy on hydrogen becoming compatible, the issues in the comparison with electron-proton scattering must be addressed more closely and there are several upcoming experiments that will, for example, directly compare electron and muon scattering on protons (lepton universality) or investigate even lower energy transfers by looking at the recoiling proton. The problems arising in the determination of the proton charge radius based on elastic electron scattering have also been discussed from a fundamental point of view, *e.g.* by Jaffe (2021) and Miller (2019), with the result that – independent from the question of the interpretation of the form factor as the Fourier transform of a three-dimensional charge distribution – the proton radius can be defined as $r_{\rm p}^2 = -6G_E'(0)$ on equal footing in electron scattering, hydrogen and muonic-hydrogen. We finally note that elastic electron scattering also provides access to the magnetic structure of the nucleon as indicated by the appearance of G_M^2 in the cross section of Eq. (17). This allows the extraction of the ratio of the magnetic and electric form factors with high precision, in particular in combination with polarized electron beams, and demonstrates that charge and magnetization densities inside the proton differ. For a much deeper and comprehensive discusson of the proton charge radius, past and upcoming experiments, we refer to the latest review by Gao and Vanderhaeghen (2022).

The determination of absolute charge radii of short-lived isotopes with laser spectroscopy – as will be discussed in the following sections – is, according to our previous discussion, inevitably based on muonic atom X-ray spectroscopy and electron scattering data. Is there a possibility that more "radius puzzles" remain undiscovered? This can be considered unlikely. The main problem with the analysis of the proton scattering data is the identification of the right functional behavior for $Q^2 \to 0$. For heavier nuclei, the form factor has pronounced structures (see Fig. 1) that restrict the possible range of radii and provide much better constraints for the fits. For helium, this has already been confirmed by laser spectroscopy on muonic ^{4}He carried out by Krauth et al. (2021), which provided a charge radius in excellent agreement with the result from elastic electron scattering and, thus, with lepton universality.

Light Atoms and Halo Nuclei

Charge radii of the lightest elements have served as cornerstones for *ab-initio* calculations of nuclear properties, with the Greens-Function Monte-Carlo model and the No-Core Shell model at the forefront. The small number of nucleons make such calculations feasible. A second motivation for the study of the lightest elements is the existence of one of the most intriguing features of nuclear structure within their isotopic chains: halos of nuclear matter. A halo nucleus consists of a nuclear core with the standard (saturated) nuclear matter density, which is surrounded by a region of low-density nuclear matter that extends to very large radii. The combination of a large interaction cross section with narrow momentum distributions of the fragments and small binding energies of the valence nucleon(s) are a fingerprint of these systems.

The small contribution of the nuclear volume effect to the total isotope shift in light elements (see left panel in Fig. 5) requires a combination of highly accurate state-of-the-art experimental measurements and precise atomic mass-shift calculations. This can be illustrated by the fact that the isotope shift between ^{8}He and ^{4}He in the investigated transition is about 64 702 MHz, with only a 10^{-5} fraction, 0.8 MHz, originating from the field shift. To extract this small amount, the mass shift had to be calculated with an accuracy of order 10 kHz. Such calculations became feasible for helium in the 1990's (Drake, 1993), and have since been extended to lithium-like (Yan and Drake, 2000), beryllium-like (Puchalski et al., 2014), and boron-like systems in Maaß et al. (2019). The standard approach in these *ab initio* calculations is non-relativistic QED, with the Schrödinger equation first solved using a set of strongly correlated basis functions. The obtained eigenfunctions form the basis to include relativistic and QED contributions using perturbation theory. Especially for the halo systems, the nuclear polarizability has to be taken into account as was demonstrated by Puchalski et al. (2006). Experimentally, the required isotope-shift accuracy is not available with the standard techniques discussed so far and therefore each of the light elements was investigated using a tailored approach. Here, we provide a brief updated summary; for a more extensive presentation we refer to the colloquial review by Lu et al. (2013).

Helium – The ^{4}He charge radius has been determined with highest precision from laser spectroscopy of the $2s \rightarrow 2p$ transitions in muonic ^{4}He by Krauth et al. (2021) to $r_\alpha = 1.678\,24(83)\,\mathrm{fm}$. Contrary to the proton, the result from the world data of elastic electron scattering of $r_\alpha = 1.681(4)\,\mathrm{fm}$ obtained by Sick (2008) is in good agreement with this value. The charge radii of the neutron halo nuclei ^{6,8}He were determined based on isotope-shift measurements in a magneto-optical trap (MOT). The short-lived isotopes were produced in nuclear reactions online at the Argonne National Laboratory (^{6}He) (Wang et al., 2004) and at GANIL (^{6,8}He) (Müller et al., 2007), transferred into a low-pressure gas discharge cell to excite population to the metastable $1s2s\,^3\mathrm{S}_1$ state, decelerated in a Zeeman slower, and finally captured in the MOT. The MOT was operated on the infrared $1s2s\,^3\mathrm{S}_1 \rightarrow 1s2p\,^3\mathrm{P}_2$ transition. Once a single atom was captured and cooled, laser spectroscopy was performed on the $1s2s\,^3\mathrm{S}_1 \rightarrow 1s3p\,^3\mathrm{P}_{0,1,2}$ transitions at 389 nm.

It should be noted that the presence of the infrared cooling laser is detrimental due to AC-Stark shifts (Cohen-Tannoudji et al., 1998) of the atomic levels and that a single photon recoil of the UV transition accelerates a helium atom from rest to a velocity that causes a Doppler shift of about 500 kHz, far greater than the required accuracy. Hence, the cooling laser was turned off during spectroscopy (2 μs) to avoid systematic shifts, but periodic re-trapping and cooling was performed (8 μs) by switching between a spectroscopy and a trapping mode with 100 kHz repetition rate to remove the recoil energy. An accuracy of better than 100 kHz was reached for ^{8}He (half-life 119 ms) with capturing rates of 30 atoms $1/\mathrm{h}$ and 200 ms observation time per atom, impressively demonstrating the performance of the technique.

Charge radii of the helium isotopes are shown in Fig. 13, based on the results of the isotope shift measurements and the charge radius obtained in muonic atom spectroscopy

$$R_c(^A\mathrm{He}) = \sqrt{r_\alpha^2 + \delta\langle r_\mathrm{c}^2\rangle^{4,A}}. \tag{43}$$

The large increase of the nuclear charge radius from ^{4}He to ^{6}He is clearly visible. It is dominated by the recoil effect of the two halo neutrons on the α-particle, whereas a swelling of the α-core is expected to contribute less than 2% of the total change.

The charge radius of ^{8}He is smaller than that of ^{6}He. This has been explained with the support of theoretical calculations investigating the effect of the additional neutron correlations in ^{8}He. These calculations demonstrate the different density dependence between a dineutron configuration and a cigar-like configuration. The former has a large radial extent and small opening angle between the two neutrons, while the latter is located closer to the core with the neutrons having larger opening angles. The cigar-like contribution thus has a smaller recoil effect on the α-core. Since the amplitude of the dineutron contribution in the ground-state wavefunction gets weaker in ^{8}He while the cigar-like component increases, the center-of-mass motion of the α-core is reduced compared to ^{6}He (Papadimitriou et al., 2011) and the charge radius is reduced. This is illustrated in the right panel in Fig. 13.

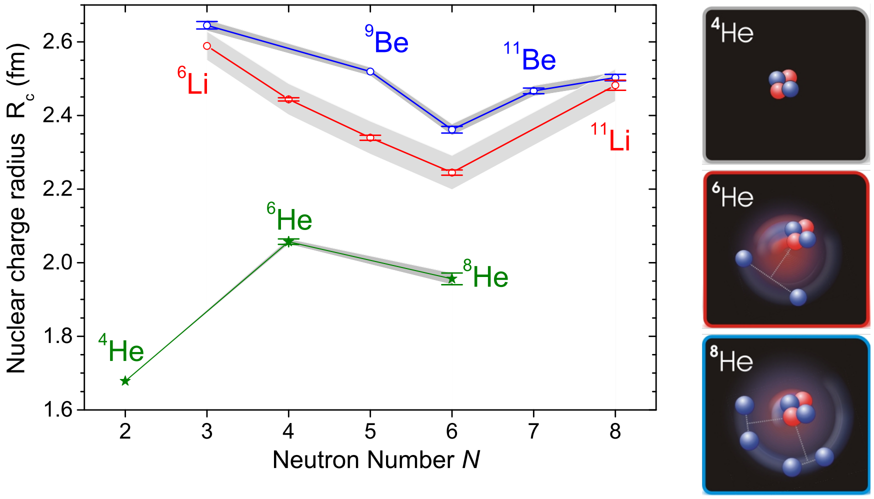

Fig. 13 *Left panel*: Charge radii of helium (Z=2), lithium (Z=3), and beryllium (Z=4) isotopes. Labels are attached to the stable reference isotopes and halo isotopes. The error bars represent the uncertainties that are conveyed from the isotope-shift measurements, whereas the grey-shaded areas represent the total uncertainty including the uncertainty of the reference radius. *Right panel*: Illustration of the nuclear structure of ^{4}He, ^{6}He, and ^{8}He. Red spheres represent protons, and blue spheres represent neutrons. The nuclear charge radius is predominantly a measure of the center-of-mass motion of the charge carrying α-like core in ^{6}He and ^{8}He and depends on the correlation of the halo neutrons. (Figure courtesy of Peter Müller, Argonne National Laboratory).

Lithium – For lithium isotopes, the data from elastic electron scattering is rather old and much more scarce than for hydrogen and helium. Analysis of the world data revealed that the previously reported uncertainty for the charge radius of ^{7}Li is underestimated and that ^{6}Li is a better reference for the nuclear size since the region of inelastic scattering is better separated from the elastic peak. As a reference for the laser spectroscopic measurements of the unstable isotopes, a value of $R_c(^6\mathrm{Li}) = 2.589(39)\,\mathrm{fm}$ was obtained in Nörtershäuser et al. (2011b). Stable and short-lived lithium isotopes were studied at GSI by Ewald et al. (2004) and at TRIUMF by Sánchez et al. (2006) by stopping beams of a few 10 keV energy in a thin graphite foil heated with a CO_2 laser to 2000 °C to ensure fast release of neutralized thermal atoms. These atoms were then probed in the $2s\,^2S_{1/2} \rightarrow 3s\,^2S_{1/2}$ transition by two-photon spectroscopy. Two-photon absorption in a pair of counter-propagating laser beams is Doppler free to first order and has the advantage that all atoms are in resonance independent of their thermal velocity, once the laser is tuned to the resonance frequency $\nu_0 = (E_\mathrm{f} - E_\mathrm{i})/2h$, where E_i and E_f are the energies of the initial and final state, respectively. Successful laser excitation was detected by resonance ionization with cw lasers after the spontaneous decay to the $2p\,^2P_J$ states along the $2p\,^2P_J \rightarrow 3d\,^2D_{J'} \rightarrow \mathrm{Li}^+ + \mathrm{e}^-$ ionization path and subsequent filtering of the created ions in a quadrupole mass spectrometer as detailed in Nörtershäuser et al. (2011a).

The trend of the nuclear charge radii is included in Fig. 13. Error bars of the individual data points represent the uncertainty of the charge radius originating from the isotope-shift measurements, whereas the grey band represents the total uncertainty including that of the ^{6}Li reference radius. For all isotopes, even for ^{11}Li, the contribution of the reference radius to the total uncertainty is significant.

The lowest mass isotope ^{6}Li has, surprisingly, the largest charge radius of all lithium isotopes. This is related to the cluster structure of these nuclei. The strong binding of the α particle, favors a “decomposition” of the ^{6}Li wavefunction into α+d. The deuteron itself already has a large charge radius compared to a proton and the clusterization leads to a center-of-mass motion that additionally smears out the charge distribution of the α as well as of the deuteron. The ^{7}Li wavefunction is dominated by an α+t structure (t = triton = ^{3}H nucleus) with a reduced size and recoil motion. In ^{8,9}Li, the additional neutrons lead to a structure that is much closer to the mean-field picture, which is also reflected in a lower threshold for neutron removal than for cluster separation in these isotopes. Consequently, the charge radius shrinks further and the minimum is reached for ^{9}Li. The strong rise towards ^{11}Li indicates a strong correlation of the two halo neutrons in the form of a dineutron, similar to the case of ^{6}He. Some cluster models required a large contribution of nuclear polarization to obtain the increased charge radius, while others attribute it to the recoil effect on the nuclear core. However, models with a large fraction of core polarization typically result in magnetic dipole and electric quadrupole moments that are quite different between ^{9}Li and ^{11}Li, contrary to the experimental results for these observables as summarized in Neugart et al. (2008). The accuracy of the available nuclear-structure data and the remaining model dependence unfortunately do not allow for an unambiguous separation of core excitation and recoil effect. However, a three-body model with adjusted parameters could actually construct a ^{11}Li wavefunction that reproduces consistently all known experimental observables within the experimental accuracy as has been reported by Shulgina et al. (2009).

Beryllium – A rather precise value of $R_\mathrm{c}(^9\mathrm{Be}) = 2.519(12)$ fm has been reported for the only stable beryllium isotope ^{9}Be by Jansen et al. (1972) from electron scattering, which is the basis for the uncertainty band of Be isotopes in Fig. 13. It was, however, determined in a model-dependent way and is likely to have underestimated uncertainties.

To study short-lived beryllium isotopes, the technique of collinear laser spectroscopy was adapted in a special form. Spectra were taken with the laser beam copropagating and counterpropagating quasi-simultaneously by quickly alternating between the two geometries (Krieger et al., 2017). The setup and a spectrum of the one-neutron halo isotope ^{11}Be are depicted in Fig. 14. We provide some details of the experimental setup in the figure caption since this technique is capable of being extended to the light elements for which short-lived isotopes have not been studied by laser spectroscopy so far, *i.e.*, boron to fluorine (Z = 5–9).

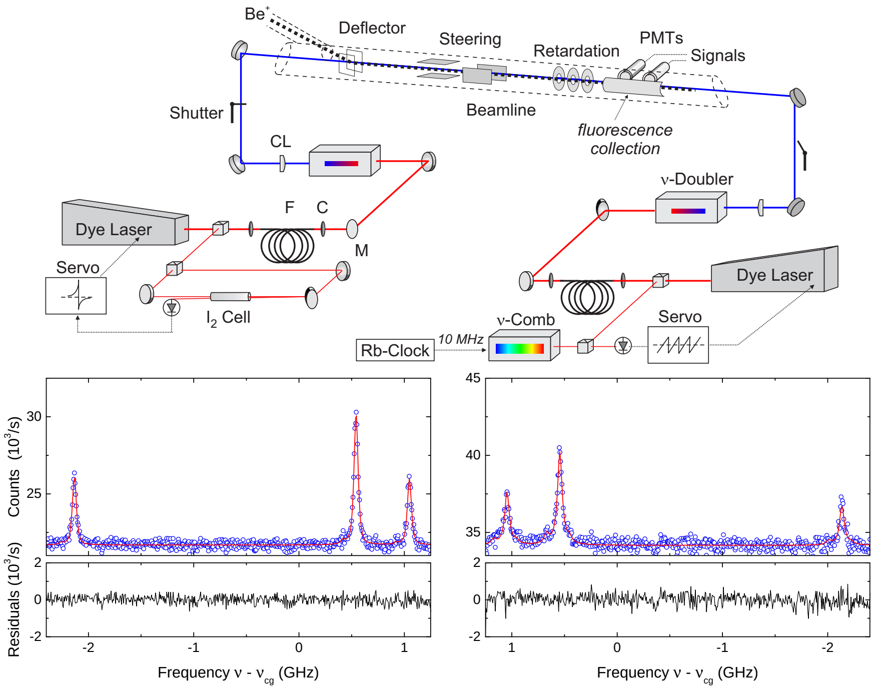

Fig. 14 *Top panel*: Experimental setup for the beryllium measurements at ISOLDE. Two dye laser systems were used to excite the $2s\ ^2S_{1/2} \rightarrow 2p\ ^2P_{1/2,3/2}$ transitions in Be^+. The laser for collinear excitation (left) was operated at a fundamental wavelength of 624 nm and stabilized to a hyperfine transition of molecular iodine. The output beam was transported by a fiber into the experimental hall, frequency doubled to 312 nm and guided into the beam line. The other laser (right) was locked to a frequency comb. After frequency-doubling to 314 nm, the UV laser beam was anticollinearly superposed with the ion beam. Mechanical shutters were operated to quickly switch between collinear and anticollinear excitation. *Bottom panel*: Spectra of ^{11}Be in collinear and anticollinear geometry. Since the two spectra are "mirror images" (w.r.t. the scanned voltage, converted here into frequency space), many systematic uncertainties cancel when calculating the rest-frame frequency of the transition as the geometrical average of the two observed resonance frequencies. (Reprinted with permission by Springer Nature from Krieger et al. (2017).)

By applying a frequency comb, a device that has revolutionized measurements of laser frequencies, the uncertainty of the ions' velocity caused by inaccurately known starting potentials, was eliminated. With the measured Doppler-shifted resonance frequencies ν_c and ν_a in collinear and anticollinear geometry, respectively, the rest-frame frequency ν_0 can be obtained as their geometrical average and the dependence on β and γ cancels completely

$$\nu_a \cdot \nu_c = \nu_0 \gamma(1+\beta) \times \nu_0 \gamma(1-\beta) = \nu_0^2 \,. \tag{44}$$

This technique has been applied online at ISOLDE/CERN to measure the charge radii of $^{7,9-11}$Be by Nörtershäuser et al. (2009) and extended to ^{12}Be, where the photon-ion coincidence detection method was applied by Krieger et al. (2012). The charge radius trend along the beryllium chain is quite similar to the lithium chain as is visible in Fig. 13. The cluster structure of the isotopes ($^7\mathrm{Be} = \alpha + {}^3\mathrm{He}$, $^{8+N}\mathrm{Be} = \alpha + \alpha + N\mathrm{n}$, for $N > 0$, note that ^{8}Be is unbound) leads again to a reduction of the charge radius with increasing neutron number up to ^{10}Be. The sudden increase of the charge radius of ^{11}Be is directly connected to the recoil effect. Since ^{11}Be is a one-neutron halo, the discussion is easier than for the two-neutron halos discussed so far, since correlation between halo nucleons is absent. Again, there might be a contribution of core-polarization but this is expected to be weak. If one assigns the full effect to the recoil motion, the charge radius of ^{11}Be can be written as composed of the charge radius of the ^{10}Be core, its center-of-mass motion, and the contribution of the neutron radius

$$R_c^2\left({}^{11}\mathrm{Be}\right) = R_c^2(\text{ core }) + \frac{1}{11^2} R_{\text{core }-n}^2 + \frac{1}{4} R_n^2. \tag{45}$$

Under these assumptions, the average distance between the halo neutron and the ^{10}Be core, $R_{\text{core }-n}$, turns out to be about 8 fm, surprisingly large compared to the interaction length of the strong force of about 1 fm.

While the very low binding energy of only $S_n = 500\,\mathrm{keV}$ favors an *s*-wave halo in ^{11}Be, the wavefunction of ^{12}Be ($S_{2n} \approx 3.67\,\mathrm{MeV}$) is assumed to be of strongly mixed p^2 and $(sd)^2$ character, indicating a breakdown of the $N = 8$ magic number as reported first from one-neutron knockout reaction experiments by Navin et al. (2000). The ^{12}Be charge radius is quite sensitive to the mixture of the two states and has therefore been used to rescale the strength of the spin-orbit force in fermionic molecular dynamics calculations, which simulates the role of three-body forces not explicitly included in the theory as discussed in Krieger et al. (2012). This mixture leads to an increased probability density of the neutrons to be located outside the ^{10}Be core, pulling the α particles of the core apart due to the attractive n–α interaction. Theory needs an $(sd)^2$ admixture of about 70% in ^{12}Be to reproduce the observed charge radius, being a clear indication for the disappearance of the classical $N = 8$ shell closure.

Boron – There is little information on the charge radii of boron isotopes so far. Measurements of the stable isotopes ^{10,11}B were performed using resonance ionization spectroscopy with cw lasers on a thermal atomic beam by Maaß et al. (2019) provided $\delta\left\langle r_c^2\right\rangle^{10,11} = -0.49(12)\,\mathrm{fm}^2$, however an accurate reference radius from electron scattering or muonic atom spectroscopy is missing. This chain is notably interesting because ^{8}B is believed to be the prototype of a proton halo. A measurement of this nucleus is in preparation at Argonne National Laboratory (Maaß et al., 2017), with the collinear-anticollinear technique to be applied after charge exchange of the B$^+$ ions into the ground state of the boron atom. Of particular interest would be the difference in charge radius between ^{7}Be and ^{8}B since it would directly probe the effect of the halo proton. This would require a reliable reference radius in both isotopic chains, which is not yet available.

Currently, ongoing theoretical efforts by Patkóš et al. (2021) and experimental preparations by König et al. (2020) target the all-optical extraction of nuclear charge radii from helium-like systems. The general idea is similar to the treatment in hydrogen-like systems: high-precision calculations of specific transition energies in helium-like systems carried out under the assumption of a point-like nucleus will be compared with measured transition energies. The difference is related to the finite nuclear-size effect and is used to extract the nuclear charge radius. High-precision measurements on Be^{2+} and B^{3+} ions will then allow for a determination of the charge radii in both isotopic chains on an equal footing. First measurements on ^{12}C^{4+} ions are ongoing to validate the technique, since the charge radius of ^{12}C is very well known from electron scattering.

Kinks at Shell Closures and Odd-Even Staggering

In a macroscopic model the addition of neutrons to a nucleus leads to a continuous increase of nuclear volume. This should give rise to an increase of its radius according to $\sqrt[3]{A}$ since the interior of the nucleus is expected to have a constant density due to the saturation of the nuclear force. In reality, the fine structure of charge radii along an isotopic chain exhibits a diversity of effects that can be associated with a variety of microscopic phenomena related to proton-neutron interactions. As an example, the charge radii of calcium isotopes are depicted (in bold blue) among others in Fig. 15a. Striking features include the parabolic behavior between ^{40}Ca and ^{48}Ca superimposed with a pronounced odd-even staggering (oes) as a function of neutron number, the identical ms charge radii of the two isotopes enclosing this region, differing in the number of nucleons by 20%, and the sharp kink at ^{48}Ca with a rapid increase in size towards ^{52}Ca. In order to describe the parabolic behavior of the calcium isotopes, Zamick (Zamick, 1971) and Talmi (Talmi, 1984) provided a model that is based on core polarization caused by the increasing number of neutrons. It describes the trend in $\delta\left\langle r_c^2\right\rangle$when filling a shell by four parameters that are connected to a linear increase of the radius, superimposed by a quadratic form proportional to the number of particle-holes multiplied by the number of particles in the respective neutron shell, representing the increasing deformation towards midshell, and an odd-even staggering. This four-parameter model is rooted in the generalized seniority picture for a semimagic isotope chain and is able to excellently reproduce the radii of the $^{40-48}$Ca isotopes as well as long chains of isotopes close to magic proton numbers, *e.g.* $^{100-130}$Cd.

Theoretical investigations during the last decades revealed that several nuclear structure effects contribute to this complex pattern. These include zero-point motion associated with surface vibrations (Reinhard and Drechsel, 1979; Barranco and Broglia, 1985), configuration mixing (Caurier et al., 2001) and nucleonic pairing (Reinhard and Nazarewicz, 2017), which carries much of the essence of the generalized seniority model into the mean-field picture of the nucleus. The electric and magnetic form factors of the nucleons play a role, as well as relativistic corrections (Friar and Negele, 1975) and the spin-orbit interaction. Charge radii on the proton-rich side are additionally affected by the presence of the particle continuum as discussed in Miller (2019).

In this section, we will concentrate on two features that are almost ubiquitous throughout the nuclear landscape: Kinks at neutron shell closures and odd-even staggering. Both can be quantified using a three-point difference formula, defined as

$$\Delta_{kn}^{(3)} R_{\mathrm{c}}(N) \equiv \frac{1}{2}\left[R_{\mathrm{c}}(N+k) - 2R_{\mathrm{c}}(N) + R_{\mathrm{c}}(N-k)\right]. \tag{46}$$

The oes is a particular and almost universal property of radii, which is expressed by a systematic difference of the radii of odd-N nuclei with respect to their even-N neighbours. It is characterized by the one-neutron (k=1) three-point difference $\Delta_{1n}^{(3)}$, whereas two-neutron (k=2) differences $\Delta_{2n}^{(3)}$ are better suited to quantify and compare the magnitude of the kink at a shell closure between several isotopic chains since it removes the interfering effect of the oes.

Kinks at the shell closures were first discussed in the cesium (Thibault et al., 1981a) and barium isotopes (Mueller et al., 1983), where deviations from a smooth rise were explained by changes in deformation. It turned out that these kinks are a universal feature as they are observed at all neutron shell closures corresponding to magic neutron numbers $N \geq 28$, as shown in Fig. 15 for the cases $N = 28, 82$, and 126, while the region around $N = 50$ is included in Fig. 17. It is striking that in these cases all isotopic chains exhibit a rather similar (Z-independent) slope above the magic number, whereas the curves diverge considerably for the isotopes below. At the smaller magic numbers $N = 2, 8, 20$, the radii do not show a similarly universal trend or data is too sparse. At $N = 20$, experimental information is only available for Ar, K, and Ca and none of these chains exhibit a notable kink, (Fig. 15). For isotopes of even smaller masses, effects of the cluster structure of nuclei are often more pronounced than possible shell effects. It should be noted that all magic numbers above $N = 20$ arise from the spin-orbit interaction. They originate from a strong energy reduction for the $L + 1/2$ spin-orbit partner of the largest angular momentum in the next higher harmonic oscillator shell, which intrudes then into the lower shell as a unique-parity orbital.

The kink at doubly magic isotopes is of special interest since these are best suited candidates for many theoretical approaches, including *ab initio* coupled cluster calculations. They are therefore stepping stones to extend *ab initio* models into the

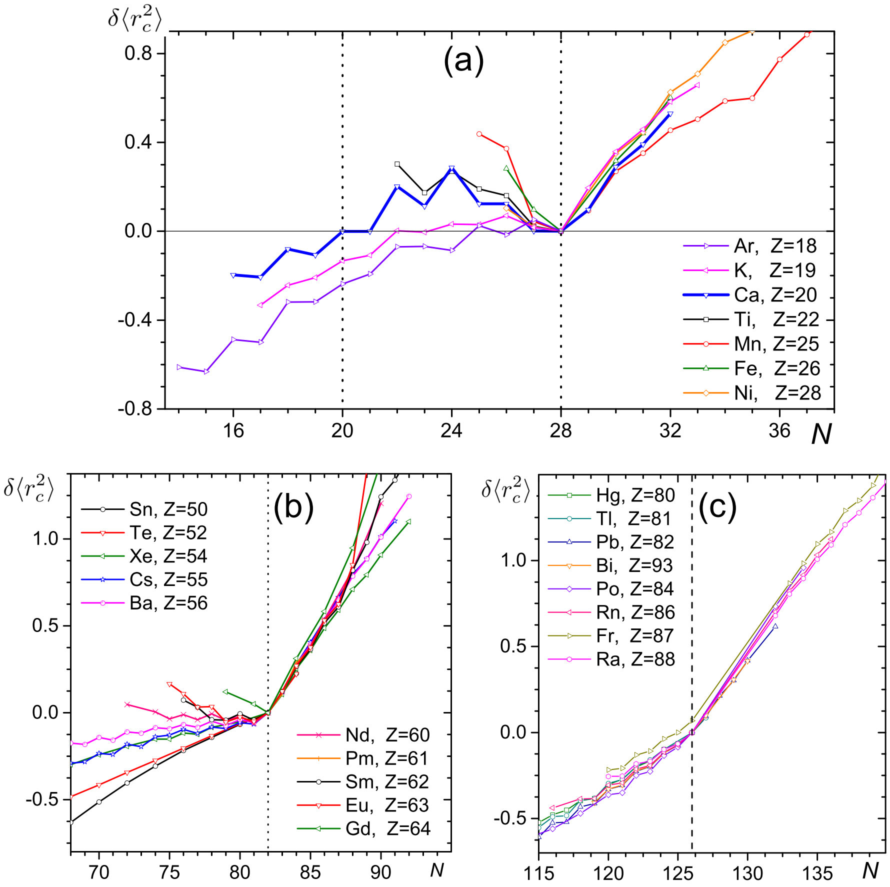

Fig. 15 The trend of charge radii at the neutron shell closures $N = 28$, 82, and 126, represented by the change in the ms charge radius $\delta\langle r_c^2\rangle$ as a function of neutron number.

heavier mass regions. From all doubly magic isotopes with (N, $Z \geq 20$), only ^{40}Ca ($Z = 20$, $N = 20$), ^{48}Ca ($Z = 20$, $N = 28$) and ^{208}Pb ($Z = 82$, $N = 126$) are stable. In particular, the kink at ^{208}Pb has been studied intensively using classical as well as relativistic nuclear density functional theory (DFT), which has initiated an ongoing debate as to whether it is mainly caused by pairing as argued in Gorges et al. (2019) or – according to Goddard et al. (2013) – rather by the attractive interaction between neutrons in the $1i_{13/2}$ orbital and all protons in orbitals with principal number $n = 1$. In the latter explanation, the increasing number of neutrons in the $1i_{13/2}$ shell above the $N = 126$ shell closure, leads to an effective "pull" of the inner protons due to the large spatial overlap of orbitals with the same n. Among the non-relativistic DFT models, the Fayans functional has been found to be particularly suitable for the description of the detailed trend of charge radii of many isotopic chains, including the kinks at $N = 28, 82$, and 126 (Reinhard and Nazarewicz, 2017; Gorges et al., 2019;

Kortelainen et al., 2022). A detailed discussion of the kinks in relativistic density functional theory is provided in Perera et al. (2021).

The $N = 28$ isotones are the only ones for which the kink has been observed in neutron-rich and proton-rich doubly magic nuclei. Here, it was found that the change in the ms charge radii across the shell closure is practically identical in ^{48}Ca and ^{56}Ni as presented by Sommer et al. (2022). This is a clear indication that the strength of the kink does not directly reflect the strength or "goodness" of the shell closure since ^{48}Ca is known to have a strong shell closure whereas ^{56}Ni is rather soft. This softness is revealed for example via the magnetic moment of ^{55}Ni which lies far from the single-particle Schmidt value (Neyens, 2023), and a B(E2) transition strength (???, 2023) that is much larger than for other doubly magic nuclei.

With the rapid progress in chiral effective field theory (χEFT) and corresponding many-body calculations, *ab initio* calculations of trends of charge radii in the medium-mass region between calcium and tin have become possible and were the focus of many recent studies, *e.g.*, (Hagen et al., 2016; Garcia Ruiz et al., 2017; de Groote et al., 2020; Koszorús et al., 2021; Malbrunot-Ettenauer et al., 2022).

We now turn briefly to the odd-even staggering. Although the oes is very small in comparison to the total radius, isotope-shift measurements are sensitive to the effect as it is directly reflected in the observable $\delta\left\langle r_{\mathrm{c}}^{2}\right\rangle^{A,A'}$. In "normal" oes, an isotope with an odd neutron number has a slightly smaller charge radius than expected from the average of the two neighboring even-N isotopes. An explanation for the oes is the reduction of pairing correlations caused by the Pauli-blocking effect due to the unpaired neutron in an odd-N isotope, which leads to a slightly smaller ms radius. At the shell closure, however, this "normal" behavior is locally inverted due to the kink, *i.e.*, the magic isotope is smaller than the (average of) neighboring odd-N isotopes. We note that an inversion of oes is not restricted to shell closures and has, for example, been observed in the radium isotopes, where it has been interpreted as a sign for octupole deformation in Ahmad et al. (1988). This and the effect of deformation on charge radii will be discussed in more detail in the following sections.

As an example for a smooth behavior of radii between two shell closures, the Cd radii are shown in the left panel of Fig. 16. The black points represent the experimental radii with systematic uncertainties represented by the grey band, and the red line is an adaption of the Zamick-Talmi model to the radii. The linear increase is represented by the green dotted line, with the data reflecting a dominant quadrupole (parabolic) contribution. The oes is clearly visible, even though far weaker than in the calcium chain. While the Zamick-Talmi model is able to reproduce such data quite well, it lacks a detailed microscopic picture and cannot transit across a shell closure as it provides no means to produce a kink as is expected beyond ^{130}Cd. The right panel shows the one-neutron three-point difference along the chain. A regular pattern without any inversion of the oes is visible.

The nature of the oes staggering has recently been explored in the Cu chain from the $N = 28$ up to the $N = 50$ shell closure, in close proximity to the doubly magic ^{56,78}Ni nuclei (de Groote et al., 2020). The behavior of the oes was found to be quite distinct at both ends of the isotopic chain. In this region, it was also possi-

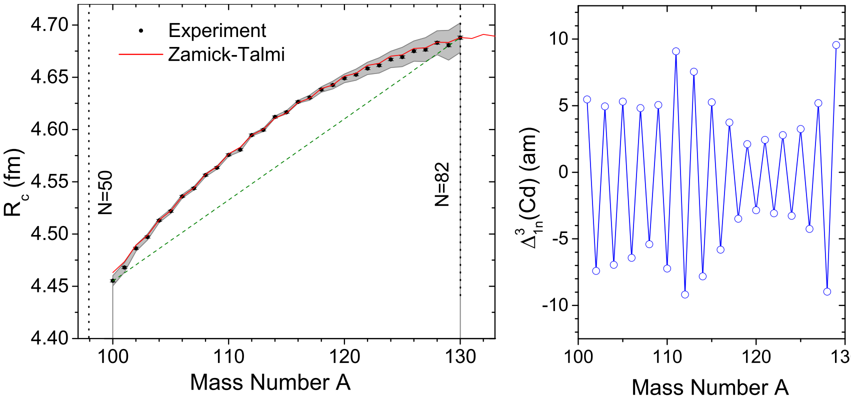

Fig. 16 *Left panel*: Radii of $^{100-130}$Cd isotopes filling the $sdg_{7/2}h_{11/2}$ shell. A fit of the Zamick-Talmi model is shown in red with its linear part in green. *Right panel*: The one-neutron three-point difference of the radii shown in the left panel in attometer as a function of mass number.

ble to carry out *ab initio* valence-space in-medium similarity renormalization group (VS-IMSRG) calculations. Both theoretical approaches, DFT and VS-IMSRG, satisfactorily reproduced the observed behavior. That this many-body effect emerged in calculations with interactions that are constrained solely by four-body data, *i.e.*, information on nuclei up to ^{4}He, is promising for a better understanding of the microscopic underlying principles and represents an important step towards a predictive nuclear theory.

Between Shell Closures: Charge Radii and Deformation

One of the most important connections between optical spectroscopy of radioactive isotopes and the wider field of nuclear spectroscopy arises through the interpretation of the measured mean-square charge radius and the nuclear deformation. The expansion of an axially deformed charge distribution in terms of spherical harmonics results in the following expression:

$$\left\langle r_{\mathrm{c}}^2\right\rangle = \left\langle r_{\mathrm{c}}^2\right\rangle_{\mathrm{sph}} \left(1 + \frac{5}{4\pi}\sum_{i=2}^{\infty}\left\langle \beta_i^2\right\rangle\right) + 3\sigma^2, \tag{47}$$

where $\left\langle r_{\mathrm{c}}^2\right\rangle_{\mathrm{sph}}$ is the ms charge radius of an equivalent, sharp-surfaced, spherical distribution of equal volume, and β_i represents the contribution from quadrupole (i = 2), octupole (i = 3) and so on, deformations. The summation is dominated by the quadrupole term. A constant diffuseness term is added to account for the convolution of a uniform "sharp cut-off" distribution with a Gaussian distribution, independent of A, Z, N and β_i. This term vanishes for differences in mean-square charge radii, extracted from optical isotope shifts between masses A and A', given to second order:

$$\delta\left\langle r_{\mathrm{c}}^{2}\right\rangle^{A,A'} = \delta\left\langle r_{\mathrm{c}}^{2}\right\rangle_{\mathrm{sph}}^{A,A'} + \left\langle r_{\mathrm{c}}^{2}\right\rangle_{\mathrm{sph}} \cdot \frac{5}{4\pi}\delta\left\langle \beta_{2}^{2}\right\rangle^{A,A'} . \tag{48}$$

This relationship affords measures of changes in *mean-square* quadrupole deformation, $\left\langle \beta_2^2 \right\rangle$, which may be compared with the square of the static quadrupole deformation, $\langle \beta_2 \rangle$. For axially symmetric deformed nuclei, the static deformation is extracted from the spectroscopic quadrupole moment, Q_{s}, measured by laser spectroscopy. The latter is related to the intrinsic quadrupole moment, Q_0, via the strong-coupling limit

$$Q_0 = Q_{\mathrm{s}} \frac{(I+1)(2I+3)}{3\Omega^2 - I(I+1)}, \tag{49}$$

where Ω is the projection of the nuclear spin along the intrinsic symmetry axis. The static deformation parameter, $\langle \beta_2 \rangle$, can then be calculated from Q_0 using:

$$Q_0 \approx \frac{5Z\left\langle r_{\mathrm{c}}^{2}\right\rangle_{\mathrm{sph}}}{\sqrt{5\pi}} \langle \beta_2 \rangle \left(1 + 0.36\langle \beta_2 \rangle\right). \tag{50}$$

We see that through a simple liquid droplet model approach, deformation parameters can be compared as a means of understanding the collective nature of nuclear deformation. Discrepancies between the extracted mean-square deformation, $\left\langle \beta_2^2 \right\rangle$, with the square of the static deformation parameter, $\langle \beta_2 \rangle$, can be attributed to a dynamic component, β_{dyn}^2,

$$\beta_{\mathrm{rms}}^2 = \langle \beta_2 \rangle^2 + \left(\left\langle \beta_2^2 \right\rangle - \langle \beta_2 \rangle^2\right) = \beta_{\mathrm{static}}^2 + \beta_{\mathrm{dyn}}^2. \tag{51}$$

The dynamic contribution produces a mean-square charge radius larger than what would be expected from the static deformation alone. In the absence of octupole or triaxial deformation, any discrepancy indicates a "beta-softening" of the (axial) deformation. We note that the mean-square charge radii, expressed in terms of an axially deformed charge distribution (Eq. (47)), can be used to infer the deformation of all nuclei, while the static quadrupole contribution is restricted to cases with a nuclear spin $I > 1/2$.

In some cases, the picture of a nucleus in which only axial symmetric deformation is considered may be too simple. For example, nuclei around Z = 72–78 (hafnium to platinum) are known to be transitional, exhibiting a variety of nuclear shapes depending on the neutron and proton numbers (Casten, 1985). Theoretical energy density functional calculations indicate changes from axially-symmetric prolate deformation near stability, through a γ-soft region of triaxiality, towards oblate shapes around N = 120 (Robledo et al., 2009). Experimental information in the region has primarily come from γ-ray spectroscopy and β-decay studies, often at fragmentation facilities due to the refractory nature of these elements. At the KISS facility, RIKEN, the laser ion-guide based separator combined with multi-nucleon transfer reactions and in-gas-cell resonance ionization spectroscopy, is being used to explore this challenging region.

As an example, in-gas-cell RIS has been performed on ^{194,195}Os, with the nuclei detected using beta-decay spectroscopy and time-of-flight mass spectrometry by Choi et al. (2020). From the evaluated isotope shifts, the corresponding variations in mean-square charge radii were determined and, under the assumption of axial deformation, the quadrupole deformation parameter was extracted. The data, when combined with existing measurements, indicate an increase in the mean-square charge radii as the $N = 126$ shell is approached, with a corresponding reduction in $\langle \beta_2^2 \rangle^{1/2}$. A sudden deviation from the linear trends at $A = 194$ is indicative of a shape transition from a prolate shape to a less-deformed oblate configuration. Clarification of this feature could be probed in the future via higher-precision measurements using in-gas-jet RIS.

We note that sensitivity to the triaxial degree of freedom can potentially be explored via the mean-square charge radius, as illustrated by Hilberath et al. (1992), in the expansion of Eq. (47),

$$\langle r_\mathrm{c}^2 \rangle = \langle r_\mathrm{c}^2 \rangle_\mathrm{sph} + \frac{5}{4\pi} \langle r_\mathrm{c}^2 \rangle_\mathrm{sph} \cdot \left(\langle \beta_2^2 \rangle + \frac{3}{10} \langle \beta_2^3 \rangle \cos\gamma (1 - 4\sin^2\gamma) \right), \tag{52}$$

where γ is the asymmetry parameter. However, for an axial deformation $\beta_2 = 0.2$, the triaxial addition to the charge radius is expected to contribute at a level of only 6%. Therefore, this degree of freedom is usually neglected in the analysis of optical isotope shifts.

Although the summation term in Eq. (47) is dominated by the quadrupole deformation, one of the open questions in the field of precision laser spectroscopy for nuclear structure physics is whether the charge radius can be used as an indicator for octupole deformation, in other words, nuclei that exhibit pear-shaped intrinsic configurations in the nuclear ground state. Octupole collectivity is caused by strong correlations between nucleons near the Fermi surface, occupying single-particle states of opposite parity that differ by three units of orbital and total angular momentum. The collective behavior results in a large enhancement of symmetry-violating nuclear properties, such as the Schiff moment (Engel et al., 2003). A measurement of this property would help to constrain unknown sources of CP violation, proposed as necessary ingredients in our observed matter-antimatter asymmetry in the universe. Experimental and theoretical efforts to identify and study nuclei with stable ground-state octupole deformation is therefore of significant interest in several fields of physics.

Neutron-deficient actinide nuclei have traditionally been highlighted for octupole deformation studies, with maximum values of deformation predicted around $N = 136$. Direct experimental evidence of stable octupole deformation has been reported only for a few isotopes, for example ^{222,224,226}Ra ($Z = 88$) (Gaffney et al., 2013; Butler et al., 2020). A recent global analysis of ground-state octupole deformation has been performed using nuclear density functional theory with several nonrelativistic and covariant energy density functionals by Cao et al. (2020). In addition to the "usual suspects", several promising candidates are highlighted in neutron-deficient isotopes of uranium, plutonium and curium.

Measurements of relative changes in the nuclear charge radii have been suggested as indicative of the emergence of octupole deformation in nuclei. For example, the odd-N neutron-rich isotopes of radon, francium and radium, all studied by collinear laser spectroscopy, exhibit larger charge radii than the average of their even-N neighbors. This effect is an inversion of the "normal" odd-even staggering seen elsewhere in the nuclear chart and discussed in the previous section. The underlying mechanism is proposed to be the same as the one that leads to the systematic splitting of parity doublets in reflection asymmetric nuclei. Recent in-source RIS experiments on neutron-rich actinium isotopes $^{225-229}$Ac at the ISAC facility, TRIUMF, by Verstraelen et al. (2019) provided additional charge radii data for comparison with different nuclear energy density functionals. For calculations using SLy5s1, the best agreement with the experimental data was obtained when the octupole degree of freedom was taken into account. However, experimental uncertainties due to the lower resolution of the technique lead to caution in the interpretation of these results, motivating the use of high-resolution methods in the future. This is the goal for proposed measurements at ISOLDE using the PI-LIST technique.

Interpretations of mean-square charge radii measurements are often discussed in parallel with other nuclear observables, for example transition probabilities from the nuclear ground state to the first excited 2^+ state, B(E2) in even-even nuclei, that shows strong correlations with the nuclear deformation expressed in mean-square form. Trends in nucleon separation energies, for example two-neutron separation energies, S_{2n}, extracted from precision mass measurements, are nowadays commonly used in interpreting new data. Comparisons of behaviour between mean-square charge radii and a range of nuclear observables have been presented by Angeli and Marinova (2015) as well as by Cakirli et al. (2010), with the former additionally evaluating isotonic trends.

Deformation at $N \sim 60$

To illustrate the sensitivity of ms charge radii to changes in nuclear shape, we focus our attention on the mass $A{\sim}100$ region, in which a sudden onset of deformation has been long-established at $N{\sim}60$. In this region, an increase of size on the addition of a neutron may be estimated to be $\sim 0.07\,\mathrm{fm}^2$. If the same neutron would affect the structure such that the shape changes from $\langle \beta_2^2 \rangle = 0$ to $\langle \beta_2^2 \rangle = 0.1$, an order of magnitude increase in the differential change would be expected. Figure 17 highlights the charge radii variations for the elements of krypton ($Z = 36$) to molybdenum ($Z = 42$), with three general regions of note corresponding to neutron numbers $N \leq 50$, $50 \leq N \leq 60$ and $N \geq 60$. We have already addressed radii variations at shell closures in connection with the $N = 28$, 82 and 126 magic neutron numbers. In Fig. 17 we see the clear effect of the $N = 50$ shell, having a strong impact on the change in slope of $\left\langle r_c^2 \right\rangle$, with a more rapid increase when neutrons start to fill a new shell. One might expect to see a normal behaviour of increasing $\langle r_c^2 \rangle$ as a function of neutron number prior to $N = 50$, however the variations not only indicate a change of nuclear volume, but also departures from spherical symmetry.

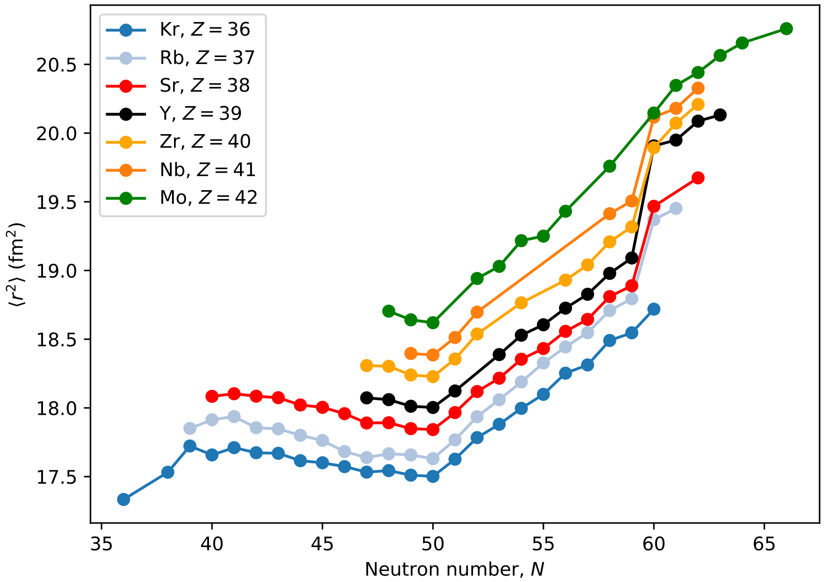

Fig. 17 Absolute nuclear mean-square charge radii as a function of neutron number in the Kr to Mo region, illustrating the sudden onset of deformation at $N = 60$.

Optical spectroscopy was initiated in the region approximately 40 years ago, with a series of measurements on rubidium ($Z = 37$) by Thibault et al. (1981b) revealing an abrupt increase in the ms charge radius between $N = 59$ and 60. The interest in this work prompted the development of variants in fast beam laser spectroscopy, including state-selective charge exchange (Silverans et al., 1987), photon-ion (atom) coincidence spectroscopy (Eastham et al., 1986) and optical pumping (Lievens et al., 1991) methods. Several of these methods were each first applied to the neighboring strontium chain ($Z = 38$) in which the sudden discontinuity at $N = 59$–60 in charge radius was also seen by Buchinger et al. (1990), however was notably absent in krypton ($Z = 36$) as reported by Keim et al. (1995). It would be important for future measurements to explore more neutron-rich krypton isotopes, to verify the departure of the discontinuity seen in the other $N = 60$ isotones up to niobium ($Z = 41$). We add that the results for the neutron-deficient krypton isotopes in the region of $N = Z = 36$ reflects the existence of shape coexistence between strongly prolate and near-spherical states, known from nuclear spectroscopy.

Production of elements above strontium was hindered by the refractory nature of the open d-shell species and their complex atomic structures. It was with the application of ion-guide technology at the IGISOL facility, combined with the gas-filled radio-frequency quadrupole (RFQ) cooler and buncher, that enabled optical spectroscopy to be performed on these higher-Z elements for the first time, namely zirconuim (Z = 40) (Campbell et al., 2002), yttrium (Z = 39) (Cheal et al., 2007), niobium (Z = 41) (Cheal et al., 2009) and molybdenum (Z=42) (Charlwood et al., 2009). Although the nuclear charge radii was accessible, yttrium and niobium both suffer from a J = 0 ionic ground state. In order to uniquely determine the nuclear spin and to access spectroscopic quadrupole moments, in-cooler optical pumping techniques were developed to provide spectroscopy away from the ground-state resonance lines. By illuminating the central axis of the ion beam cooler with laser light, an efficient redistribution of population out of the ground state into a selected metastable state occurs, from which collinear laser spectroscopy is performed. With sensitivity to the quadrupole moments enabled by this method, it was confirmed that the N = 60 shape change is truly to a rigid prolate deformation.

The current picture, as shown in Fig. 17, indicates that the yttrium isotopes are seemingly at the center of this phenomenon, with neighboring elements marking a reduction in the magnitude of deformation either side of this chain. The trends of charge radii in molybdenum are markedly different, with a gradual rise from the shell closure and a decrease observed at N = 66. We note that the trends in the charge radii closely reflect experimental tends in the two-neutron separation energies obtained from precision mass measurements, confirming molybdenum to be at the border of this region of deformation. Theoretically, the onset of deformation has been studied using self-consistent mean-field calculations based on the Gogny-D1S interaction by Rodríguez-Guzmán et al. (2010). Important correlations were found between shape transitions and sudden changes seen in the behavior of the nuclear charge radii. A qualitatively consistent agreement with experiment is seen, with the smooth trend in the molybdenum isotopes requiring triaxial degrees of freedom to obtain a good agreement beyond N = 60. Tantalisingly, recent theoretical efforts using the interacting boson model with configuration mixing (IBM-CM) by García-Ramos and Heyde (2020) provide direct predictions of charge radii for zirconium isotopes to ^{106}Zr, hopefully within reach of future facilities.

Shape coexistence and shape staggering in Hg

Shape coexistence is a remarkable phenomenon that appears to be unique to finite many-body quantum systems. It arises due to the subtle interplay between collective and single-particle behavior between nucleons and may therefore appear to some extent in almost all nuclei. Although there is no strict, universal, understanding of the mechanism of shape coexistence, often two coherent approaches are invoked, either within a nuclear shell model or via self-consistent mean field methods. In the former, the promotion of multiple particles (typically protons) across known shell closures increases the number of valence particles and holes that can interact with valence particles of the other type (typically neutrons). The correlation energies arising from both pairing and quadrupole-quadrupole interactions can overcome the cost in energy of promoting particles from one orbital to another. The nucleus thus re-organizes itself into new configurations possessing a different deformation from the initial (original) ground state without multi-particle multi-hole excitation. In the second approach, the motion of nucleons as independent quasiparticles is derived from effective forces and self-consistent Hartree-Fock-Bogoliubov (HFB) theory. A coexistence is generated via competing configurations based on different nuclear shapes. Whichever of these approaches is preferred, the essential ingredients include the occurrence of energy gaps as well as the mixing of the resulting configurations of protons and neutrons. A comprehensive review of shape coexistence can be found in Heyde and Wood (2011), published about a decade ago. Just recently, *experimental* evidence for shape coexistence in regions where the phenomenon has been suggested to emerge, as well as new results for well-documented regions, has been reviewed by Garrett et al. (2021).

Perhaps the most spectacular examples of shape coexistence are manifested in the transitional region extending from the rare-earth nuclei to the lead isotopes, in which a wealth of experimental information has been obtained. Although changes in mean-square charge radii are not direct spectroscopic fingerprints for coexistence, one of the earliest highlights was the discovery of an unprecedented increase in charge radii of neutron-deficient mercury ($Z = 80$) isotopes, ^{185}Hg, ^{183}Hg and ^{181}Hg, from optical hyperfine structure studies by Bonn et al. (1972), and Ulm et al. (1986). This observed pattern of “shape staggering” in Hg isotopes, indicated in Fig. 18, is unparalleled throughout the nuclear chart, motivating extensive interest in the region and the application of complementary techniques that probe the excited states of these nuclei. The large staggering observed has characteristic features of a quantum phase transition, with weakly deformed, oblate-shaped ground states and strongly-deformed, prolate-shaped states appearing at almost the same energy, alternating as a function of neutron number. Additionally, while the charge radius measured for the low-lying $13/2^-$ isomers in $^{187-191}$Hg closely follows the ground state trend, a larger difference is observed between ^{185m}Hg and ^{185}Hg.

It has taken almost thirty years to answer the question of where the shape staggering in mercury ends. In order to extend the reach of the earlier data, the highly sensitive method of in-source resonance ionization spectroscopy was applied at the ISOLDE facility by Marsh et al. (2018), successfully spanning 15 isotopes and extending the existing measurements to ^{177}Hg, having a half-life of 127 ms and a production rate of a few ions per minute. A three-step excitation and ionization scheme was employed, with spectroscopy performed on the 253.65-nm $6s^2\ ^1\mathrm{S}_0 \rightarrow 6s6p\ ^3\mathrm{P}_1$ transition. Well-resolved HFS spectra were obtained and the resulting isotopes were identified using one of three detection stations, depending on the lifetime, purity, intensity or decay mode. With this sensitive technique, an excellent agreement with the literature values validated the method, additionally providing new data showing that the staggering in the charge radius persists down to ^{179}Hg, at which mass the nucleus returns to sphericity in its ground state. In order to elucidate the underlying mechanism responsible for this localized region of dramatic shape staggering,

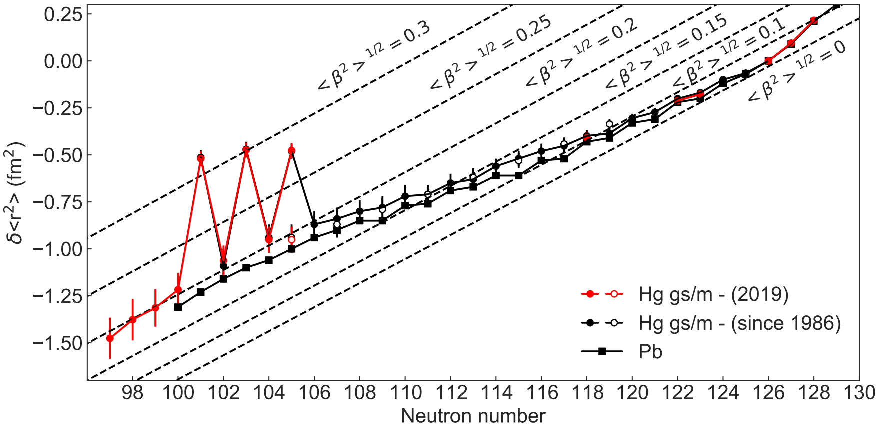

Fig. 18 Changes in mean-square charge radii as a function of neutron number for mercury and lead isotopes, relative to the shell closure at $N = 126$. Liquid droplet model isodeformation lines for various values of the deformation parameter β_2 are shown dashed. Figure courtesy of S. Sels.

a combination of large-scale numerical simulations using Monte Carlo shell model (MCSM) calculations as well as density functional theory (DFT) calculations were performed in Sels et al. (2019). The MCSM calculations highlight the importance of simultaneous multiple excitations to the proton $1h_{9/2}$ and neutron $1i_{13/2}$ orbitals, with the latter driving the large quadrupole deformation. The DFT calculations offer an interpretation of the charge radii trend in terms of the odd-even mass staggering that reflects the coexistence of nearly degenerate oblate and prolate minima.

In addition to the trends in the ms charge radii of mercury isotopes, Fig. 18 shows the corresponding lead isotopes for comparison, with in-source RIS affording access to ^{182}Pb. Unlike the mercury isotopes, the ground-state wavefunction of lead remains essentially spherical as the neutron mid-shell at $N = 104$ is crossed. Most recently, and fifty years after the original discovery of the shape staggering phenomenon in mercury, the in-source method has been used by Barzakh et al. (2021) to explore the lightest isotopes in the neighboring bismuth chain. By performing laser spectroscopy on ^{187,188,189,191}Bi, a sharp increase in the radius was seen for the ground state of ^{188}Bi relative to the ground states of ^{187,189}Bi, occurring at the exact same neutron number, $N = 105$, where the staggering starts in the mercury chain. This is only the second example of such striking behavior in the nuclear chart.

Heavy Elements

Laser spectroscopy of the heaviest elements is treated in a dedicated chapter within this Handbook of Nuclear Physics (Block, 2023) and therefore we will be brief in our discussion, focusing on the implications of charge radii measurements in this region. We also refer to a recent review that describes the most common experimental methods and selected recent results on the atomic and nuclear properties of the actinides ($89 \geq Z \geq 103$) up to nobelium ($Z = 102$) by Block et al. (2021). Some of the most challenging experiments lie within the actinide region and beyond, for which highly sensitive techniques are required. Despite the long-standing interest in the region, a paucity of ground state nuclear structure information exists above radium, the heaviest element studied online using collinear laser spectroscopy. This lack of data, unlike anywhere else in the nuclear chart, is a reflection of the scarcity of material and the complex atomic structure of these elements. Short-lived isotopes are not available at on-line isotope separator facilities and require production via fusion reactions in heavy-ion collisions or transfer reactions with radioactive targets. High-flux reactors can breed sufficient quantities of transuranium elements, however studies are then restricted to long-lived isotopes. Furthermore, a lack of stable isotopes in the region has resulted in limited atomic structure information (configuration assignments, atomic spins, hyperfine structure constants). These limitations add to the challenge of performing laser spectroscopy for ground-state nuclear structure.

As previously discussed, the neutron-deficient actinide region is favored for exploration of static octupole deformation in the ground state, with measurements of changes in ms charge radii a potential indicator of this collective phenomenon. Theoretical approaches to support the interpretation of the rather limited available experimental data are restricted to density functional theory, with computational scaling laws currently prohibiting various *ab initio* and configuration interaction approaches. Present energy density functional (EDF) models, generally speaking, have indicated rather good correspondence with charge radii data. For example, DFT calculations using the Skyrme parameterization UNEDF0 were compared with measurements of the charge radii in francium isotopes by Voss et al. (2015). A good agreement was seen close to the $N = 126$ shell closure albeit a certain deficiency with the model predictions emerged towards the lighter isotopes due to an overprediction of the intrinsic deformation. Several years after the successful hyperfine spectroscopy measurements of the short-lived ^{240f,242f,244f}Am fission isomers in a buffer gas cell Backe et al. (1998, 2000), the RADRIS technique afforded access to the differential ms charge radii of $^{252-254}$No, the latter at the deformed neutron shell closure $N = 152$ (Raeder et al., 2018). In general, the charge radii of the actinide isotopes increases rather linearly as a function of neutron number, differing slightly in the slopes for different chains. A droplet model parameterization, commonly used to explore axial quadrupole deformation in systems up to the lead region, shows deficiencies in high-Z elements that exhibit strong deformation. Density functional theory, again using a Skyrme functional, describes the available experimental data remarkably well (Raeder et al., 2018), even though the model has not been adapted specifically to charge radii, nor to the actinide region. It is noteworthy that the calculated charge distribution for ^{254}No reveals a central depression of about 10%, originating from the strong Coulomb repulsion in these heavy systems. Future measurements, in combination with more sophisticated state-of-the-art atomic calculations, are required to explore this fascinating effect in heavier nuclei.

Lastly, we look forward to the application of the Fayans functionals to the actinide region in the future. These functionals have been optimized with a focus on charge radii and applied to successfully reproduce trends in lighter systems, for example calcium, copper and cadmium. Systematic calculations including the octupole degree of freedom, together with new experimental measurements of the charge radius, would be a crucial test for this model. Additionally, an important issue in the development of next generation energy density functional models is the assessment of predictive power and theoretical uncertainties. In extrapolation to experimentally unknown regions, such as the actinides, the role of model uncertainties becomes prominent and therefore theoretical and experimental efforts will both be required to exploit this interesting region of the nuclear chart.

Outlook

Information about the strong and electromagnetic forces acting within the atomic nucleus can be probed via measurements of nuclear charge radii. A wealth of rich structural phenomena has been explored over many years, arising from the quantum motion of the proton and neutron constituents. Shell and subshell effects, halo structures and clustering, pairing correlations and mixing, nuclear deformation, shape staggering, and shape coexistence are all topical features of current experimental and theoretical interest. Furthermore, nuclear charge radii have been linked to the properties of infinite matter and radii of neutron stars.

In recent years, impressive advancements in *ab initio* calculations have enabled an exploration of bulk nuclear properties, specifically ground-state energies, charge radii and density distributions towards medium-mass nuclei. Relative trends in charge radii are generally well reproduced, however, calculations often underestimate the absolute value of the experimental measurements, pointing to a possible bulk systematic deficiency in the used Hamiltonians. Clearly, for open-shell systems, quadrupole correlations are expected to play an important role, inviting alternative theoretical long-term developments. Ultimately, *ab initio* theory aims to provide a universal framework for the prediction of low-energy nuclear phenomena across the nuclear landscape. Currently, density functional theory remains the only microscopic theory which can be applied throughout the entire nuclear chart. Different parameterizations have been developed over the years and have been benchmarked with nuclear charge radii, exploring odd-even staggering as well as the nature of the kinks at shell closures. Recent efforts have led to an exploration of the interplay of quadrupole deformation and pairing correlations in deformed open shell nuclei. The development of next generation energy density functionals will involve the assessment of predictive power and theoretical model uncertainties. Extrapolation to unknown regions, for example actinide nuclei, will require both theoretical and experimental data.

The combination of modern laser spectroscopic techniques and powerful radioactive beam facilities have offered experimental access to regions across the nuclear landscape, from the lightest halo nuclei to the heaviest elements, spanning long chains of isotopes on both sides of stability. Over the years, considerable evolution and refinement of the traditional workhorses, namely collinear laser spectroscopy and in-source resonance ionization spectroscopy, has been made in order to realize measurements towards ever more challenging cases. The application of radiofrequency cooler-buncher devices, collinear resonance ionization techniques and trapping of cold atoms and ions has opened up new possibilities for the study of nuclei with high sensitivity and production rates of only a few atoms per second. Detection techniques have dramatically improved over the years, and the field has witnessed a combination of methodologies that potentially can be used to extract a full set of nuclear observables, for example laser-assisted decay spectroscopy, multi-reflection time-of-flight devices and Penning-trap methods combined with in-source spectroscopy. This trend is expected to continue with increasing demands on sensitivity and precision.

Several areas of the nuclear chart remain unexplored, for example a number of late d-shell elements, the majority of non-metals (excluding the noble gases) and elements beyond $Z = 102$ lack reports of radioactive measurements. Many of these regions have been restricted mainly due to chemistry and atomic structure constraints. With the aforementioned developments in the techniques, matched in the longer-term by more powerful facilities coming on-line, for example FAIR, FRIB and SPIRAL2, that promise more intense beams as well as beams that have been chemically difficult to produce, optical spectroscopy will finally address these challenging regions, remaining active and fruitful in the future.

At least three future non-optical experiments aim to provide absolute values of ms charge radii, or precision changes in ms charge radii for radioactive isotopes, namely the SCRIT facility at RIKEN, the muX project at the Paul Scherrer Institut (PSI) and the use of dielectronic recombination spectroscopy in storage rings, as already demonstrated at GSI. At SCRIT, electron scattering measurements will be made on confined radioactive ions. Results for radioactive isotopes from any of these experiments could act as calibrants for optical data. Such measurements would also provide valuable tests for the confidence of large-scale atomic structure calculations used in the determination of atomic factors. Presently, the precision of these calculations is generally explored in relative comparisons of atomic and ionic transitions.

Lastly, we note exciting new opportunities are currently on the horizon, in which high-precision measurements of nuclear charge radii will play a role. For example, isotope shift measurements offer unique information on fundamental symmetries of nature. The role of precision spectroscopy in searches for physics beyond the Standard Model (SM) has recently been emphasized via new ideas pointing to the manifestation of beyond-SM physics scenarios in the isotope shifts of atomic spectra (Berengut et al., 2018). Radioactive molecules hold particular promise for high sensitivity studies of parity- and time-reversal-violation effects (Garcia Ruiz et al., 2020), necessitating applications of the techniques developed at radioactive beam facilities over the years. These opportunities are examples in which we look forward to the field branching from traditional low-energy nuclear structure physics to multidisciplinary fields of science in the future.

References

??? *Nuclear Physics Handbook*, chapter ... Springer, New York, 2023.

S. A. Ahmad et al. Mean square charge radii of radium isotopes and octupole deformation in the $^{220--228}$Ra region. *Nuclear Physics A*, 483:244–268, 1988.

G. D. Alkhazov et al. Measurement of isotropic variations in the charge radii of europium nuclei by the method of three-stepped laser photoionization of atoms. *JETP Lett.*, 37:274, 1983.

G.D. Alkhazov et al. A new highly efficient method of atomic spectroscopy for nuclides far from stability. *Nuclear Instruments and Methods in Physics Research Section B*, 69:517–520, 1992. doi: https://doi.org/10.1016/0168-583X(92)95309-F.

R. V. Ambartsumyan, V. N. Kalinin, and V. S. Letokhov. Two-step selective photoionization of rubidium atoms by laser radiation. *JETP Lett.*, 13:217–9, 1971.

I. Angeli and K.P. Marinova. Correlations of nuclear charge radii with other nuclear observables. *Journal of Physics G*, 42:055108, 2015.

A. Antognini et al. Proton structure from the measurement of 2S-2P transition frequencies of muonic hydrogen. *Science*, 339:417–420, 2013. doi: 10.1126/science.1230016.

A. Antognini et al. Measurement of the quadrupole moment of ^{185}Re and ^{187}Re from the hyperfine structure of muonic X rays. *Phys. Rev. C*, 101:054313, 2020. doi: 10.1103/PhysRevC.101.054313.

K.-R. Anton et al. Collinear Laser Spectroscopy on Fast Atomic Beams. *Physical Review Letters*, 40:642–645, 1978.

J. Ärje et al. Submillisecond On-Line Mass Separation of Nonvolatile Radioactive Elements: An Application of Charge Exchange and Thermalization Processes of Primary Recoil Ions in Helium. *Phys. Rev. Lett.*, 54:99–101, 1985. doi: 10.1103/PhysRevLett.54.99.

H. Backe, A. Dretzke, M. Hies, G. Kube, H. Kunz, W. Lauth, M. Sewtz, N. Trautmann, R. Repnow, and H. J. Maier. Isotope shift measurement at 244fam *. *Hyperfine Interactions*, 127(1):35–39, Aug 2000. ISSN 1572-9540. doi: 10.1023/A:1012690022283. URL `https://doi.org/10.1023/A:1012690022283`.

H. Backe, W. Lauth, M. Block, and M. Laatiaoui. Prospects for laser spectroscopy, ion chemistry and mobility measurements of superheavy elements in buffer-gas traps. *Nuclear Physics A*, 944:492–517, 2015. doi: https://doi.org/10.1016/j.nuclphysa.2015.07.002.

H. Backe et al. Isotope Shift Measurements for Superdeformed Fission Isomeric States. *Phys. Rev. Lett.*, 80:920–923, 1998.

F. Barranco and R. A. Broglia. Correlation between mean square radii and zero-point motions of the surface in the ca isotopes. *Physics Letters B*, 151:90–94, 1985.

R. C. Barrett. Model-independent parameters of the nuclear charge distribution from muonic X-rays. *Physics Letters B*, 33:388–390, 1970. doi: 10.1016/0370-2693(70)90611-8.

A. Barzakh et al. Large shape staggering in neutron-deficient bi isotopes. *Phys. Rev. Lett.*, 127:192501, 2021. doi: 10.1103/PhysRevLett.127.192501.

M. A. Belushkin, H.-W. Hammer, and Ulf-G. Meißner. Dispersion analysis of the nucleon form factors including meson continua. *Physical Review C*, 75, 2007. doi: 10.1103/PhysRevC.75.035202.

J. C. Berengut et al. Probing New Long-Range Interactions by Isotope Shift Spectroscopy. *Phys. Rev. Lett.*, 120:091801, 2018. doi: 10.1103/PhysRevLett.120.091801.

J. C. Bernauer et al. High-Precision Determination of the Electric and Magnetic Form Factors of the Proton. *Physical Review Letters*, 105:242001, 2010.

A. Beyer et al. The rydberg constant and proton size from atomic hydrogen. *Science*, 358:79–85, 2017. doi: 10.1126/science.aah6677.

N. Bezginov et al. A measurement of the atomic hydrogen Lamb shift and the proton charge radius. *Science*, 365:1007–1012, 2019. doi: 10.1126/science.aau7807.

K. Blaum et al. A novel scheme for a highly selective laser ion source. *Nuclear Instruments and Methods in Physics Research Section B*, 204:331 – 335, 2003. doi: http://dx.doi.org/10.1016/S0168-583X(02)01942-0.

M. Block. *Nuclear Physics Handbook*, chapter Nuclear Moments. Springer, New York, 2023.

M. Block, M. Laatiaoui, and S. Raeder. Recent progress in laser spectroscopy of the actinides. *Progress in Particle and Nuclear Physics*, 116:103834, 2021. doi: https://doi.org/10.1016/j.ppnp.2020.103834.

J. Bonn et al. Sudden change in the nuclear charge distribution of very light mercury isotopes. *Physics Letters B*, 38:308 – 311, 1972. doi: http://dx.doi.org/10.1016/0370-2693(72)90253-5.

W. Borchers, R. Neugart, E. W. Otten, H. T. Duong, G. Ulm, and K. Wendt. Hyperfine structure and isotope shift investigations in $^{202--222}$Rn for the study of nuclear structure beyond $Z = 82$. *Hyperfine Interactions*, 34:25–29, 1987. doi: 10.1007/BF02072676.

S. Bourzeix et al. High resolution spectroscopy of the hydrogen atom: Determination of the 1S Lamb shift. *Physical Review Letters*, 76(3):384–387, 1996. ISSN 0031-9007. doi: 10.1103/PhysRevLett.76.384.

C. Brandau et al. Precise Determination of the $2s_{1/2}{-}2p_{1/2}$ Splitting in Very Heavy Lithiumlike Ions Utilizing Dielectronic Recombination. *Phys. Rev. Lett.*, 91:073202, 2003. doi: 10.1103/PhysRevLett.91.073202.

C. Brandau et al. Isotope Shift in the Dielectronic Recombination of Three-Electron ^{A}Nd^{57+}. *Phys. Rev. Lett.*, 100:073201, 2008. doi: 10.1103/PhysRevLett.100.073201.

B. H. Bransden and C. J. Joachain. *Physics of Atoms and Molecules*. Prentice Hall, 2003. ISBN 9780582356924.

F. Buchinger et al. Systematics of nuclear ground state properties in $^{78-100}$Sr by laser spectroscopy. *Phys. Rev. C*, 41:2883–2897, 1990. doi: 10.1103/PhysRevC.41.2883.

P. A. Butler et al. Evolution of Octupole Deformation in Radium Nuclei from Coulomb Excitation of Radioactive ^{222}Ra and ^{228}Ra Beams. *Phys. Rev. Lett.*, 124:042503, 2020. doi: 10.1103/PhysRevLett.124.042503.

R. B. Cakirli, R. F. Casten, and K. Blaum. Correlations of experimental isotope shifts with spectroscopic and mass observables. *Phys. Rev. C*, 82:061306, 2010. doi: 10.1103/PhysRevC.82.061306.

P. Campbell et al. Laser Spectroscopy of Cooled Zirconium Fission Fragments. *Phys. Rev. Lett.*, 89:082501, 2002. doi: 10.1103/PhysRevLett.89.082501.

Y. Cao et al. Landscape of pear-shaped even-even nuclei. *Phys. Rev. C*, 102:024311, 2020. doi: 10.1103/PhysRevC.102.024311.

R.F. Casten. NpNn systematics in heavy nuclei. *Nuclear Physics A*, 443:1–28, 1985. doi: https://doi.org/10.1016/0375-9474(85)90318-5.

E. Caurier et al. Shell model description of isotope shifts in calcium. *Physics Letters B*, 522:240–244, 2001.

F. C. Charlwood et al. Nuclear charge radii of molybdenum fission fragments. *Physics Letters B*, 674:23–27, 2009. doi: 10.1016/j.physletb.2009.02.050.

B. Cheal, T. E. Cocolios, and S. Fritzsche. Laser spectroscopy of radioactive isotopes: Role and limitations of accurate isotope-shift calculations. *Phys. Rev. A*, 86:042501, 2012. doi: 10.1103/PhysRevA.86.042501.

B. Cheal et al. The shape transition in the neutron-rich yttrium isotopes and isomers. *Physics Letters B*, 645:133–137, 2007. doi: 10.1016/j.physletb.2006.12.053.

B. Cheal et al. Laser Spectroscopy of Niobium Fission Fragments: First Use of Optical Pumping in an Ion Beam Cooler Buncher. *Phys. Rev. Lett.*, 102:222501, 2009. doi: 10.1103/PhysRevLett.102.222501.

P. Chhetri et al. Precision Measurement of the First Ionization Potential of Nobelium. *Phys. Rev. Lett.*, 120:263003, 2018. doi: 10.1103/PhysRevLett.120.263003.

H. Choi et al. In-gas-cell laser ionization spectroscopy of ^{194,196}Os isotopes by using a multireflection time-of-flight mass spectrograph. *Phys. Rev. C*, 102:034309, 2020. doi: 10.1103/PhysRevC.102.034309.

C. Cohen-Tannoudji, J. Dupont-Roc, and G. Grynberg. *Atom-Photon Interactions*. John Wiley & Sons, New York, 1998. ISBN 0471293369.

R. P. de Groote et al. Dipole and quadrupole moments of $^{73\text{–}78}$Cu as a test of the robustness of the $Z = 28$ shell closure near ^{78}Ni. *Phys. Rev. C*, 96:041302, 2017. doi: 10.1103/PhysRevC.96.041302.

R. P. de Groote et al. Measurement and microscopic description of odd–even staggering of charge radii of exotic copper isotopes. *Nature Physics*, 16:620–624, 2020. doi: 10.1038/s41567-020-0868-y.

H. De Witte et al. Nuclear Charge Radii of Neutron-Deficient Lead Isotopes Beyond $N = 104$ Midshell Investigated by In-Source Laser Spectroscopy. *Phys. Rev. Lett.*, 98:112502, 2007. doi: 10.1103/PhysRevLett.98.112502.

H. DeVries, C. W. DeJager, and C. DeVries. Nuclear Charge-Density-Distribution Parameters from Elastic Electron-Scattering. *Atomic Data and Nuclear Data Tables*, 36:495–536, 1987.

G. W. F. Drake. High-Precision Calculations for the Rydberg States of Helium. In Frank S. Levin and David A. Micha, editors, *Long-Range Casimir Forces: Theory and Recent Experiments on Atomic Systems*, pages 107–217. Springer US, Boston, MA, 1993. doi: 10.1007/978-1-4899-1228-2{_}3.

B. Dreher et al. The determination of the nuclear ground state and transition charge density from measured electron scattering data. *Nuclear Physics A*, 235:219–248, 1974. doi: 10.1016/0375-9474(74)90189-4.

H.T. Duong, J. Pinard, S. Liberman, G. Savard, J.K.P. Lee, J.E. Crawford, G. Thekkadath, F. Le Blanc, P. Kilcher, J. Obert, J. Oms, J.C. Putaux, B. Roussière, and J. Sauvage. Shape transition in neutron deficient pt isotopes. *Physics Letters B*, 217(4):401 – 405, 1989. ISSN 0370-2693. doi: http://dx.doi.org/10.1016/0370-2693(89)90068-3. URL `http://www.sciencedirect.com/science/article/pii/0370269389900683`.

D. A. Eastham et al. Coincidence Laser Spectroscopy - a New Ultrasensitive Technique for Fast Ionic or Atomic-Beams. *Optics Communications*, 60:293–295, 1986.

S. Eliseev et al. Phase-Imaging Ion-Cyclotron-Resonance Measurements for Short-Lived Nuclides. *Phys. Rev. Lett.*, 110:082501, 2013.

J. Engel et al. Time-reversal violating schiff moment of ^{225}Ra. *Phys. Rev. C*, 68: 025501, 2003. doi: 10.1103/PhysRevC.68.025501.

G. Ewald et al. Nuclear Charge Radii of ^{8,9}Li Determined by Laser Spectroscopy. *Physical Review Letters*, 93:113002, 2004.

G. J. Farooq-Smith et al. Laser and decay spectroscopy of the short-lived isotope ^{214}Fr in the vicinity of the $N = 126$ shell closure. *Phys. Rev. C*, 94:054305, 2016. doi: 10.1103/PhysRevC.94.054305.

V.N. Fedoseyev et al. Atomic lines isotope shifts of short-lived radioactive Eu studied by high-sensitive laser resonance photoionization method in on-line experiments with proton beams. *Optics Communications*, 52:24 – 28, 1984. doi: http://dx.doi.org/10.1016/0030-4018(84)90067-1.

V. N. Fedosseev, Yu. Kudryavtsev, and V. I. Mishin. Resonance laser ionization of atoms for nuclear physics. *Physica Scripta*, 85:058104, 2012. doi: 10.1088/0031-8949/85/05/058104.

V.N. Fedosseev et al. Atomic spectroscopy studies of short-lived isotopes and nuclear isomer separation with the ISOLDE RILIS. *Nuclear Instruments and Methods in Physics Research Section B*, 204:353 – 358, 2003. doi: http://dx.doi.org/10.1016/S0168-583X(02)01959-6.

R. Ferrer et al. Towards high-resolution laser ionization spectroscopy of the heaviest elements in supersonic gas jet expansion. *Nature Communications*, 8:14520, 2017. doi: 10.1038/ncomms14520.

R. Ferrer et al. Hypersonic nozzle for laser-spectroscopy studies at 17 K characterized by resonance-ionization-spectroscopy-based flow mapping. *Phys. Rev. Research*, 3:043041, 2021. doi: 10.1103/PhysRevResearch.3.043041.

D. A. Fink et al. In-source laser spectroscopy with the laser ion source and trap: First direct study of the ground-state properties of ^{217,219}Po. *Phys. Rev. X*, 5:011018, 2015. doi: 10.1103/PhysRevX.5.011018.

H. Fleurbaey et al. New Measurement of the 1S-3S Transition Frequency of Hydrogen: Contribution to the Proton Charge Radius Puzzle. *Physical Review Letters*, 120:183001, 2018. doi: 10.1103/PhysRevLett.120.183001.

J. L. Friar and J. W. Negele. Theoretical and Experimental Determination of Nuclear Charge Distributions. In Michel Baranger and Erich Vogt, editors, *Advances in Nuclear Physics*, volume 8, pages 219–376. Springer US, Boston, MA and s.l., 1975. doi: 10.1007/978-1-4757-4398-2{_}3.

J. L. Friar, J. Martorell, and D. W. L. Sprung. Nuclear sizes and the isotope shift. *Physical Review A*, 56:4579–4586, 1997.

G. Fricke and K. Heilig. *Nuclear Charge Radii*, volume 20 of *Elementary Particles, Nuclei and Atoms*. Springer-Verlag Berlin Heidelberg, 2004.

G. Fricke et al. Nuclear Ground State Charge Radii from Electromagnetic Interactions. *Atomic Data and Nuclear Data Tables*, 60:177–285, 1995.

L. P. Gaffney et al. Studies of pear-shaped nuclei using accelerated radioactive beams. *Nature*, 497:199–204, 2013. doi: 10.1038/nature12073.

H. Gao and M. Vanderhaeghen. The proton charge radius. *Reviews of Modern Physics*, 94, 2022. ISSN 0034-6861. doi: 10.1103/RevModPhys.94.015002.

J. E. García-Ramos and K. Heyde. Subtle connection between shape coexistence and quantum phase transition: The Zr case. *Phys. Rev. C*, 102:054333, 2020. doi: 10.1103/PhysRevC.102.054333.

R. F. Garcia Ruiz et al. Development of a sensitive setup for laser spectroscopy studies of very exotic calcium isotopes. *Journal of Physics G*, 44:044003, 2017.

R. F. Garcia Ruiz et al. Spectroscopy of short-lived radioactive molecules. *Nature*, 581:396–400, 2020. doi: 10.1038/s41586-020-2299-4.

P. E. Garrett, M. Zielińska, and E. Clément. An experimental view on shape coexistence in nuclei. *Progress in Particle and Nuclear Physics*, page 103931, 2021. doi: https://doi.org/10.1016/j.ppnp.2021.103931.

H. Geiger and E. Marsden. On the scattering of the α-particles by matter. *Proc. Roy. Soc. Lond. A*, 81(546):174–177, 1908. doi: 10.1098/rspa.1908.0067.

H. Geiger and E. Marsden. On a diffuse reflection of the α-particles. *Proc. Roy. Soc. Lond. A*, 82(557):495–500, 1909. doi: 10.1098/rspa.1909.0054.

H. Geiger and E. Marsden. The scattering of α-particles by matter. *Proc. Roy. Soc. Lond. A*, 83(565):492–504, 1910. doi: 10.1098/rspa.1910.0038.

R. J. Glauber. Theory of high energy hadron-nucleus collisions. In Samuel Devons, editor, *High-Energy Physics and Nuclear Structure*, pages 207–264, Boston, MA, 1970. Springer US.

P. M. Goddard, P. D. Stevenson, and A. Rios. Charge Radius Isotope Shift Across the N=126 Shell Gap. *Phys. Rev. Lett.*, 110:032503, 2013. doi: 10.1103/PhysRevLett.110.032503.

C. Gorges et al. Isotope shift of ^{40,42,44,48}Ca in the $4s\,^2S_{1/2} \rightarrow 4p\,^2P_{3/2}$ transition. *Journal of Physics B*, 48:245008, 2015.

C. Gorges et al. Laser Spectroscopy of Neutron-Rich Tin Isotopes: A Discontinuity in Charge Radii across the $N = 82$ Shell Closure. *Phys. Rev. Lett.*, 122:192502, 2019. doi: 10.1103/PhysRevLett.122.192502.

C. Granados et al. In-gas laser ionization and spectroscopy of actinium isotopes near the $n = 126$ closed shell. *Phys. Rev. C*, 96:054331, 2017. doi: 10.1103/PhysRevC.96.054331.

A. Grinin et al. Two-photon frequency comb spectroscopy of atomic hydrogen. *SCIENCE*, 370:1061–1066, 2020. doi: 10.1126/science.abc7776.

G. Hagen et al. Neutron and weak-charge distributions of the ^{48}Ca nucleus. *Nat Phys*, 12:186–190, 2016. doi: 10.1038/nphys3529.

L. N. Hand, D. G. Miller, and Richard Wilson. Electric and magnetic form factors of the nucleon. *Reviews of Modern Physics*, 35(2):335–349, 1963. ISSN 0034-6861. doi: 10.1103/RevModPhys.35.335.

R. Heinke et al. High-resolution in-source laser spectroscopy in perpendicular geometry. *Hyperfine Interactions*, 238:6, 2016. doi: 10.1007/s10751-016-1386-2.

K. Heyde and J. L. Wood. Shape coexistence in atomic nuclei. *Rev. Mod. Phys.*, 83: 1467–1521, 2011. doi: 10.1103/RevModPhys.83.1467.

Th. Hilberath, St. Becker, G. Bollen, H. J. Kluge, U. Krönert, G. Passler, J. Rikovska, and R. Wyss. Ground-state properties of neutron-deficient platinum isotopes. *Zeitschrift für Physik A*, 342:1–15, 1992. doi: 10.1007/BF01294481.

Y. Hirayama et al. Doughnut-shaped gas cell for KEK Isotope Separation System. *Nuclear Instruments and Methods in Physics Research Section B*, 412:11–18, 2017. doi: https://doi.org/10.1016/j.nimb.2017.08.037.

G. S. Hurst and M. G. Payne. *Principles and Applications of Resonance Ionzation Spectroscopy*. Bristol: Hilger, 1988.

R. L. Jaffe. Ambiguities in the definition of local spatial densities in light hadrons. *Physical Review D*, 103, 2021. doi: 10.1103/PhysRevD.103.016017.

J. A. Jansen, R. Th. Peerdeman, and C. de Vries. Nuclear charge radii of ^{12}C and ^{9}Be. *Nuclear Physics A*, 188:337–352, 1972.

R. Kanungo et al. Proton Distribution Radii of $12-19$C Illuminate Features of Neutron Halos. *Physical Review Letters*, 117:102501, 2016.

J.-P. Karr, Do. Marchand, and E. Voutier. The proton size. *Nature Reviews Physics*, 2:601–614, 2020. doi: 10.1038/s42254-020-0229-x.

S. L. Kaufman. High-resolution laser spectroscopy in fast beams. *Optics Communications*, 17:309–312, 1976. doi: 10.1016/0030-4018(76)90267-4.

M. Keim et al. Laser-spectroscopy measurements of $^{72-96}$Kr spins, moments and charge radii . *Nuclear Physics A*, 586:219 – 239, 1995. doi: http://dx.doi.org/10.1016/0375-9474(94)00786-M.

W. H. King. *Isotope Shifts in Atomic Spectra*. Physics of Atoms and Molecules Series. Springer, New York, NY, 1984. ISBN 9781489917867.

A. Klose et al. Tests of atomic charge-exchange cells for collinear laser spectroscopy. *Nuclear Instruments and Methods in Physics Research Section A*, 678: 114–121, 2012.

K. König et al. A new Collinear Apparatus for Laser Spectroscopy and Applied Science (COALA). *Review of Scientific Instruments*, 91:081301, 2020. doi: 10.1063/5.0010903.

H. Kopferman. *Nuclear Moments*. Elsevier Science, Burlington, 2nd ed. edition, 1958. ISBN 9781483230610.

M. Kortelainen et al. Universal trend of charge radii of even-even Ca–Zn nuclei. *Physical Review C*, 105, 2022. doi: 10.1103/PhysRevC.105.L021303.

Á. Koszorús et al. Charge radii of exotic potassium isotopes challenge nuclear theory and the magic character of N=32. *Nature Physics*, 17:439–443, 2021. doi: 10.1038/s41567-020-01136-5.

J. J. Krauth et al. Measuring the α-particle charge radius with muonic helium-4 ions. *Nature*, 589:527–531, 2021. doi: 10.1038/s41586-021-03183-1.

A. Krieger et al. Calibration of the isolde acceleration voltage using a high-precision voltage divider and applying collinear fast beam laser spectroscopy. *Nuclear Instruments and Methods in Physics Research A*, 632:23–31, 2011.

A. Krieger et al. Nuclear Charge Radius of 12Be. *Phys. Rev. Lett.*, 108:142501, 2012.

A. Krieger et al. Frequency-comb referenced collinear laser spectroscopy of Be$^+$ for nuclear structure investigations and many-body QED tests. *Applied Physics B*, 123:15, 2017. doi: 10.1007/s00340-016-6579-5.

T. Kron et al. Hyperfine structure study of ^{97,98,99}Tc in a new laser ion source for high-resolution laser spectroscopy. *Phys. Rev. C*, 102:034307, 2020. doi: 10.1103/PhysRevC.102.034307.

U. Krönert et al. Resonance lonization mass spectroscopy with a pulsed thermal atomic beam. *Applied Physics A*, 44:339–345, 1987. doi: 10.1007/BF00624601.

Yu.A. Kudriavtsev and V.S. Letokhov. Laser method of highly selective detection of rare radioactive isotopes through multistep photoionization of accelerated atoms. *Applied Physics B*, 29:219–221, 1982. doi: 10.1007/BF00688671.

Yu. Kudryavtsev et al. Dual chamber laser ion source at LISOL. *Nuclear Instruments and Methods in Physics Research Section B:*, 267:2908 – 2917, 2009. doi: http://dx.doi.org/10.1016/j.nimb.2009.06.013.

M. Laatiaoui et al. Atom-at-a-time laser resonance ionization spectroscopy of nobelium. *Nature*, 538:495–498, 2016. doi: 10.1038/nature19345.

J. K. P. Lee, G. Savard, J. E. Crawford, G. Thekkadath, H. T. Duong, J. Pinard, S. Liberman, F. Le Blanc, P. Kilcher, J. Obert, J. Oms, J. C. Putaux, B. Roussière, and J. Sauvage. Resonant ionization spectroscopy of laser-desorbed gold isotopes. *AIP Conference Proceedings*, 164(1):205–208, 1987. doi: http://dx.doi.org/10.1063/1.37034. URL `http://scitation.aip.org/content/aip/proceeding/aipcp/10.1063/1.37034`.

J. K. P. Lee, G. Savard, J. E. Crawford, G. Thekkadath, H. T. Duong, J. Pinard, S. Liberman, F. Le Blanc, P. Kilcher, J. Obert, J. Oms, J. C. Putaux, B. Roussière, and J. Sauvage. Charge-radius changes in even-A platinum nuclei. *Phys. Rev. C*, 38:2985–2988, Dec 1988. doi: 10.1103/PhysRevC.38.2985. URL `http://link.aps.org/doi/10.1103/PhysRevC.38.2985`.

M. Lestinsky et al. Physics book: Cryring@esr. *The European Physical Journal - Special Topics*, 225:797–882, 2016. doi: 10.1140/epjst/e2016-02643-6.

V. S. Letokhov. *Laser Photoionization Spectroscopy*. Orlando FL: Academic, 1987.

P. Lievens, R.E. Silverans, L. Vermeeren, W. Borchers, W. Neu, R. Neugart, K. Wendt, F. Buchinger, and E. Arnold. Nuclear ground state properties of 99sr by collinear laser spectroscopy with non-optical detection. *Physics Letters B*, 256(2):141 – 145, 1991. ISSN 0370-2693. doi: http://dx.doi.org/10.1016/0370-2693(91)90664-C. URL `http://www.sciencedirect.com/science/article/pii/037026939190664C`.

Y.-H. Lin, H.-W. Hammer, and U.-G. Meißner. High-precision determination of the electric and magnetic radius of the proton. *Physics Letters B*, 816:136254, 2021. doi: 10.1016/j.physletb.2021.136254.

Z. T. Lu et al. Colloquium: Laser probing of neutron-rich nuclei in light atoms. *Reviews of Modern Physics*, 85:1383–1400, 2013.

K. M. Lynch et al. Decay-Assisted Laser Spectroscopy of Neutron-Deficient Francium. *Physical Review X*, 4, 2014.

B. Maaß et al. Towards laser spectroscopy of the proton-halo candidate ^{8}B. *Hyperfine Interactions*, 238:25, 2017. doi: 10.1007/s10751-017-1399-5.

B. Maaß et al. Nuclear Charge Radii of ^{10,11}B. *Phys. Rev. Lett.*, 122:182501, 2019. doi: 10.1103/PhysRevLett.122.182501.

S. Malbrunot-Ettenauer et al. Nuclear Charge Radii of the Nickel Isotopes $^{58-68,70}$Ni. *Phys. Rev. Lett.*, 128:022502, 2022. doi: 10.1103/PhysRevLett.128.022502.

B. A. Marsh et al. Characterization of the shape-staggering effect in mercury nuclei. *Nature Physics*, 14:1163–1167, 2018. doi: 10.1038/s41567-018-0292-8.

A. J. Miller et al. Proton superfluidity and charge radii in proton-rich calcium isotopes. *Nature Physics*, 15:432–436, 2019. doi: 10.1038/s41567-019-0416-9.

Gerald A. Miller. Defining the proton radius: A unified treatment. *Physical Review C*, 99:035202, 2019. doi: 10.1103/PhysRevC.99.035202.

Peter J. Mohr, David B. Newell, and Barry N. Taylor. CODATA recommended values of the fundamental physical constants: 2014. *Reviews of Modern Physics*, 88:035009, 2016. doi: 10.1103/RevModPhys.88.035009.

A. C. Mueller et al. Spins, moments and charge radii of barium isotopes in the range $^{122-146}$Ba determined by collinear fast-beam laser spectroscopy. *Nuclear Physics A*, 403:234–262, 1983.

M. Mukai et al. In-gas-cell laser resonance ionization spectroscopy of ^{196,197,198}Ir. *Phys. Rev. C*, 102:054307, 2020. doi: 10.1103/PhysRevC.102.054307.

P. Müller et al. Nuclear Charge Radius of ^{8}He. *Phys. Rev. Lett.*, 99:252501, 2007. doi: 10.1103/PhysRevLett.99.252501.

William D. Myers and W. J. Swiatecki. Average nuclear properties. *Annals of Physics*, 55:395–505, 1969. doi: 10.1016/0003-4916(69)90202-4.

A. Navin et al. Direct Evidence for the Breakdown of the N=8 Shell Closure in ^{12}Be. *Phys. Rev. Lett.*, 85:266–269, 2000. doi: 10.1103/PhysRevLett.85.266.

R. Neugart, W. Klempt, and K. Wendt. Collisional ionization as a sensitive detection scheme in collinear laser-fast-beam spectroscopy. *Nuclear Instruments and Methods in Physics Research B*, 17:354–359, 1986.

R. Neugart et al. Precision Measurement of ^{11}Li Moments: Influence of Halo Neutrons on the ^{9}Li Core. *Phys. Rev. Lett.*, 101:132502, 2008.

G. Neyens. *Nuclear Physics Handbook*, chapter Nuclear Moments. Springer, New York, 2023.

A. Nieminen et al. On-Line Ion Cooling and Bunching for Collinear Laser Spectroscopy. *Physical Review Letters*, 88:094801, 2002.

NIST. 2018 codata recommended values, 2022. URL `https://physics.nist.gov/cgi-bin/cuu/Value?rp|search_for=proton+radius`.

W. Nörtershäuser et al. Nuclear Charge Radii of ^{7,9,10}Be and the One-Neutron Halo Nucleus ^{11}Be. *Phys. Rev. Lett.*, 102:062503, 2009. doi: 10.1103/Physrevlett.102.062503.

W. Nörtershäuser et al. Isotope-shift measurements of stable and short-lived lithium isotopes for nuclear-charge-radii determination. *Physical Review A*, 83:012516, 2011a.

W. Nörtershäuser et al. Charge radii and ground state structure of lithium isotopes: Experiment and theory reexamined. *Physical Review C*, 84:024307, 2011b.

G. Papadimitriou et al. Charge radii and neutron correlations in helium halo nuclei. *Physical Review C*, 84:051304, 2011.

C. G. Parthey et al. Improved Measurement of the Hydrogen 1S-2S Transition Frequency. *Phys. Rev. Lett.*, 107:203001, 2011.

V. Patkóš, V. A. Yerokhin, and K. Pachucki. Complete α^7m Lamb shift of helium triplet states. *Physical Review A*, 103, 2021. doi: 10.1103/PhysRevA.103.042809.

U. C. Perera, A. V. Afanasjev, and P. Ring. Charge radii in covariant density functional theory: A global view. *Physical Review C*, 104, 2021. doi: 10.1103/PhysRevC.104.064313.

R. Pohl, R. Gilman, G. A. Miller, and K. Pachucki. Muonic Hydrogen and the Proton Radius Puzzle. *Annual Review of Nuclear and Particle Science*, 63:175–204, 2013. doi: 10.1146/annurev-nucl-102212-170627.

R. Pohl et al. The size of the proton. *Nature*, 466:213–216, 2010.

R. Pohl et al. Laser spectroscopy of muonic deuterium. *Science*, 353:669–673, 2016. doi: 10.1126/science.aaf2468.

Ernest Pollard. Nuclear potential barriers: Experiment and theory. *Physical Review*, 47:611–620, 1935. doi: 10.1103/PhysRev.47.611.

M. Puchalski, A. M. Moro, and K. Pachucki. Isotope Shift of the $3\,^2S_{1/2}$-$2\,^2S_{1/2}$ Transition in Lithium and the Nuclear Polarizability. *Phys. Rev. Lett.*, 97:133001, 2006.

M. Puchalski, K. Pachucki, and J. Komasa. Isotope shift in a beryllium atom. *Physical Review A*, 89:012506, 2014.

S. Raeder et al. Probing Sizes and Shapes of Nobelium Isotopes by Laser Spectroscopy. *Phys. Rev. Lett.*, 120:232503, 2018. doi: 10.1103/PhysRevLett.120.232503.

P. G. Reinhard and D. Drechsel. Ground state correlations and the nuclear charge distribution. *Zeitschrift für Physik A*, 290:85–91, 1979.

P. G. Reinhard and W. Nazarewicz. Toward a global description of nuclear charge radii: Exploring the Fayans energy density functional. *Physical Review C*, 95: 064328, 2017.

M. Reponen et al. Evidence of a sudden increase in the nuclear size of proton-rich silver-96. *Nature Communications*, 12:4596, 2021. doi: 10.1038/s41467-021-24888-x.

L M Robledo, R Rodríguez-Guzmán, and P Sarriguren. Role of triaxiality in the ground-state shape of neutron-rich Yb, Hf, W, Os and Pt isotopes. *Journal of Physics G*, 36:115104, 2009. doi: 10.1088/0954-3899/36/11/115104.

R. Rodríguez-Guzmán, P. Sarriguren, L.M. Robledo, and S. Perez-Martin. Charge radii and structural evolution in Sr, Zr, and Mo isotopes. *Physics Letters B*, 691: 202–207, 2010. doi: https://doi.org/10.1016/j.physletb.2010.06.035.

E. Rutherford. LXXIX. The scattering of α and β particles by matter and the structure of the atom. *The London, Edinburgh, and Dublin Philosophical Magazine and Journal of Science*, 21(125):669–688, 1911. ISSN 1941-5982. doi: 10.1080/14786440508637080.

R. Sánchez et al. Nuclear Charge Radius of ^{11}Li: the Influence of Halo Neutrons. *Physical Review Letters*, 96:033002, 2006.

J. Sauvage, N. Boos, L. Cabaret, J.E. Crawford, H.T. Duong, J. Genevey, M. Girod, G. Huber, F. Ibrahim, M. Krieg, F. Le Blanc, J.K.P. Lee, J. Libert, D. Lunney, J. Obert, J. Oms, S. Péru, J. Pinard, J.C. Putaux, B. Roussière, V. Sebastian, D. Verney, S. Zemlyanoi, J. Arianer, N. Barré, M. Ducourtieux, D. Forkel-Wirth, G. Le Scornet, J. Lettry, and C. Richard-Serre, C. Véron. COMPLIS experiments: Collaboration for spectroscopy measurements using a pulsed laser ion source. *Hyperfine Interactions*, 129(1-4):303–317, 2000. ISSN 0304-3843. doi: 10.1023/A:1012618001695. URL `http://dx.doi.org/10.1023/A%3A1012618001695`.

B. Schinzler et al. Collinear laser spectroscopy of neutron-rich Cs isotopes at an on-line mass separator. *Physics Letters B*, 79:209–212, 1978.

C. Schulz et al. Resonance ionization spectroscopy on a fast atomic ytterbium beam. *Journal of Physics B*, 24:4831, 1991. doi: 10.1088/0953-4075/24/22/020.

C. Schwob et al. Optical Frequency Measurement of the 2S$-$12D Transitions in Hydrogen and Deuterium: Rydberg Constant and Lamb Shift Determinations. *Physical Review Letters*, 82:4960–4963, 1999. doi: 10.1103/PhysRevLett.82.4960.

S. Sels et al. Shape staggering of midshell mercury isotopes from in-source laser spectroscopy compared with density-functional-theory and Monte Carlo shell-model calculations. *Phys. Rev. C*, 99:044306, 2019. doi: 10.1103/PhysRevC.99.044306.

E. C. Seltzer. K X-Ray Isotope Shifts. *Physical Review*, 188:1916–1919, 1969.

N. B. Shulgina, B. Jonson, and M. V. Zhukov. ^{11}Li structure from experimental data. *Nuclear Physics A*, 825:175–199, 2009. doi: 10.1016/j.nuclphysa.2009.04.014.

I. Sick. Model-independent nuclear charge densities from elastic electron scattering. *Nuclear Physics A*, 218:509–541, 1974. doi: 10.1016/0375-9474(74)90039-6.

I. Sick. Precise root-mean-square radius of ^{4}He. *Physical Review C*, 77:041302(R), 2008. doi: 10.1103/Physrevc.77.041302.

R. Silverans, G. Borghs, P. de Bisschop, and M. van Hove. Fast ion beam collinear laser spectroscopy: Some aspects of recent applications, sensitivity and resolution. *Hyperfine Interactions*, 24:181–201, 1985.

R. E. Silverans, P. Lievens, and L. Vermeeren. A Sensitive Measuring Scheme in Collinear Fast-Ion-Beam Laser Spectroscopy - the Optical-Pumping, State-Selective Neutralization and Particle-Detection Sequence. *Nuclear Instruments and Methods in Physics Research B*, 26(4):591–597, 1987.

G. G. Simon et al. Absolute electron-proton cross sections at low momentum transfer measured with a high pressure gas target system. *Nuclear Physics A*, 333(3): 381–391, 1980.

F. Sommer et al. Charge radii of ^{55,56}Ni reveal a surprisingly similar behavior at $N = 28$ in Ca and Ni isotopes. *Phys. Rev. Lett., in print*, 2022.

P. Strasser, T. Matsuzaki, and K. Nagamine. Challenge towards muonic atom formation with unstable nuclei. *European Physical Journal A*, 13:197–202, 2002.

Igal Talmi. On the odd-even effect in the charge radii of isotopes. *Nuclear Physics A*, 423:189–196, 1984.

C. Thibault et al. Hyperfine structure and isotope shift of the D2 line of $^{118-145}$Cs and some of their isomers. *Nuclear Physics A*, 367:1–12, 1981a.

C. Thibault et al. Hyperfine structure and isotope shift of the D_2 line of $^{76-98}$Rb and some of their isomers. *Phys. Rev. C*, 23:2720–2729, 1981b. doi: 10.1103/PhysRevC.23.2720.

Th. Udem et al. Phase-Coherent Measurement of the Hydrogen 1S-2S Transition Frequency with an Optical Frequency Interval Divider Chain. *Physical Review Letters*, 79:2646–2649, 1997. ISSN 0031-9007.

G. Ulm et al. Isotope shift of ^{182}Hg and an update of nuclear moments and charge radii in the isotope range ^{181}Hg-^{206}Hg. *Zeitschrift für Physik A*, 325:247–259, 1986. doi: 10.1007/BF01294605.

P. Van Duppen et al. A laser ion source for on-line mass separation. *Hyperfine Interactions*, 74:193–204, 1992. doi: 10.1007/BF02398629.

A. R. Vernon et al. Simulation of the relative atomic populations of elements $1 \leq z \leq 89$ following charge exchange tested with collinear resonance ionization spectroscopy of indium. *Spectrochimica Acta Part B*, 153:61–83, 2019. doi: 10.1016/j.sab.2019.02.001.

E. Verstraelen et al. Search for octupole-deformed actinium isotopes using resonance ionization spectroscopy. *Phys. Rev. C*, 100:044321, 2019. doi: 10.1103/PhysRevC.100.044321.

A. Voss et al. First Use of High-Frequency Intensity Modulation of Narrow-Linewidth Laser Light and Its Application in Determination of ^{206,205,204}Fr Ground-State Properties. *Phys. Rev. Lett.*, 111:122501, 2013. doi: 10.1103/PhysRevLett.111.122501.

A. Voss et al. Nuclear moments and charge radii of neutron-deficient francium isotopes and isomers. *Phys. Rev. C*, 91:044307, 2015. doi: 10.1103/PhysRevC.91.044307.

L.-B. Wang et al. Laser Spectroscopic Determination of the ^{6}He Nuclear Charge Radius. *Phys. Rev. Lett.*, 93:142501, 2004.

F. Wauters and A. Knecht. The muX project. *SciPost Phys. Proc.*, page 22, 2021. doi: 10.21468/SciPostPhysProc.5.022.

W. H. Wing, G. A. Ruff, W. E. Lamb JR., and J. J. Spezeski. Observation of the Infrared Spectrum of the Hydrogen Molecular Ion HD^{+}. *Physical Review Letters*, 36:1488–1491, 1976.

W. Xiong et al. A small proton charge radius from an electron–proton scattering experiment. *Nature*, 575:147–150, 2019. doi: 10.1038/s41586-019-1721-2.

Z.-C. Yan and G. W. F. Drake. Lithium isotope shifts as a measure of nuclear size. *Physical Review A*, 61:022504, 2000.

D. T. Yordanov et al. Nuclear Charge Radii of $^{21-32}$Mg. *Physical Review Letters*, 108:042504, 2012.

D. T. Yordanov et al. Simple Nuclear Structure in $^{111-129}$Cd from Atomic Isomer Shifts. *Phys. Rev. Lett.*, 116:032501, 2016. doi: 10.1103/PhysRevLett.116.032501.

Larry Zamick. Two body contribution to the effective radius operator. *Annals of Physics*, 66:784–789, 1971. doi: 10.1016/0003-4916(71)90080-7.

P. A. Zyla et al. Review of particle physics. *Prog. Theor. Exp. Phys.*, 2020:083C01, 2020. doi: 10.1093/ptep/ptaa104.